PARTICLE BEHAVIOUR IN HIGH FIELD MAGNETIC FLOCCULATION AND SEPARATION

ROLF VAN KLEEF

PARTICLE BEHAVIOUR IN HIGH FIELD MAGNETIC FLOCCULATION AND SEPARATION

PARTICLE BEHAVIOUR IN HIGH FIELD MAGNETIC FLOCCULATION AND SEPARATION

PROEFSCHRIFT

TER VERKRIJGING VAN DE GRAAD VAN DOCTOR IN DE
WISKUNDE EN NATUURWETENSCHAPPEN
AAN DE KATHOLIEKE UNIVERSITEIT TE NIJMEGEN, OP GEZAG VAN
DE RECTOR MAGNIFICUS PROF DR J H G I GIESBERS,
VOLGENS BESLUIT VAN HET COLLEGE VAN DEKANEN
IN HET OPENBAAR TE VERDEDIGEN
OP VRIJDAG 14 SEPTEMBER 1984
DES NAMIDDAGS TE 2 00 UUR PRECIES

door

RUDOLPHUS PETRUS ANTONIUS ROBERTUS VAN KLEEF
geboren te Nijmegen

1984
Druk Krips Repro Meppel

PROMOTOR:
PROF. DR. P. WYDER

CO-REFERENT:
DR. H.W. MYRON

Iedereen die heeft meegeholpen aan het tot stand komen van dit proefschrift wil ik hiervoor hartelijk danken; in het bijzonder

Martin Parker for enthusiastically introducing me to the world of separation science, for innumerable advices and suggestions and a most enjoyable collaboration,

Kees Kerkdijk voor alle uitstekende adviezen en een plezierige kennismaking met de industriele aspekten van magnetische separatie,

Rick Reijers voor een prettige samenwerking en in het bijzonder zijn bijdrage aan het in het eerste deel van hoofdstuk 3 beschreven experiment,

Klaas van Hulst, Henk Muileman en Jos Rook voor alles tussen (bijna) 0 en (bijna) 15 tesla en veel daaromheen,

en natuurlijk de medewerkers van de afdeling Experimentele Natuurkunde 4 voor alle hulp en de uitstekende werksfeer.

The investigations described in this thesis have been carried out at the Research Institute for Materials of the Faculty of Science at the Catholic University of Nijmegen under the direction of Prof. Dr. P. Wyder.

These investigations in the program of the Netherlands Foundation for Fundamental Research on Matter (F.O.M.) have been supported (in part) by the Netherlands Foundation for Technical Research (S.T.W.).

"Mijne Heren," zei Mellenberg, "de enige die bij de proef aanwezig was, ben ik en toen de graankorrel meel geworden was hield het op met waaien. Het zal u niet eenvoudig vallen om mij snel en afdoend tegenbewijs voor mijn stelling te leveren. Per slot ben ik deskundig, ik ben expert, ik heb er jaren over nagedacht."

J.M.A. Biesheuvel
Uit: De heer Mellenberg.
In de bovenkooi. Meulenhoff Amsterdam.

Contents

CHAPTER 1 AN OVERVIEW OF SOME MAGNETIC SEPARATORS

CHAPTER 2 MAGNETIC FLOCCULATION; ASPECTS OF COLLOID DESTABILIZATION IN HIGH MAGNETIC FIELDS

an overview
of some
magnetic separators

1

1. General Introduction

During the last decade, a considerable amount of research has been carried out on magnetic separation, with respect to the development of still more advanced separators, as well as in search of new applications of this technique. Nowadays, the term magnetic separation is applicable to a large collection of separation techniques, ranging from arrangements to remove scrap metal and machine parts from both industrial and agricultural product streams, to highly sophisticated techniques to separate e.g. blood cells from whole blood (1-4), or tumour cells from bone marrow (5). However, the main application of magnetic separation is found in the mining and clay industry, in which it is used to upgrade ores or to purify kaolin clay.

In principle, magnetic separation is employed to separate particulate materials, in both dry and wet streams, according to their intrinsic magnetic properties. The basic condition, related to magnetic separation is therefore the fact that the particles to be separated should be distinguishable according to these magnetic properties, i.e. the ways in which they respond to an externally applied magnetic field. Table 1.1 shows the periodic table of the elements, in which for each element its response to an applied magnetic field is indicated. The magnetic behaviour of a related compound is also considered in this simple picture (after Kolm et al. (6)).

Only three elements are ferromagnetic (f): iron, cobalt and nickel. Compounds of these elements may be strongly or weakly ferromagnetic or even paramagnetic. Fifty-five elements have paramagnetic properties. Here, we can distinguish between 32 paramagnetic elements that form paramagnetic compounds (pp), 16 paramagnetic elements that form diamagnetic compounds (pd) and 7 elements that become paramagnetic when one or more are present in a compound (pc). However, two of them (nitrogen and copper) are slightly diamagnetic in pure form. Of the remaining elements, about two-thirds are diamagnetic. Separation techniques, capable of processing paramagnetic minerals therefore have the largest range of potential applications. Due to the weaker magnetic properties of these minerals, separators involving higher fields and/or higher field gradients are required.

Magnetic separation brings about a physical separation between discrete particles via a competition between magnetic, gravitational, hydrodynamic and

Table 1.1. Periodic table of the elements.
A magnetic characterization (after Kolm et al. (6)).

H 1																	He 2
Li 3 *pd*	Be 4											B 5	C 6	N 7 *pc*	O 8 *pd*	F 9	Ne 10
Na 11 *pd*	Mg 12 *pd*											Al 13 *pd*	Si 14	P 15	S 16	Cl 17	Ar 18
K 19 *pc*	Ca 20 *pd*	Sc 21 *pp*	Ti 22 *pp*	V 23 *pp*	Cr 24 *pp*	Mn 25 *pp*	Fe 26 *f*	Co 27 *f*	Ni 28 *f*	Cu 29 *pc*	Zn 30	Ga 31 *pd*	Ge 32	As 33	Se 34	Br 35	Kr 36
Rb 37 *pc*	Sr 38 *pd*	Y 39 *pp*	Zr 40 *pd*	Nb 41 *pd*	Mo 42 *pp*	Tc 43 *pp*	Ru 44 *pp*	Rh 45 *pp*	Pd 46 *pp*	Ag 47	Cd 48	In 49	Sn 50 *pd*	Sb 51	Te 52	I 53	Xe 54
Cs 55 *pc*	Ba 56 *pd*	La 57 *pd*	Hf 72 *pd*	Ta 73 *pp*	W 74 *pp*	Re 75 *pp*	Os 76 *pp*	Ir 77 *pp*	Pt 78 *pp*	Au 79 *pc*	Hg 80	Tl 81 *pc*	Pb 82	Bi 83	Po 84	At 85	Rn 86
Fr 87	Ra 88	Ac 89	Kh 104														
Lanthanum series			Ce 58 *pp*	Pr 59 *pp*	Nd 60 *pp*	Pm 61	Sm 62 *pp*	Eu 63 *pp*	Gd 64 *pp*	Tb 65 *pp*	Dy 66 *pp*	Ho 67 *pp*	Er 68 *pp*	Tm 69 *pp*	Yb 70 *pp*	Lu 71 *pd*	
Actinium series			Th 90 *pd*	Pa 91	U 92 *pp*	Np 93	Pu 94 *pp*	Am 95 *pp*	Cm 96	Bk 97	Cf 98	Es 99	Fm 100	Md 101	No 102	Lr 103	

inertial forces. In addition, interparticle forces can influence the effectiveness of the separation. In Figure 1.1, a schematic representation is given of a magnetic separator. Due to magnetic forces, ferromagnetic or paramagnetic particles are separated from the feed. Competing forces are inertial, frictional and gravitational forces, which are also responsible for the transport of the particles through the separator. The magnetic fraction is referred to as the *mags*, the non-magnetic one as the *tails*, while other, less magnetic components are referred to as *middlings*. Attractive interparticle forces and e.g. a too low degree of liberation of one of the components in crushed materials decrease the separation efficiency due to a physical attachement between magnetic and non-magnetic particles.

The efficiency of separation is usually expressed in terms of *recovery* and *grade*. The recovery is defined as the ratio of the concentration of magnetic material in the mags and that in the feed material and the grade is the concentration of magnetic material in the separation products. In principle, these quantities depend on the ratio of magnetic and competing forces.

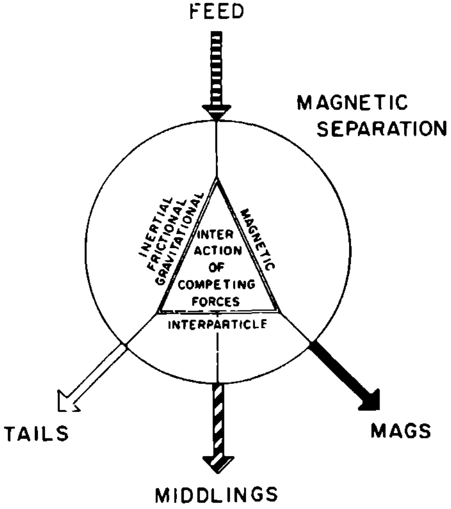

Figure 1.1 Schematic representation of a magnetic separator.

2. Major Types of Magnetic Separators

It is generally accepted, to divide the various types of magnetic separators into two groups, namely Low Gradient Magnetic Separation devices (LGMS) and High Gradient Magnetic Separation devices (HGMS). A further distinction can be made between particle capture techniques and particle deflection techniques, usually referred to as Open Gradient Magnetic Separation (OGMS). These names, however, suggest that the gradients in the magnetic field are of fundamental importance to the separation process and indeed they are, but it is good to emphasize the fact that the magnetic traction force, responsible for the actual separation, is proportional to the product of the magnetic field H and the gradient of the field. In fact the magnetic traction force on a small, non-ferromagnetic particle can be approximated by

$$\vec{F}_M = \tfrac{1}{2}V_p(\chi_p - \chi_m)\vec{\nabla}(HB_o), \qquad (2.1)$$

where V_p is the volume of the particle, $(\chi_p - \chi_m)$ its net magnetic susceptibility with respect to the medium and where the magnetic flux density at the position of the particle is given by $B_o = \mu_o H$. Since volume and susceptibility are the only terms in equation (2.1) that are related to the physical properties of the particle, the magnetic field is characterized by the magnetic force density

$$\vec{f}_M = \tfrac{1}{2}\vec{\nabla}(HB_o). \qquad (2.2)$$

For a given magnetic separator, a typical value of the magnetic force density can be used to characterize that particular device. However, a second important parameter is the range over which the typical force density is present (force range), and therefore some authors prefer to use the energy density (product of magnetic force density and force range) as a parameter for the classification of magnetic separators. In Table 2.1, these typical parameters are given for a number of different separation devices. A short review of the various devices is given in the following. The emphasize will be on the basic principles of the devices and not on the various ways in which they are applied in practice.

Table 2.1 Typical values of the characteristic parameters of magnetic separators (partly after Gerber (7)).

Device	Force Range (m)	Magnetic Force Density (Nm^{-3})	Energy Density (Nm^{-2})
Belt Separator	10^{-2}	$5 \cdot 10^{4}$	$5 \cdot 10^{2}$
Drum Separator	$2 \cdot 10^{-2}$	$2 \cdot 10^{5}$	$4 \cdot 10^{3}$
Frantz Isodynamic Separator	10^{-2}	$8 \cdot 10^{7}$	$8 \cdot 10^{5}$
Induced Roll Separator	$3 \cdot 10^{-3}$	$2 \cdot 10^{9}$	$6 \cdot 10^{6}$
Jones Separator	10^{-3}	$4 \cdot 10^{9}$	$4 \cdot 10^{6}$
Frantz-Ferrofilter	10^{-3}	$7 \cdot 10^{7}$	$7 \cdot 10^{4}$
Conventional HGMS	10^{-4}	$6 \cdot 10^{11}$	$6 \cdot 10^{7}$
Superconducting HGMS	10^{-4}	$2 \cdot 10^{12}$	$2 \cdot 10^{8}$
Ultra High Gradient Magnetic Separator (UHGMS)	10^{-6}	$2 \cdot 10^{15}$	$2 \cdot 10^{9}$

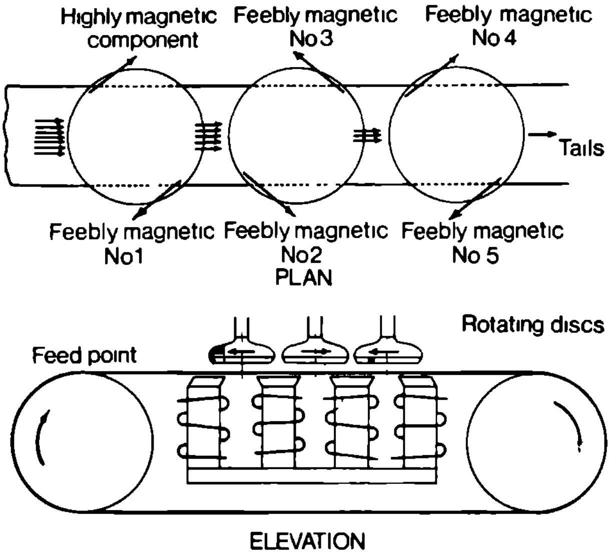

Figure 2.1 Dry belt separator (Boxmag Rapid Ltd.).

Apart from very simple devices, used to remove ferrous tramp metal from a variety of feeds, such as grains, foodstuffs, both in dry and wet form and other low density materials, the *dry belt separator* is one of the best known types of low gradient magnetic separators. The feed is supplied to a moving conveyer belt and passes through a magnet system. Here, magnetic material is removed from the feed on the belt and transported to a place outside the magnet system, where it is collected. Figure 2.1 shows a device of this type, in which the magnetic field is generated by an electromagnetic system, situated underneath the conveyer belt. Above this belt, rotating discs are mounted, which interact with the applied magnetic field. Magnetic particles in the feed are retained by the discs and, due to their rotation, carried away to a place outside the field on both sides of the belt and removed by scrapers.

An important alternative to the belt separator is the *drum separator*. This is probably the most common type of magnetic separator. Dry drum separators may be used to process particles with sizes down to about 100 μm. There exists a variety of devices, including dry drum, wet drum, pulley and induced roll separators. A schematic picture of a drum separator is given in Figure 2.2.

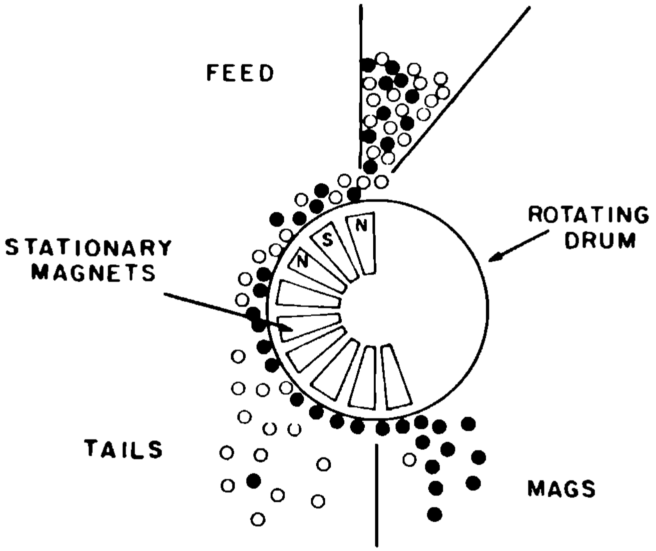

Figure 2.2. Schematic representation of a dry drum separator.

Basically, it consists of a system of magnet poles of alternating polarity, arranged as indicated in the figure. The semi-cylindrical magnet system is surrounded by a rotating drum, made of non-magnetic material. The feed is introduced at the top of the device. The particles move downwards on the surface of the drum, until a position is reached where gravity causes the non-magnetic particles to fall down, while the magnetic particles stay attached to the drum and are carried away to a place outside the magnetic field. With this device, it is possible to produce a middling fraction, which is weaker magnetic than the mags and falls down from the surface of the drum between the tails and the mags. Very often, these middlings consist of particles in which the magnetic component is insufficiently liberated. After collection, this fraction can be ground to a smaller particle size and re-processed by the separator.

The basic principles of operation of an *induced roll separator* are similar to those of a drum separator, although the design of the device is different. In an induced roll separator, the rotating 'drum' is situated between the poles of a magnet system and is magnetized by the field. Magnetic particles are held at the magnetized surface of the roll and are removed at a certain point by brushes. Non-magnetic particles are collected at the point where they fall down from the roll, due to gravity.

A completely different type of separator is the *Frantz-Isodynamic Separator*, schematically represented in Figure 2.3. This device, however, is restricted to operation on laboratory scale. Here, the shape of the pole pieces of an electromagnet is designed to produce an isodynamic field, i.e. a magnetic field for which the product HVH is constant in a certain region between the pole pieces. Therefore, a magnetic traction force is produced on a magnetic particle in the operating zone, independent of its position. In this zone, a narrow chute is placed, which is inclined, both parallel and perpendicular to its length, in order to allow a component of the gravitational force to compete with the magnetic force. The chute is vibrated to reduce friction and the particles move downwards, while experiencing a magnetic force, proportional to their *mass susceptibility*. This force deflects them from their original direction of motion. Finally, the stream is divided by a splitter. Careful operation in a free-fall deflecting mode can result in a separation on the basis of absolute susceptibility of even diamagnetic particles.

High Gradient Magnetic Separators are generally *induced pole* devices, in which a relatively uniform magnetic field induces magnetic poles in a ferro-

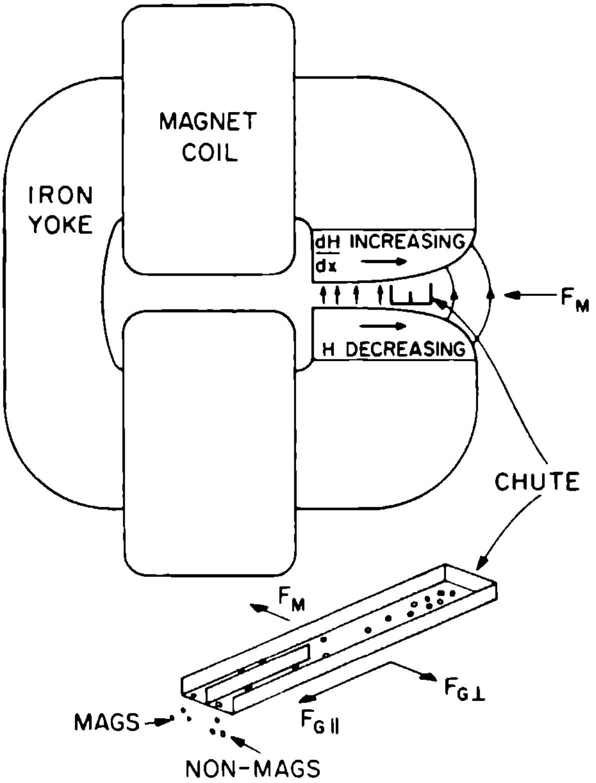

Figure 2.3. Frantz-Isodynamic Separator.

magnetic matrix (screens, grids, grooved plates or fibrous materials). Depending on the physical properties of the matrix, this results in the appearance of large magnetic field gradients, and therefore in large magnetic forces. Unfortunately, large gradients generally exist only in small volumes. Although such a separator is capable of processing very small particles, the capture capacity of the matrix is very limited. In Figure 2.4 and Figure 2.5, representations are given of, respectively, a *Frantz-Ferrofilter* and a *Jones Separator*. In the first device, the matrix consists of grids of ferromagnetic ribbons, which are placed in the bore of a solenoid-type magnet, while the Jones separator utilizes a stack of grooved plates, situated between the poles of an electromagnet.

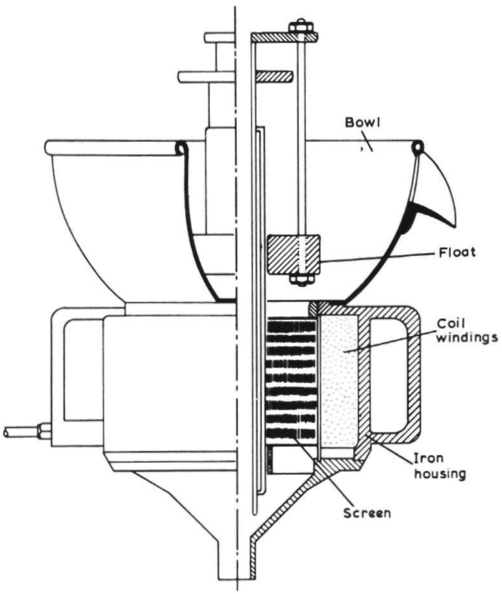

Figure 2.4. The Frantz-ferrofilter.

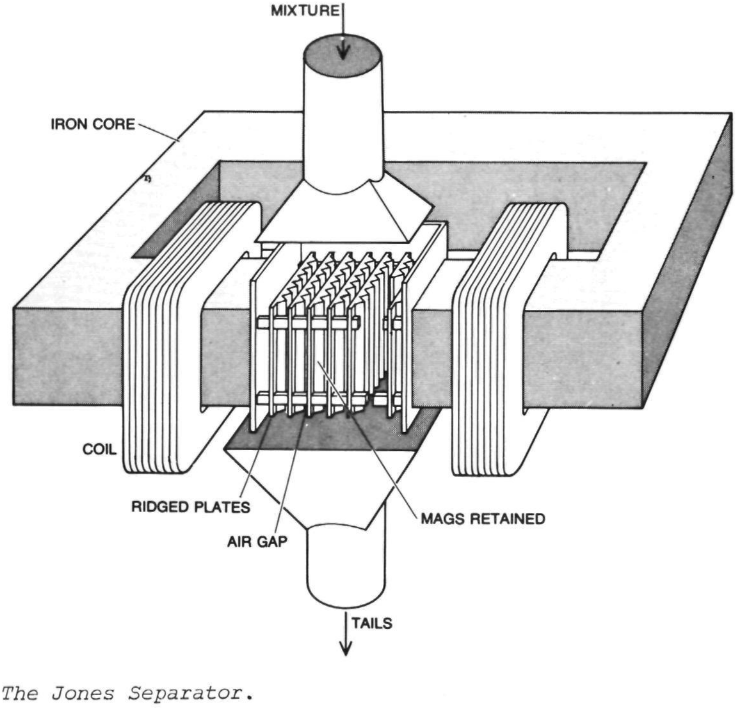

Figure 2.5. The Jones Separator.

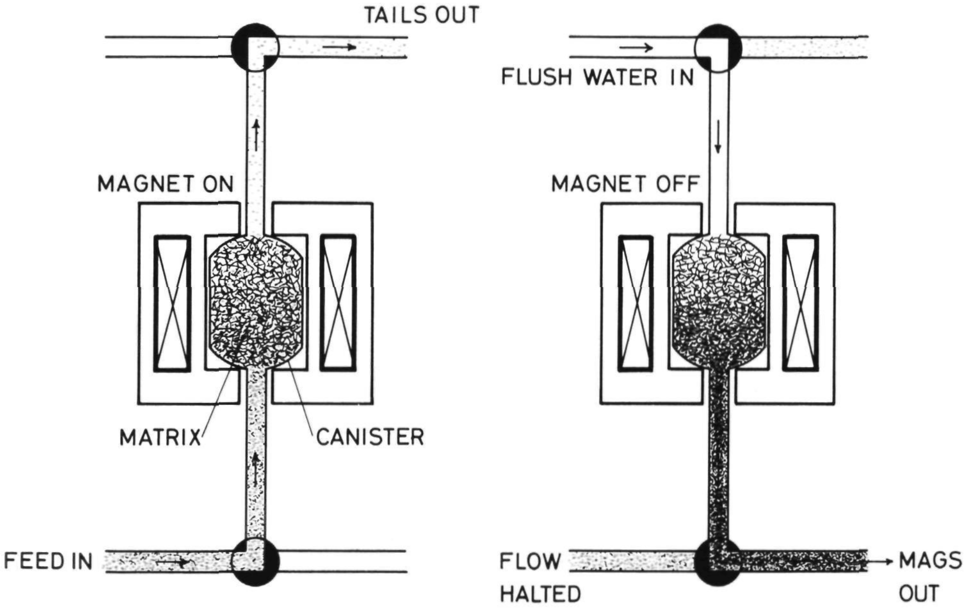

Figure 2.6. Schematic representation of the cyclic process of a High Gradient Magnetic Separator.

High Gradient Magnetic Separators are usually operated in a cyclic mode (see Figure 2.6.). The feed material is pumped through the matrix, with the magnetic field switched on. Magnetic particles are captured on the surface of the matrix, while the non-magnetic ones pass through the matrix. Usually, the feed flow is directed upwards to avoid the capture of non-magnetic material due to gravitational forces. When the matrix becomes saturated with magnetic particles, the feed flow is halted and the matrix is rinsed, at full field, with a small quantity of clean water (not shown in Figure 2.6.), to remove the remaining non-magnetic particles from the matrix and the supply- and outlet-pipes. Then, the field is switched off and the matrix is back-flushed with high-speed flushwater in order to collect the magnetic fraction and regenerate the matrix. After that, a new separation cycle can be started.

Due to this cyclic behaviour, the dead-time of such a separation device is rather long, resulting in a rather low duty cycle. This even gets worse when applying superconducting magnets, because of the long rise- and decay-times of the field. One way of avoiding the cyclic operation is shown in Figure 2.7, where a schematic representation is given of a carousel-type separator. Here, the matrix consists of an annular arrangement of compartments, each filled with filter material (e.g. steel wool), which, by rotation, moves through a specially constructed magnet. Inside the field, the feed slurry is pumped through the matrix compartments, which are subsequently rinsed. Then, at a place outside the magnet, the loaded matrix compartments are cleaned and the magnetic product is collected.

A continuous operation can also be achieved in a reciprocating canister magnetic separator (8). Here, the loaded canister, containing the matrix, is pushed out of the (superconducting) magnet, at full field, by a hydraulic ram and replaced by a fresh one. Because of the immense magnetic forces that act on the canister when it is pushed out of the magnet bore (300 - 500 t for a 2 m length, 1 m diameter canister in a field of 8 T (9)), the canisters are usually part of a linear canister train. This train comprises dummy filters (D)

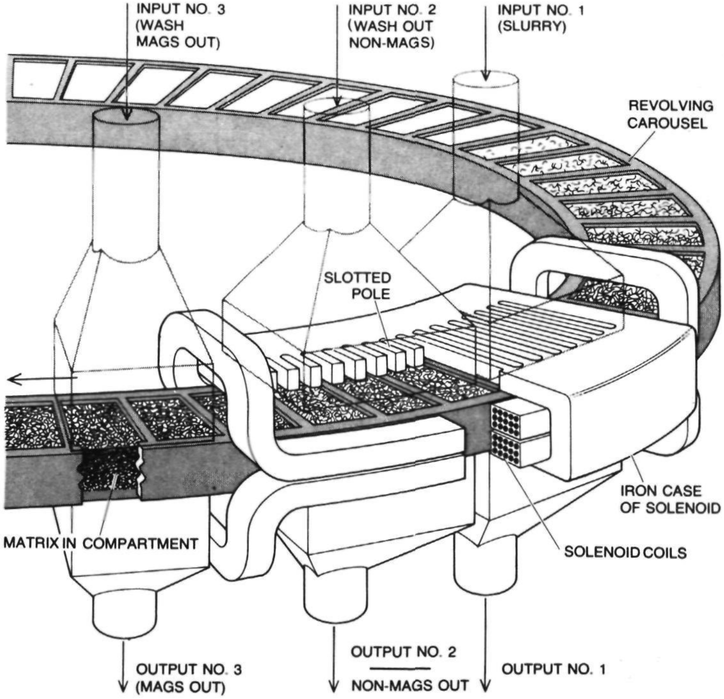

Figure 2.7. Carousel-type high gradient magnetic separator.

and active filters (A) in a symmetric arrangement D-A-D-A-D. Due to this symmetry, the magnetic forces are much smaller and the switching from one canister to the other can be done without damaging the canister or the magnet.

Extensive information on the various types of magnetic separators can be obtained from References (10) to (13). A review of the physics of magnetic separation is given in Reference (10).

3. Additional Remarks

The major part of this thesis deals with the various properties of magnetically induced aggregation of particles. The physics of this process, however, is closely related to high gradient magnetic separation. Where magnetic separation is basically the deposition of a particle on a ferromagnetic matrix element, e.g. a fiber or a sphere, magnetized by an externally applied magnetic field, magnetically induced aggregation can be considered as the deposition of a particle on a second particle. Obviously, the major difference between the two processes is in the balance between the various forces involved, rather than in their specific character.

In chapter 2, a review is given on the basic principles of magnetic flocculation. In addition, the process is illustrated by means of experimental results for relatively coarse particles. In the second part of chapter 3, experimental results concerning flocculation of ultra-fine colloids are described. The first part of chapter 3 deals with the various experimental and theoretical aspects of high gradient magnetic filtration of ultra-fine colloids. The preliminary experiments that were carried out in the scope of this new part of separation science are considered to be the first, promising step towards Ultra High Gradient Magnetic Separation (UHGMS), the separation of ultra-fine particles in ultra-high force fields.

Finally, in chapter 4, an application of magnetic flocculation of relatively coarse particles in non-uniform magnetic fields is described. Here, magnetically enhanced settling is used to separate particles in liquids. This process of selective magnetosedimentation is the basis of what has appeared to be a simple, effective and continuously operating separation technique.

Apart from the work, described in this thesis, various experiments have been carried out to investigate the possibility of application of HGMS or other magnetic separation techniques in industrial processes or in processes of environmental importance. A standard HGMS facility was built, with which laboratory scale separation experiments can be carried out, in applied fields up to 15 T and with any desired fluid velocity. In addition, the continuous flow magnetic separation (CFMS) device is available for the same purpose. A vibrating sample magnetometer (Foner-type) was used to classify the specimens according to their magnetic properties.

Measurements were done for, among others, TNO (14), International Nickel Company, Hoogovens Groep, Billiton Research B.V., ECN, ICI, Unilever and Smit Nymegen.

References

1. M.D. Graham, J. Appl. Phys., 52, (1981), p 2578.
2. M.D. Graham and P.R. Selvin, IEEE Trans. on Magn., MAG-18, (1982), p 1523.
3. M.D. Graham, J. Less-Common Metals, 94, (1983), p 383.
4. F. Paul and D. Melville, to be published in IEEE Trans. on Magn., September 1984.
5. J.G. Trelaeven, F.M. Gibson, J. Ugelstad, A. Rembaum and J.T. Kemshead, Magnetic Separation News, 1, (1984), p 103.
6. H. Kolm, J. Oberteuffer and D. Kelland, Scientific American, 233, (1975), p 47.
7. R. Gerber, IEEE Trans. on Magn., MAG-18, (1982), p 812.
8. P.W. Riley and D. Hocking, IEEE Trans. on Magn., MAG-17, (1981), p 3299.
9. J.H.P. Watson, R.G. Scurlock, A.W. Swales and T. Holden, Proc. 9th Int. Cryogenic Eng. Conf., No. 6, Kobe, Butterworth, (1982), p 120.
10. R.R. Birss and M.R. Parker in *"Progress in Filtration and Separation"*, Vol. 2, R.J. Wakeman (Ed.), Elsevier Amsterdam, (1981).
11. M.R. Parker, Contemp. Phys., 18, (1977), p 279.
12. J.A. Oberteuffer, IEEE Trans. on Magn., MAG-10, (1974), p 233.
13. M.R. Parker, Proc. Symp. Electrical and Magnetic Separation and Filtration Technology, Antwerp, (1984), p 1.
14. W.J.Th. van Gemert, H.M. van der Laan and H.J. Veen, *"Onderzoek Reiniging Baggerslib"*, TNO Hoofdgroep Maatschappelijke Technologie, Report 8722-10765, Ref. 84-02613, April 1984.

magnetic flocculation;
aspects of
colloid destabilization
in high
magnetic fields

2

This chapter is to be published in "Modern Magnetic Separation", M.R. Parker and J.H.P. Watson (Eds.), Gordon & Breach, London, (in preparation).

1. Introduction

In this chapter a review is given of the basic features concerning interparticle interactions of colloidal particles and the related stability of the colloid itself. An additional interaction is introduced, caused by an externally applied magnetic field. It turns out that a magnetic field is able to destabilize a colloid. This process of, what is called, magnetic flocculation is described, starting from various theoretical points of view and is compared with "ordinary" flocculation, i.e. flocculation due to interfacial electrochemical processes. In this chapter, however, only colloid stability in the presence of simple electrolytes is considered, thereby omitting the influence of polymers or other similar flocculants. Some aspects of magnetic flocculation are illustrated by experimental results for suspensions of paramagnetic or diamagnetic particles in high magnetic fields.

In the literature the terminology with respect to particle clustering is somewhat confusing. In order to distinguish between the various types of particle clusters, Gestner (1) proposed the following definitions. Aggregates are firmly constructed groups of primary particles. The physical contact between the particles is at their crystal faces. Agglomerates have a much more porous structure in which the particles are mainly attached to each other at their edges. On the other hand, flocculates are very loosely bound clusters.

Even more confusing is the use of terms like flocculation, aggregation, agglomeration and coagulation. They all imply the formation of clusters of particles. According to Lyklema (2) and Parfitt (3), the term flocculation is used to indicate the reduction in particle number with time as a consequence of irreversible collisions between the particles. They consider the terms flocculation and coagulation to be synonymous. However, Bondi et al. (4) and Corry and Seaman (5) state that the term coagulation is used when the particles are in direct physical contact with each other, e.g. in the case of attachment in a primary energy minimum, due to the influence of simple electrolytes. Flocculation is used when the particles do not completely join together, e.g. in the case of a secondary minimum, adsorption bridging or chemical bridging. However, in this chapter these four terms are used interchangebly, without any further specification.

Likewise, a distinction has to be made between colloids and suspensions of (coarse) particles. Colloids are dispersions of particles with sizes, such that they do not settle under the influence of gravity, but are continuously dispersed by Brownian motion. Suspensions, however, are subject to settling. Usually, the critical diameter between colloids and suspensions is of the order of 1 µm or less. Suspensions with particle sizes in the intermediate region are sometimes called suspensoids.

2. Interparticle Interactions and Colloid Stability

2.1 Electrostatic interaction

When particles are suspended in an aqueous medium, they can develop a surface charge via a number of mechanisms, such as uptake of H^+ or OH^- ions, specific adsorption or dissociation of surface groups. Since electroneutrality is required, a second charge distribution has to be present outside the surface of the particle, which, together with the surface charge, forms the electrical double layer. In fact, most authors (2) divide the double layer into three parts:

1. a surface layer with surface charge σ_o,
2. a Stern layer (6) in which the influence of the specific character of the surface is present; charge σ_m. This Stern layer, in fact, compensates for the finite dimensions of the ions that are adsorbed on the surface,
3. a Gouy layer or diffuse layer: a cloud of counterions, attracted to the surface and with thermal motion as a competing process; charge σ_d.

An illustration of a double layer system, with the related electrical potential ψ is given in Figure 2.1.1. In Stern's model, the ions are treated as point charges, in any respect, except for their inability to approach the solid surface closer than a distance δ because of their actual finite dimensions. The Stern model was refined by Graham (7), who distinguished between the *outer Helmholtz plane (oHp)*, i.e. the closest distance to the solid surface of the centres of the hydrated ions in solution and the *inner Helmholtz plane (iHp)*, when ions are specifically adsorbed on the surface. The charge of these adsorbed ions is denoted as σ_m. Since the space between the surface and the subsequent Helmholtz planes is free of charge, the potential decreases linearly with distance. However, the slope in the two regions may be different.

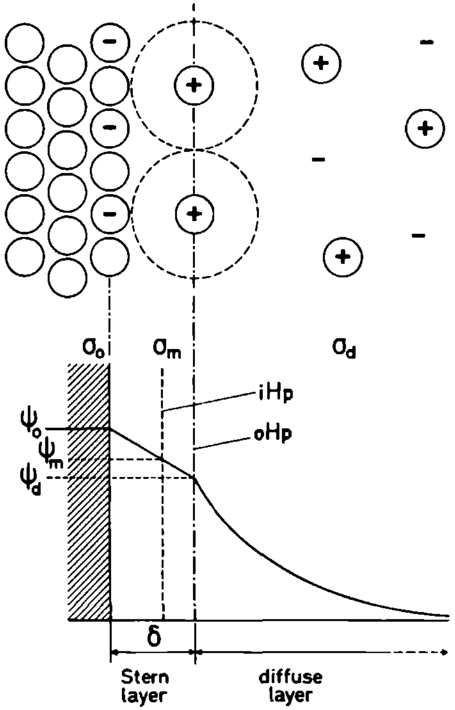

Figure 2.1.1. Illustration of a double layer system, including the Stern layer. Specific adsorption of counterions occurs at the inner Helmholtz plane (iHp).

The ions in the Stern layer are bound to the surface and together with a thin layer of liquid they move along with the particle. One can therefore approximate the potential at the outer side of the Stern layer, ψ_d, by the experimentally detectable ζ-potential, the potential at the plane of shear between particle and liquid.

The theoretical treatment of the double layer system was first developed independently by Gouy (8) and Chapman (9) and later by Debye and Hückel (10). The Coulomb interaction between the charges in such a system is described by Poisson's equation

$$\Delta\psi = -\frac{\rho}{\varepsilon_o\varepsilon_r}, \qquad (2.1.1)$$

where ψ is the electric potential, ρ the charge density and $\varepsilon_o\varepsilon_r$ the dielectric constant of the fluid medium. The distribution of ions in the liquid is given by

$$n_i = n_{io} \exp(-z_i e\psi/kT), \qquad (2.1.2)$$

where n_i is the number density of ions of valence z_i and n_{io} the number density in the bulk liquid (at $\psi = 0$). The charge density ρ is then given by

$$\rho = \Sigma\, z_i e n_i . \qquad (2.1.3)$$

We can now rewrite equation (2.1.1), yielding

$$\Delta\psi = - \frac{1}{\varepsilon_o\varepsilon_r} \sum z_i e n_{io} \exp(-z_i e\psi/kT). \qquad (2.1.4)$$

Using the fact that the system is not allowed to carry any excess charge, equation (2.1.4) can be approximated, for small values of ψ, by

$$\Delta\psi = \kappa^2\psi, \qquad (2.1.5)$$

where

$$\kappa^2 = \frac{e^2\, \Sigma\, n_{io} z_i^2}{\varepsilon_o\varepsilon_r kT} . \qquad (2.1.6)$$

The Debye length $1/\kappa$ is a measure of the thickness of the diffuse layer.

In order to determine the potential energy of interaction for a system of two spherical particles due to interactions between the double layers, we first have to calculate the free energy of a double layer system. Once an expression for the free energy is known (11, 12), the potential energy of interaction immediately follows from the change in free energy when one of the particles is brought from infinity to a certain position with distance r with respect to the other particle. However, some considerations are appropriate at this stage. When thermodynamic equilibrium is assumed, this implies that the surface potential is constant and completely determined by the electrolyte. If two particles approach each other, this means that the double layer charge at the surfaces of the particles decreases and therefore a number of ions has to diffuse into the liquid. Thermodynamic equilibrium will exist during the temporary encounter of two particles only if the diffusion process is sufficiently quick, which is the case for most colloids. However, if this redistribution of charge needs an activation energy through which the system cannot respond quickly enough to a new situation, as is the case for some organic hydrophillic colloids, assumption of constant charge will lead to a better description than the constant potential approach.

In the following we restrict ourselves to the case of constant potential and thus the potential energy is given by

$$V_R = \Delta F = \psi_o (Q_\infty - Q_r), \qquad (2.1.7)$$

where Q_∞ and Q_r are the charges on one particle when it is respectively at infinitely great distance and at a distance r from a second one. Clearly, for a system of equal spherical particles, the double layer potential energy will depend on the surface potential ψ_o, double layer thickness $1/\kappa$, relative permittivity ε_r of the liquid medium and the particle radius a. For particles with a relatively thin double layer (i.e. $\tau = \kappa a >> 1$) the interaction energy can be calculated by using the expressions for the interactions of two infinitely large parallel planes (11, 13). Here, the spherical particles are considered to be built up of infinitisemal parallel rings. For small values of the surface potential, the repulsive energy is thus given by

$$V_R = 2\pi\varepsilon_o\varepsilon_r a\psi_o^2 \ln\{1 + \exp(-\tau(r_a-2))\}, \qquad (2.1.8)$$

$$(\kappa a >> 1)$$

where $r_a = r/a$ is the normalized distance between the centres of the spheres. Expression (2.1.8) should not be used if $\tau < 10$ (11).

When τ (= κa) is small, one can essentially follow the same method as used to calculate the interaction between flat surfaces (11). For small values of ψ_o the repulsive energy is given by

$$V_R = 4\pi\varepsilon_o\varepsilon_r a\psi_o^2 \left\{\frac{\exp\,(-\tau(r_a-2))}{r_a}\right\} \beta, \qquad (2.1.9)$$

$(\kappa a < 1)$

where β is a factor to allow for loss of spherical symmetry as the double layers overlap. Approximate expressions for β, which is a function of the distance between the particles, are given in Ref. (11), p 155 for the two limits $\tau(r_a-2) << 1$ and $\tau(r_a-2) >> 1$.

For a system of two spherical particles with radii a and b, the repulsive energy of interaction can be generalized to (14)

$$V_R = \frac{\pi\varepsilon_o\varepsilon_r ab(\psi_{01}^2+\psi_{02}^2)}{(a+b)} \left[\frac{2\psi_{01}\psi_{02}}{(\psi_{01}^2+\psi_{02}^2)} \ln\left\{\frac{1+\exp(-\kappa H)}{1-\exp(-\kappa H)}\right\} + \ln\{1-\exp(-2\kappa H)\}\right], \qquad (2.1.10)$$

provided the double layer thickness is small compared to the particle sizes. Here, H is the shortest distance between the spheres,

$$H = r - (a + b). \qquad (2.1.11)$$

For chemically identical particles, of course, ψ_{01} will be equal to ψ_{02}.

Since no exact expression exists for the generalization of equation (2.1.9) in the case of dissimilar particles, we suggest an expression of the form

$$V_R = 4\pi\varepsilon_o\varepsilon_r ab\psi_o^2 \frac{\exp(-\kappa H)}{(H+a+b)}. \qquad (2.1.12)$$

This generalization is entirely based on ad hoc arguments, but nevertheless it can be expected to give a reasonable description of the actual interaction. The correction factor β is taken to be unity.

The force between the particles due to the double layer interaction is calculated via the definition

$$F_R = -\frac{\partial V_R}{\partial r} = -\frac{\partial V_R}{\partial H}. \tag{2.1.13}$$

For a system of two equal spherical particles, the repulsive force is given by, respectively,

$$F_R = 2\pi\varepsilon_o\varepsilon_r\psi_o^2\tau \frac{\exp(-\tau(r_a-2))}{\exp(-\tau(r_a-2)) + 1} \tag{2.1.14}$$

if $\tau \gg 1$, and

$$F_R = \frac{4\pi\varepsilon_o\varepsilon_r\psi_o^2}{r_a^2} \left\{(\tau r_a + 1)\beta - r_a \frac{\partial\beta}{\partial r_a}\right\} \exp(-\tau(r_a-2)) \tag{2.1.15}$$

if $\tau < 1$.

The value of β lies between 0.6 and 1, but is usually approximated by unity, even at relatively short interparticle distances (15). In the following we also assume β to be independent of position, thus $\partial\beta/\partial r_a = 0$. For a system of two spherical particles with radii a and b the repulsive force is given by the approximate form

$$F_R = 4\pi\varepsilon_o\varepsilon_r ab\psi_o^2 \frac{(\kappa(H + a + b) + 1)}{(H + a + b)^2} \exp(-\kappa H) \tag{2.1.16}$$

for small values of the double layer thickness, while for large values differentiation of equation (2.1.10) yields

$$F_R = \frac{2\pi\varepsilon_o\varepsilon_r\psi_o^2 ab}{(a + b)} \kappa \frac{\exp(-\kappa H)}{\exp(-\kappa H) + 1}. \tag{2.1.17}$$

2.2 London - van der Waals interaction

London - van der Waals forces are based on the fact that molecules without permanent dipoles can still attract each other due to quantum fluctuations in the distribution of electrons belonging to those molecules. Since one may add the separate contributions of molecule pairs, it is possible to calculate the (long-range) London - van der Waals forces between two macroscopic bodies. For a system of two spherical particles with diameters D_1 and D_2 at a distance d from each other (shortest distance), Hamaker (16) derived the potential energy of the interaction:

$$V_A = -\frac{A}{12}\left\{\frac{y}{x^2+xy+x} + \frac{y}{x^2+xy+x+y} + 2\ln\left(\frac{x^2+xy+x}{x^2+xy+x+y}\right)\right\}, \tag{2.2.1}$$

where $x = d/D_1$, $y = D_2/D_1$ and where A is the Hamaker constant. For two equal spherical particles of radius a, which are separated from each other by a normalized centre-to-centre distance r_a, equation (2.2.1) reduces to

$$V_A = -\frac{A}{6}\left\{\frac{2}{r_a^2-4} + \frac{2}{r_a^2} + \ln\left(\frac{r_a^2-4}{r_a^2}\right)\right\}. \tag{2.2.2}$$

For dissimilar particles of radii a and b, equation (2.2.1) becomes

$$V_A = -\frac{A}{6}\left\{\frac{2}{r_a^2-(\alpha+1)^2} + \frac{2}{r_a^2-(\alpha-1)^2} + \ln\left(\frac{r_a^2-(\alpha+1)^2}{r_a^2-(\alpha-1)^2}\right)\right\}. \tag{2.2.3}$$

Here, the interparticle distance is measured in units of the particle radius a, while α is defined as $\alpha = b/a$. For very small distances, equation (2.2.3) can be approximated by

$$V_A = -\frac{Ab}{6(a+b)(r_a - (\alpha+1))}. \tag{2.2.4}$$

Since the London - van der Waals interaction is of electromagnetic nature, it takes some time for the electromagnetic waves to travel from one particle to the other and back. When the distance between the particles is of the order of the London wavelength or larger, the forces are retarded and their r-dependence is one power faster than for the non-retarded case. This London wavelength is defined as the turning time of the dipoles, times the speed of light and is typically of the order of 1000 Å (17).

In the absence of accurate information on several parameters involved, we will use the non-retarded expressions for the London - van der Waals potential energy, as given above.

The London - van der Waals forces can be derived from the expressions for the potential energy, according to

$$F_A = -\frac{\partial V_A}{\partial r} = -\frac{1}{a}\frac{\partial V_A}{\partial r_a}. \qquad (2.2.5)$$

For two dissimilar particles this results in

$$F_A = \frac{2Ab}{3a^2}\left\{\frac{2\alpha r_a}{r_a^4-2(\alpha^2+1)r_a^2+(\alpha^2-1)^2} - \frac{r_a}{(r_a^2-(\alpha+1)^2)^2} - \frac{r_a}{(r_a^2-(\alpha-1)^2)^2}\right\}, \qquad (2.2.6)$$

which, for identical particles, reduces to

$$F_A = -\frac{32A}{ar_a^3(r_a^2-4)^2}\;. \qquad (2.2.7)$$

The Hamaker constant A, in the preceding equations, for particles of materials 1 and 2, interacting through a fluid medium 3, is given by

$$A = (A_1^{\frac{1}{2}} - A_3^{\frac{1}{2}})(A_2^{\frac{1}{2}} - A_3^{\frac{1}{2}}), \qquad (2.2.8)$$

where A_i is the Hamaker constant of medium i, interacting through vacuum.

Exact data concerning A are hard to obtain (15, 18). Hamaker (16) concludes that $A = 3\cdot 10^{-19}$ J is a very high value, $7\cdot 10^{-20}$ J is a normal value and $7\cdot 10^{-21}$ J is an abnormally low value. Fowkes (19) has shown that for several oxides in water, A varies between $3.5\cdot 10^{-20}$ J and $8\cdot 10^{-20}$ J.

2.3 Magnetic dipole-dipole interaction

When a magnetic field is applied to a colloid, the particles will be polar-

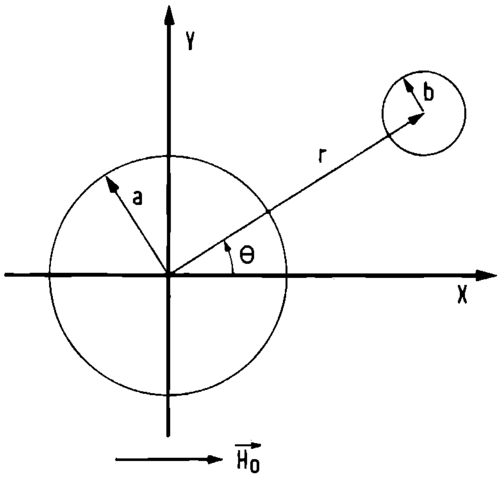

Figure 2.3.1. Coordinate frame of reference for a system of two spherical particles with radii a and b.

ized by the field, resulting in an interaction between the induced dipolar moments. In the following, we will only consider particles which do not possess a permanent magnetic moment, i.e. particles with a field-independent magnetic volume susceptibility χ.

The magnetostatic potential at a point (r,θ) in the coordinate system of Figure 2.3.1, in the vicinity of a spherical particle, radius a, volume susceptibility χ_p, immersed in a fluid of volume susceptibility χ_m and polarized by a magnetic field H_o, can be shown to be (see Appendix I)

$$\phi_m(r,\theta) = -\left(1 - \frac{a^3\chi}{3r^3}\right) H_o r\cos\theta, \qquad (2.3.1)$$

where $\chi = \chi_p - \chi_m$. From this, one can immediately obtain expressions for the radial and azimuthal components of the magnetic field:

$$H_r(r,\theta) = \left(1 + \frac{2\chi a^3}{3r^3}\right) H_o\cos\theta \qquad (2.3.2a)$$

and

$$H_\theta(r,\theta) = -\left(1 - \frac{\chi a^3}{3r^3}\right) H_o \sin\theta. \qquad (2.3.2b)$$

If a second particle, with similar characteristics but with a radius b is placed at a point (r,θ), dipole-dipole interactions between the two particles will produce magnetic forces which can be expressed as (see Appendix I)

$$F_{m,r}(r,\theta) = -\frac{2\pi\chi^2 B_o^2 a^3 b^3}{3\mu_o r^4}(1 + 3\cos 2\theta) \qquad (2.3.3a)$$

and

$$F_{m,\theta}(r,\theta) = -\frac{4\pi\chi^2 B_o^2 a^3 b^3}{3\mu_o r^4}\sin 2\theta. \qquad (2.3.3b)$$

For identical particles these expressions reduce to

$$\vec{F}_m(r,\theta) = -\frac{2\pi\chi^2 B_o^2 a^2}{3\mu_o r_a^4}\left\{(1 + 3\cos 2\theta)\hat{r} + 2\sin 2\theta\,\hat{\theta}\right\}, \qquad (2.3.4)$$

where $\hat{r}$ and $\hat{\theta}$ are unit vectors in the r and θ direction respectively.

2.4 Total interaction energy

Derjaguin and Landau, and independently Verwey and Overbeek stated, in what is now called the DLVO-theory (11), that the total potential energy of interaction between the suspended particles is given by the sum of the repulsive double layer interaction energy and the London - van der Waals energy. This implies that the two interactions are independent. For sufficiently high values of the surface potential, the total energy V_T as a function of interparticle distance passes through a maximum. Physically, this means that there exists a potential energy barrier which prevents the particles from flocculating into the deep primary energy minimum. An example of this situation is

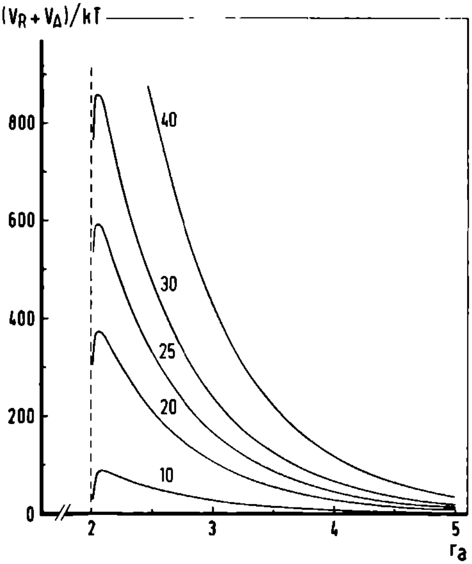

Figure 2.4.1. Potential energy of a two-particle system due to London - van der Waals and double layer interactions, as a function of normalized distance between the particles, for several values of the double layer potential ψ_o (values indicated in mV). (Other parameter values: $a = 10^{-6}$ m, $\kappa = 10^{6}$ m^{-1}, $A = 5 \cdot 10^{-20}$ J)

given in Figure 2.4.1. Extensive studies on the subject of total potential energy were published by Verwey and Overbeek (11, 20).

When an external magnetic field is applied to the colloid, a third type of interaction appears. The DLVO-theory can therefore be extended by including a term, describing the dipole-dipole interaction between the colloidal particles in the presence of an external magnetic induction field B_o (21, 22). For similar particles with a net volume susceptibility χ, the additional term is given by

$$V_M = - \frac{2\pi a^3 \chi^2 B_o^2}{9\mu_o r_a^3} (1 + 3\cos 2\theta), \qquad (2.4.1)$$

where r_a and θ are as defined in Figure 2.3.1. The resultant total potential

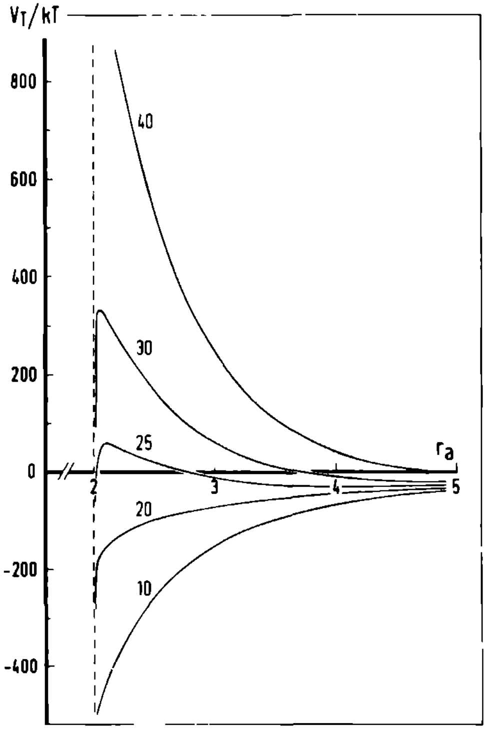

Figure 2.4.2. Total potential energy of interaction for the particle systems of Figure 2.4.1 in an externally applied magnetic field of 0.15 T. (θ = 0)

energy V_T of interaction between two particles, immersed in an electrolyte and in the presence of a magnetic field is now

$$V_T = V_R + V_A + V_M \tag{2.4.2}$$

(see Figure 2.4.2).

Once again we assume that all three terms are independent. Concretely, this means that the influence of high magnetic fields on the thermodynamic equilibrium in the electrical double layer and on the London - van der Waals interaction is not considered important. Also, we will not consider any form of steric stabilization of the colloid.

3. Formation of Agglomerates in High Magnetic Fields

3.1 Introduction

It is clear from equations (2.4.1) and (2.4.2) that a magnetic field is able to decrease the total potential energy barrier until the particles can flocculate into the primary energy minimum. This is illustrated in Figure 3.1.1, where the total potential energy is plotted against interparticle distance for several values of the applied magnetic field. Clearly, the barrier is being reduced, while the position of the maximum shifts towards higher distances when turning up the field. For a certain field value the total potential energy at this maximum is sufficiently low and particles will flocculate. The field at which this takes place is called the threshold field for flocculation B_F (22). Some authors suggest a barrier height of 15 kT as as a threshold situation (23), but there are no obvious reasons for such a choice. In section 3.2, a different method of determining B_F will be described, based on expressions for the particle's velocity in a flocculation process.

In Figure 2.4.2, the total potential energy, in the presence of an external magnetic field, is plotted for the same colloid as in Figure 2.4.1. Clearly, for ψ_o = 25 mV and 30 mV, an energy barrier is present to prevent the particles from touching each other. However, at a somewhat larger distance, the potential energy becomes negative. In this region of space, the magnetic interaction dominates the repulsive double layer interaction, which leads to attractive forces between the particles. As a result, the particles will stay fixed at a certain interparticle distance: they flocculate into a secondary energy minimum.

3.2 Dynamics of magnetically induced particle aggregation

As mentioned above, the magnetic potential energy is uniaxial, with its axis of symmetry along the direction of the magnetic field. This is in contrast with V_R and V_A, which are both spherically symmetric. In order to examine the behaviour of the particles during flocculation, it is convenient to return to the local polar coordinate system of Figure 2.3.1.

In Figure 3.2.1, the aspects of symmetry are illustrated by means of a plot of lines of constant potential energy for a system of two similar haematite (α-Fe$_2$O$_3$) particles in a field of 1 tesla, directed along the $\theta = 0$ direction. This plot has rotational symmetry around the field (x)-axis and mirror symmetry about the yz-plane. Clearly, for positions (r_a, θ) of the second particle, for which $1 + 3\cos 2\theta > 0$ ($\theta < 54^\circ.74$), the total potential energy is negative and the particles experience an attractive force. On the other hand, at positions with $1 + 3\cos 2\theta < 0$, the energy is positive and the particles are pushed away from each other. From this, it can be expected that the poten-

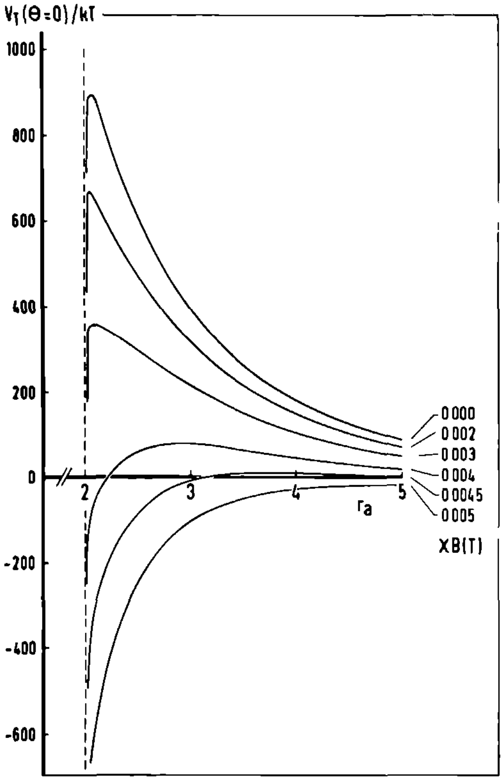

Figure 3.1.1. *Total potential energy of interaction of a two-particle system in the presence of a magnetic field, as a function of the normalized distance. The total potential energy is plotted for various values of the product of magnetic susceptibility and applied magnetic field.*
(Parameter values: $\psi_o = 30$ *mV,* $\kappa = 5 \cdot 10^6$ m^{-1}, $a = 10^{-6}$ *m,* $A = 5 \cdot 10^{-20}$ *J,* $\theta = 0$*)*

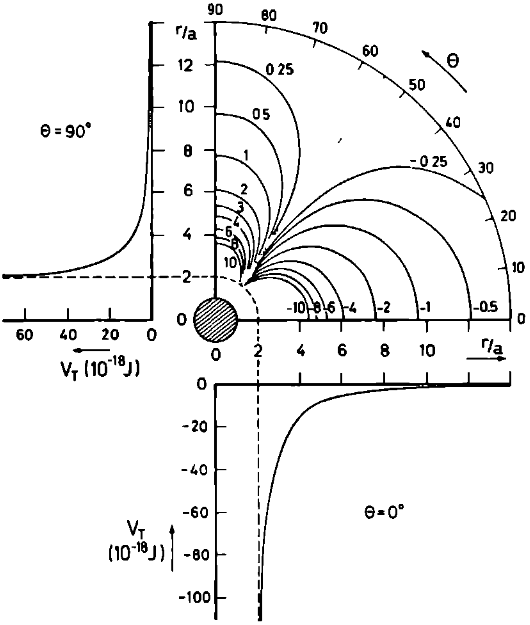

Figure 3.2.1. Lines of constant total potential energy for a system of two similar haematite particles in the coordinate system of Figure 2.3.1. A magnetic field of 1 tesla is applied along the $\theta=0$ direction. The potential energy is expressed in units of 10^{-18} J.

tial energy is of limited use in studying field induced particle aggregation. Therefore, a more general criterion is adapted, based on flocculation into a secondary minimum (24).

A force balance equation is constructed, using the spatial derivative of the potential energies involved, as well as an expression for the Stokes hydrodynamic drag. Since the particle sizes are typically of the order of a few microns or less, the inertialess approximation is used.

The calculations presented in the following are for haematite (α-Fe_2O_3) particles, suspended in water at a pH-value of 7, yielding a value for the Debye-Hückel parameter: $\kappa = 7.67 \cdot 10^5$ m^{-1} (25). For particle sizes of the order of 1 µm, $\kappa a \simeq 1$ and therefore we have to use equation (2.1.12) to express the double layer potential energy. As a result, the radial and azimuthal components of the velocity of the second particle (b) with respect to the first particle (a), localized at the origin, are respectively given by

$$\frac{dr_a}{dt} = \upsilon_{La}\left\{\frac{2\alpha r_a}{r_a^4-2(\alpha^2+1)r_a^2+(\alpha^2-1)^2} - \frac{r_a}{(r_a^2-(\alpha+1)^2)^2} - \frac{r_a}{(r_a^2-(\alpha-1)^2)^2}\right\}$$

$$+ \upsilon_{Ra}\left\{\frac{\tau r_a+1}{r_a^2}\right\} \exp\{-\tau(r_a-(\alpha+1))\}$$

$$+ \upsilon_{Ma}\left\{\frac{1-3\cos^2\theta}{r_a^4}\right\} \qquad (3.2.1a)$$

and

$$r_a \frac{d\theta}{dt} = - \upsilon_{Ma} \frac{\sin 2\theta}{r_a^4} \; . \qquad (3.2.1b)$$

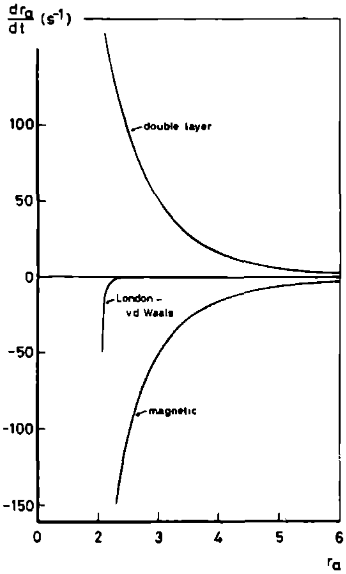

Figure 3.2.2. Contribution of each of the indicated interactions to the on-axis radial velocity of a single particle, relative to a second one at the origin.

Here,

$$\upsilon_{Ma} = \upsilon_M/a = \frac{2\chi^2 b^3 B_o^2}{9\mu_o \eta a^3}\ , \qquad (3.2.2a)$$

$$\upsilon_{La} = \upsilon_L/a = \frac{A}{9\pi\eta a^3} \qquad (3.2.2b)$$

and

$$\upsilon_{Ra} = \upsilon_R/a = \frac{2\varepsilon_o \varepsilon_r \psi_o^2}{3\eta a^2} \qquad (3.2.2c)$$

are normalized , characteristic velocity coefficients, which may be termed the magnetic, the London - van der Waals and the double layer velocities respectively, in analogy with High Gradient Magnetic Separation (26). These equations can be made to describe a system of two similar particles by substituting b=a and α=1 (27).

In Figure 3.2.2 the contribution to the radial velocity at θ=0 is shown for each of the three terms in equation (3.2.1a) for 1 µm-radius α-Fe_2O_3 particles in water of pH=7 at an applied magnetic field of 0.17 tesla. Clearly, the London - van der Waals interaction can be neglected for all values of r_a, except those very close to r_a=2.

Equations (3.2.1a) and (3.2.1b) have been solved for the corresponding set of parameters using a fourth order Runge-Kutta technique (see Appendix II). For other parameter constants, the conclusions drawn here are unaltered, although details may differ. A result is shown in Figure 3.2.3, where the trajectories of the second particle are plotted for various values of the magnetic field. The localized frame of reference is the same as in Figure 2.3.1 for the case a=b.

A non-ferromagnetic particle, initially positioned at a point (r,θ) in the first quadrant of the xy-plane of Figure 3.2.3, precesses in a clockwise fashion, solely due to the magnetically induced (negative) azimuthal velocity component (c.f. equation (3.2.1b)). When the particle approaches the x-axis, its azimuthal velocity component will approach zero, proportional to sin2θ.

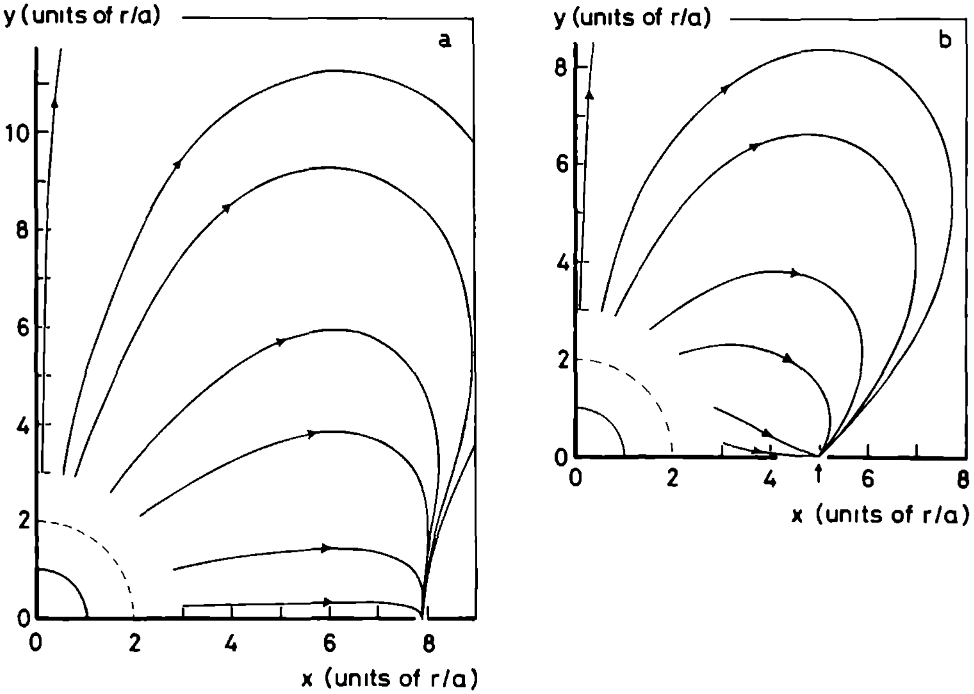

Figure 3.2.3. Trajectories of a single particle, relative to a second one, fixed at the origin, in an applied magnetic field directed along the x-axis.
(a) $B=0.10$ T; (b) $B=0.16$ T.
Parameter values: $a=10^{-6}$ m; $\chi=2\cdot10^{-2}$, $\psi_o=2.5\cdot10^{-2}$ V; $\kappa=7.67\cdot10^{5}$ m^{-1}; $A=5\cdot10^{-20}$ J.

The particle is not able to cross the x-axis since the azimuthal component changes sign when θ becomes negative. At a field of 0.1 tesla (Figure 3.2.3a), the magnetic interaction is not strong enough to be able to compete with the electrostatic repulsion at relatively close distances. Particles, released in the vicinity of the particle at the origin, are forced to move to larger distances. Eventually, particles released almost anywhere in the first quadrant of Figure 3.2.3a will arrive at a stable position ($r_a=7.9$, $\theta=0$). This is an example of flocculation into a secondary minimum. When a particle is released near the y-axis ($\theta=90^{\circ}$), it will be strongly repelled and therefore it will move towards large distances. Although the interaction is weak at those distances, the particle will eventually reach the stable position at the x-axis,

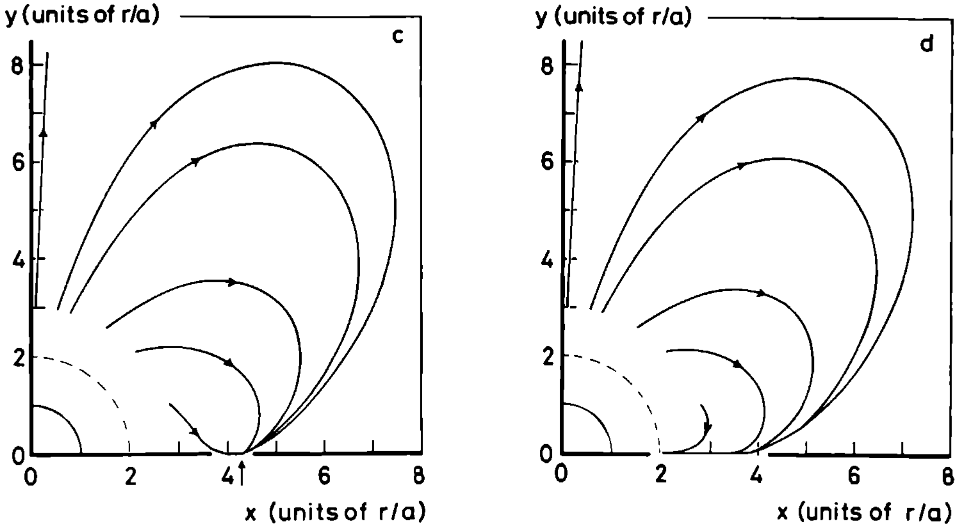

Figure 3.2.3. (continued) Trajectories of a single particle, relative to a second one fixed at the origin.
(c) B=0.17 T; (d) B=0.18 T.

but the traveling time involved is too large to be of practical importance.

In Figure 3.2.3b and c, particle trajectories are plotted for higher values of the magnetic field. Clearly, the magnetic interaction is becoming more effective and the position of the secondary minimum is shifting towards smaller interparticle distances. Eventually, at a field of 0.18 tesla, (Figure 3.2.3d), the secondary minimum collapses and the particles directly flocculate into the deep primary minimum.

In Figure 3.2.4 the radial component of the particle velocity (at $\theta=0$) is plotted for several values of the applied magnetic field. The set of parameter constants was the same as used in Figure 3.2.3. In the absence of a magnetic field, the radial velocity is positive at all interparticle distances (except for $r_a \simeq 2$) because the particles experience a repulsive force. For field values up to 0.17 tesla there exists a region with respectively positive and negative radial velocities. In this field interval, flocculation into a secondary minimum occurs. Then, at fields above 0.17 tesla, the radial velocity is negative at any position (r_a, $\theta=0$).

The positions of the secondary minimum in Figure 3.2.3 correspond with the points in Figure 3.2.4 where the radial velocity changes from negative to positive on approaching the origin. One can therefore define the threshold field for flocculation, B_F, as the field at which the secondary minimum collapses and the particles directly flocculate into the primary energy minimum.

In Figure 3.2.5 the position and field value of the secondary minimum is shown for pairs of identical α-Fe_2O_3 particles in the size range of 0.8 to 2.0 μm. The threshold field B_F is reached for these curves where the secondary minimum collapses, i.e. at the transition to the shaded region. One can notice that the position of the secondary minimum increases with decreasing field and decreases (in units of r/a) with increasing particle size at fixed field values. The collapse positions of the secondary minimum and the corresponding thresh-

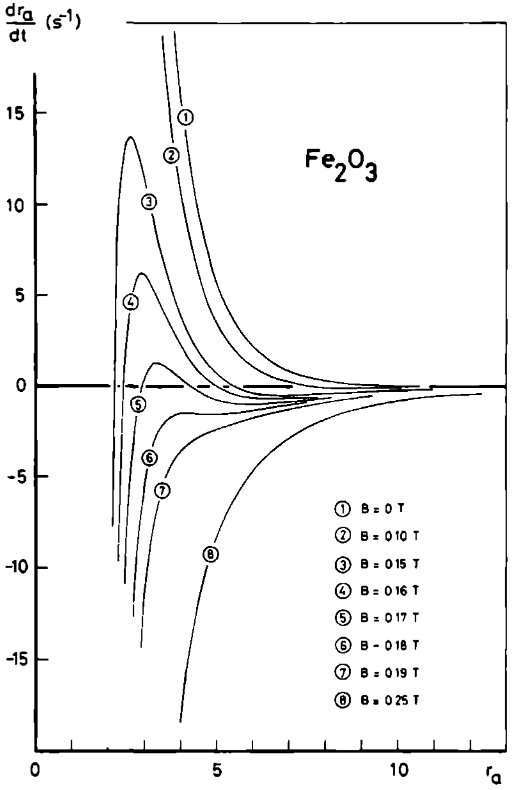

Figure 3.2.4. Normalized on-axis radial velocity as a function of interparticle distance for several values of the applied magnetic field.

old fields, as a function of particle size, are displayed in the inset of Figure 3.2.5.

Figure 3.2.6 shows the same quantities for a system of two interacting α-Fe$_2$O$_3$ particles of dissimilar sizes. Here, r_{sm} and B_F are plotted as a function of the geometrical mean $\sqrt{ab}$ of the particle pair. For a smaller geometrical mean, both collapse position and threshold field increase.

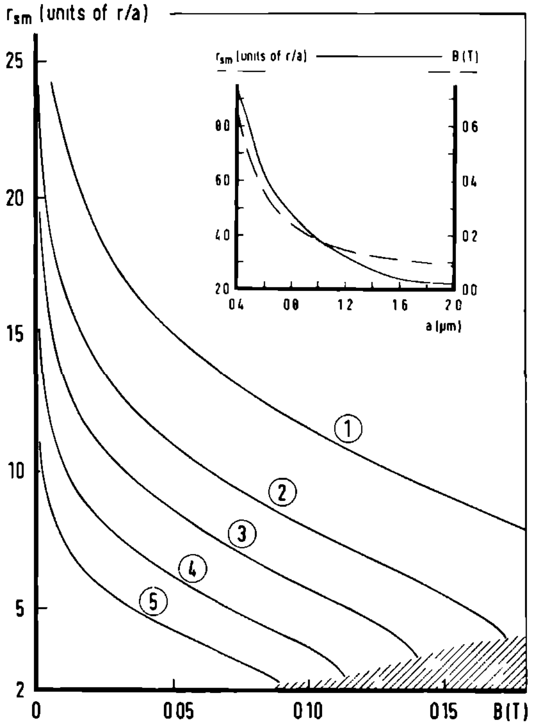

Figure 3.2.5. Position of the secondary minimum vs. magnetic field for identical haematite particles with radii: (1) 0.8 μm, (2) 1.0 μm; (3) 1.2 μm, (4) 1.5 μm; (5) 2.0 μm. In the inset, the collapse positions and fields of the secondary minimum are shown as a function of particle radius.

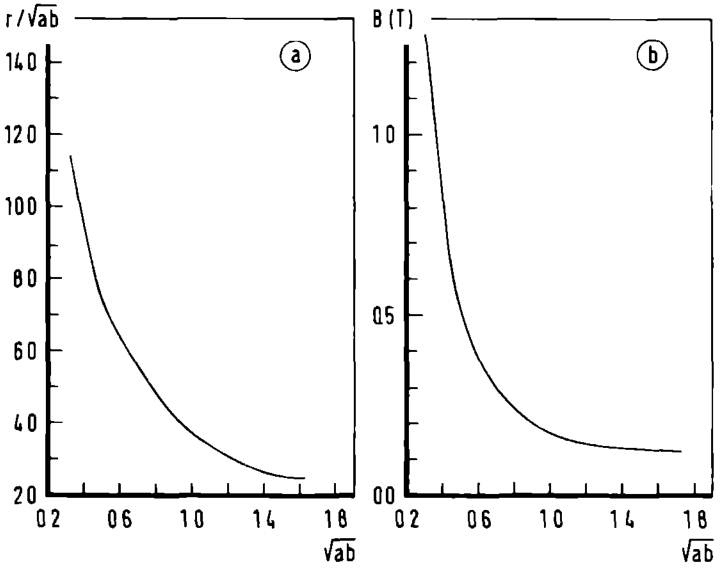

Figure 3.2.6. Collapse position (a) and field (b) of the secondary minimum for dissimilar haematite particles with radii a and b as a function of the geometrical mean of the particle pair.

4. Particle Size Limits on Magnetic Flocculation

4.1 Lower size limit: thermal diffusion

The agglomeration of small particles on a nucleation centre is described by the continuity equation

$$\frac{\partial n}{\partial t} + \vec{\nabla}\cdot\vec{j} = 0 \ , \qquad (4.1.1)$$

where the first term measures the rate of reduction of the particle number density and where $\vec{\nabla}\cdot\vec{j}$ is the total particle flux.

Consider a force field, created by a non-ferromagnetic particle of radius a, in a uniform external magnetic induction field B_0. Consider this particle to be fixed and surrounded by a "cloud" of similar particles, also of radius a. Assume that there is no interparticle interaction in this cloud. Then, the motion of these particles can, to a first approximation, be expressed in terms of a flux of particles moving towards the fixed one, because of the force field, and a flux of particles moving outwards because of a gradient in the particle density. The motion of the particles is opposed by hydrodynamic drag and therefore their velocity, due to the magnetic interaction, can be expressed as

$$\vec{u}(r,\theta) = \vec{\nabla}V_M(r,\theta) \ / \ 6\pi\eta a \ , \tag{4.1.2}$$

where V_M is the magnetic potential energy of interaction and η is the viscosity of the fluid medium. The flux of particles due to the force field is thus $n(r,\theta)\vec{u}(r,\theta)$. The opposing thermal diffusion flux is given by

$$D\vec{\nabla}n(r,\theta) \ , \tag{4.1.3}$$

where the diffusion coefficient D is given by

$$D = kT/6\pi\eta a \ . \tag{4.1.4}$$

Thus, at equilibrium conditions, $\partial n/\partial t = 0$, the continuity equation reads

$$D\vec{\nabla}n(r,\theta) = -n(r,\theta)\vec{u}(r,\theta) \ . \tag{4.1.5}$$

For a magnetic potential energy of the form as expressed in equation (2.4.1), equation (4.1.5) can be written in terms of radial and azimuthal components, yielding

$$\frac{1}{n'(r,\theta)} \frac{\partial n'(r,\theta)}{\partial r_a} = - \frac{W}{kT} \frac{(1 + 3\cos 2\theta)}{r_a^4} \tag{4.1.6a}$$

and

$$\frac{1}{n'(r,\theta)} \frac{\partial n'(r,\theta)}{\partial \theta} = - \frac{2W}{kT} \frac{\sin 2\theta}{r_a^3} \tag{4.1.6b}$$

respectively, where

$$W = \frac{2\pi\chi^2 B_o^2 a^3}{3\mu_o} \tag{4.1.7}$$

and n' is the particle number density, normalized with respect to its value at r_a=2 and θ=0.

In the symmetry directions θ=0 and θ=π/2, equation (4.1.6) may be solved analytically. For θ=0, for example, the particle number density drops exponentially according to

$$n'(r,\theta) = n_o \exp\{- \frac{W}{6kT} (1 - \frac{8}{r_a^3})\} , \tag{4.1.8}$$

where n_o is the number density of particles of radius a, surrounding the flocculation centre in a close packed limit.

A thermal limit can be set to magnetically induced particle agglomeration when the magnetic energy term in equation (4.1.6) becomes comparable to kT, i.e. when W≃kT. This corresponds to a lower limit on particle size of approximately

$$b_{min} = (3\mu_o kT/2\pi\chi^2 B_o^2)^{1/3} . \tag{4.1.9}$$

For haematite particles, suspended in water at room temperature, this leads to

$$b_{min} \simeq 2 \cdot 10^{-8}\ B_o^{-2/3} . \tag{4.1.10}$$

The one-third power law is consistent with a similar expression for the case of particle capture at a domain wall in a Bitter pattern formation (28).

4.2 Upper size limit: the influence of sedimentation

For particle sizes well above the lower limit, derived in the last section, $W \gg kT$ and the flocculation process has to be considered in terms of individual particles rather than particle fluxes. Although, in principle, there is no upper size limit upon the formation of particle clusters, some hydrodynamic aspects become increasingly important. For larger particle sizes, the gravitational settling velocity v_s becomes crucially important in causing resistance to the formation of aggregates of more than two particles (29, 30).

According to the previously discussed dynamic model, at fields above B_F, doublets are formed which, in the case of a vertical field, settle parallel to their axis of symmetry. The settling velocity v_s' of these clusters depends on the gain in mass and Stokes radius, relative to a single particle. Stöber et al. (31) proposed for the Stokes radius a_n of a cluster of n identical spherical particles

$$a_n = n^{1/4} a , \tag{4.2.1}$$

where a is the Stokes radius of a single particle. This implies that, on the basis of a simple force balance equation, the gravitational settling rate of the cluster will be given by

$$v_s' = n^{3/4} v_s , \tag{4.2.2}$$

which for a doublet leads to $v_s' = 1.68\ v_s$. The considerations on which the derivation of equation (4.2.1) is based are, however, questionable. Since the doublet is only allowed to settle parallel to its long axis of symmetry, we will assume, to a first approximation, that the Stokes diameter of the cluster and of the single particle do not differ substantially, yielding $v_s' \simeq 2v_s$.

In order to enable the formation of aggregates with more than two particles, the difference in settling velocity between the doublet and the single particle has to be compensated by a sufficiently large magnetic velocity of the singlet, otherwise it cannot, generally speaking, line up with the doublet.

The normalized characteristic velocities υ_{La}, υ_{Ra} and υ_{Ma} in equation (3.2.2) can, for a pair of identical particles, be seen to be proportional to a^{-3}, a^{-2} and a^{0} respectively. In addition, the normalized gravitational settling velocity

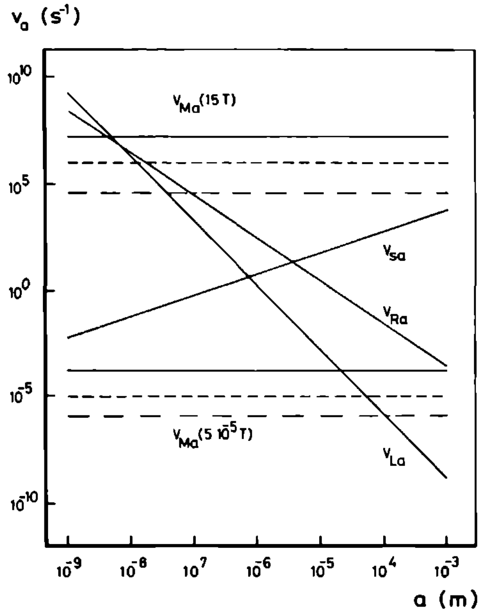

Figure 4.2.1. Size dependence of the various characteristic velocity components for particles of haematite (-), siderite (---) and goethite (-.-.-).

$$v_{sa} = 2(\rho_p-\rho_l)ag/9\eta \tag{4.2.3}$$

is proportional to a^1. In Figure 4.2.1 the size dependence of these velocities is graphically shown for three types of minerals. Clearly, v_{sa} becomes significant in the size range above 1 μm.

A different approach can be considered by calculating the trajectories of a single particle in the vicinity of a doublet. This can be done by means of the previously described dynamical model. For this purpose, consider the doublet to be placed at the origin of the frame of reference of Figure 4.2.2. The single particle is situated at an arbitrary point in the r,θ plane. The interaction between the singlet and the doublet is now calculated, assuming that the individual particles in the doublet do not interfere with each other, i.e. the field distribution around the doublet is approximated by a superposition of the field distribution around a particle at the origin and a particle at (-2a,0). The same approximations are made concerning the double layer and London - van der Waals interactions. The interaction distance r' and angle θ' of the second element of the doublet can be expressed in the coordinates of the singlet position via, respectively

$$r' = (4a^2 + r^2 + 4ar\cos\theta)^{\frac{1}{2}} \tag{4.2.4a}$$

and

$$\sin\theta' = \frac{r\sin\theta}{r+2a} . \tag{4.2.4b}$$

In the frame of reference of Figure 4.2.2 and for a vertical magnetic field, the particle situated at (r,θ) obtains a certain drift velocity v_d, equal to the difference in settling velocity between the doublet and the singlet. The influence of the potential flow of fluid around the doublet can be taken into account (32), resulting in radial and azimuthal drift velocity components of the form

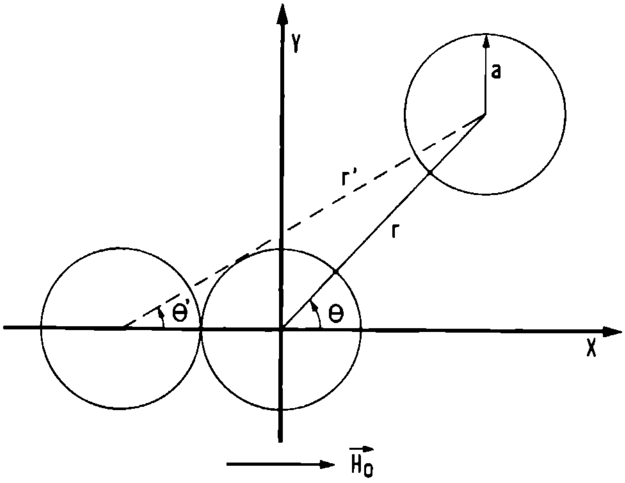

Figure 4.2.2. Coordinate system in the case of interaction between a single particle and a doublet.

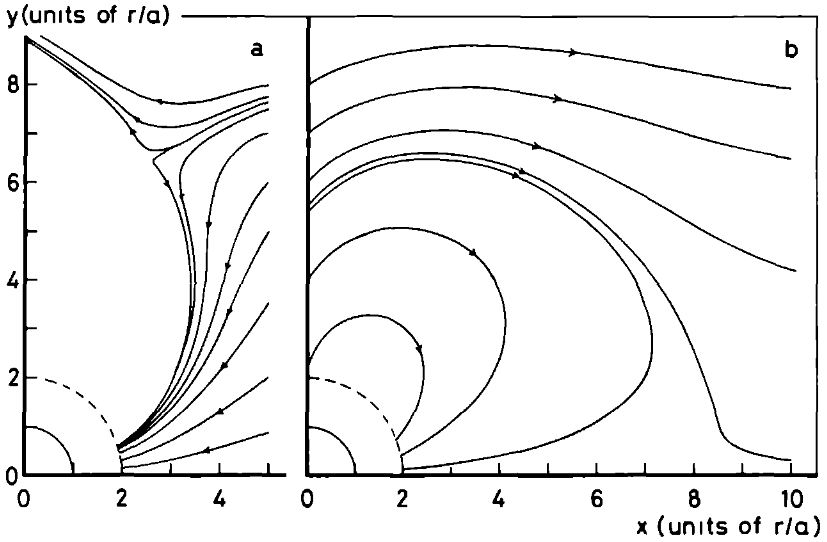

Figure 4.2.3. Trajectories of a single particle relative to a doublet at the origin. The single particle is initially lower (a) and higher (b) in the suspension than the cluster. The magnetic field is directed parallel to the x-axis.

$$v_{da,r} = \pm v_{da} \left(A - \frac{B}{r_a^3}\right) \cos\theta \tag{4.2.5a}$$

and

$$v_{da,\theta} = \mp v_{da} \left(A + \frac{B}{2r_a^3}\right) \sin\theta \, , \tag{4.2.5b}$$

respectively. The sign depends on whether the singlet was initially higher or lower in the suspension than the doublet. A and B are constants, derived via the method of images for equal particle radii and are 0.1958 and 2.39032 respectively.

In Figure 4.2.3, trajectories of a single α-Fe_2O_3 particle, relative to the doublet at the origin, are plotted for the singlet initially being lower (Fig. 4.2.3a) and higher (Figure 4.2.3b) in the suspension than the doublet. The above-mentioned set of system parameters was used, at a field of 1 tesla, while the normalized drift velocity was chosen to be $|v_{da}| = 1$.

From the example of Figure 4.2.3 and other, similar calculations, one can conclude (30, 33) that the capture radius of a doublet is much smaller than of a singlet (about 1 to 3, for the situation of Figure 4.2.3) and decreases rapidly with increasing drift velocity. In addition, the capture radius depends on whether the singlet was initially at a higher or lower point than the doublet. Clearly, the capture radius is larger for the latter.

That size in itself does not restrict the occurrence of higher-than-binary clusters was shown for spherical monosize latex particles in a solution of manganous chloride (30). Here, the formation of two-, three- and four-particle chains was observed when the drift velocity was eliminated by matching the specific density of latex and fluid.

4.3 Particle size and heterocoagulation

Until now we have not considered the influence of sedimentation on the state of flocculation in polydisperse suspensions of coarse particles. In suspensions of this type, gravity has a substantial influence, because particles with different sizes will settle with different rates and therefore may collide.

In the following, we will estimate the magnetogravitational force between the elements of a binary cluster of spherical particles with different radii and compare the results with interparticle forces due to electrical double layer interaction, London - van der Waals and magnetic interactions. For the derivation of the magnetogravitational force between the elements of the cluster, we will extend the calculations of Van Mil et al. (34), to include the effect of magnetosedimentation and a magnetic dipole-dipole interparticle interaction.

Consider two particles with diameters d_1 and d_2, settling with their centres along the same vertical axis, in a vertical magnetic field. Each of the particles will settle under the combined influence of gravity and a magnetic force due to a gradient in the field, according to

$$F_{mg,i} = \frac{\pi}{6} d_{v,i}^3 (\rho_p - \rho_l) g + \frac{\pi}{6} d_{v,i}^3 (\chi_p - \chi_l) \frac{B \nabla B}{\mu_o} , \qquad (4.3.1)$$

where $i = 1,2$ and $d_{v,i}$ is the volume diameter of particle number i, i.e. the diameter of a sphere, having the same volume as the particle. By defining a magnetic density

$$\rho_m = \frac{(\chi_p - \chi_l) B \nabla B}{\mu_o g} , \tag{4.3.2}$$

equation (4.3.1) can be rewritten in the form

$$F_{mg,i} = \frac{\pi}{6} d_{v,i}^3 (\rho_g + \rho_m) g , \tag{4.3.3}$$

where ρ_g is the net density of the particles with respect to the fluid. The total magnetogravitational force F_{MG} between the particles is then given by

$$F_{MG} = F_{mg,1} - F_{mg,2} + F_{f,1} - F_{f,2} . \tag{4.3.4}$$

$F_{f,i}$ is the Stokes force

$$F_{f,i} = -3\pi\eta d_{d,i} v , \tag{4.3.5}$$

where $d_{d,i}$ is the drag diameter of particle i, i.e. the diameter of a sphere having the same friction factor as the particle. In equation (4.3.4), particle 1 is assumed to be situated *above* particle 2. Clearly, for particle 1 being the larger one, F_{MG} is positive, indicating an attractive force. For the reverse situation, F_{MG} is a repulsive force.

When the particle cluster settles with a velocity v_a (subscript a: aggregate), one can approximate the friction (drag) force on the individual elements by

$$F_{f,i} = -3\pi\eta d_{d,i} v_a . \tag{4.3.6}$$

In addition, the total drag force on the cluster is described by

$$F_{mg,1} + F_{mg,2} = -F_{f,a} = 3\pi\eta d_{d,a} v_a . \tag{4.3.7}$$

By approximating the drag diameter d_d by the surface diameter d_s, i.e. the diameter of a sphere having the same surface area as the particle, the total magnetogravitational force can be written as

$$F_{MG} = \frac{\pi}{6} (\rho_g+\rho_m) \{d^3_{v,1} - d^3_{v,2}$$

$$- (d_{v,1} - d_{v,2})(d^3_{v,1} + d^3_{v,2})^{2/3} \frac{\sqrt{\Psi_a}}{\sqrt{\Psi}}\} , \qquad (4.3.8)$$

where the shape factor Ψ, defined as

$$\Psi \equiv d_v^2 \; / \; d_s^2 , \qquad (4.3.9)$$

can easily be calculated for spherical particles.

Of course, the result in equation (4.3.8) is to be considered only as a rough estimate of the actual magnetogravitational force, since the Stokes forces on the individual elements of the cluster were assumed to be independent of each other.

When the lower particle (number 2) is larger than particle number 1, F_{MG} is a separating force. In order to examine the state of flocculation, F_{MG} has to be compared with the other interparticle forces. For $|F_{MG}| < |F_A+F_R+F_M|$, the cluster is stable and the two elements will settle as a whole. On the other hand, when $|F_{MG}| > |F_A+F_R+F_M|$, the repulsive force exceeds the attractive forces and the cluster will break up.

The maximum size of particle 2 in a stable cluster can be obtained by equating the magnetogravitational force F_{MG} and the other, interparticle forces. In Figure 4.3.1., the maximum diameter of the *lower* particle (number 2), relative to the *upper* particle (number 1), is plotted against the diameter of particle 1, for several values of the applied magnetic field. The two spherical particles are assumed to settle in a magnetic field of uniform field gradient (i.e. $\nabla B = \xi B$), such that the resulting magnetic force assists gravity. The smallest distance H, between the two agglomerated particles was assumed to be 5 nm. For small values of d_1, d_2 may vary widely (see Figure 4.3.1). Thus, the difference in particle size of particle 1 and 2 may be large. However, this difference decreases with increasing size d_1 of the upper particle. We can therefore conclude that heterocoagulation will occur more frequently in polydisperse suspensions of micron-size particles than for larger average particle sizes. However, although the maximum value of d_2/d_1 decreases with increasing value of d_1, the absolute maximum size of particle 2 increases,

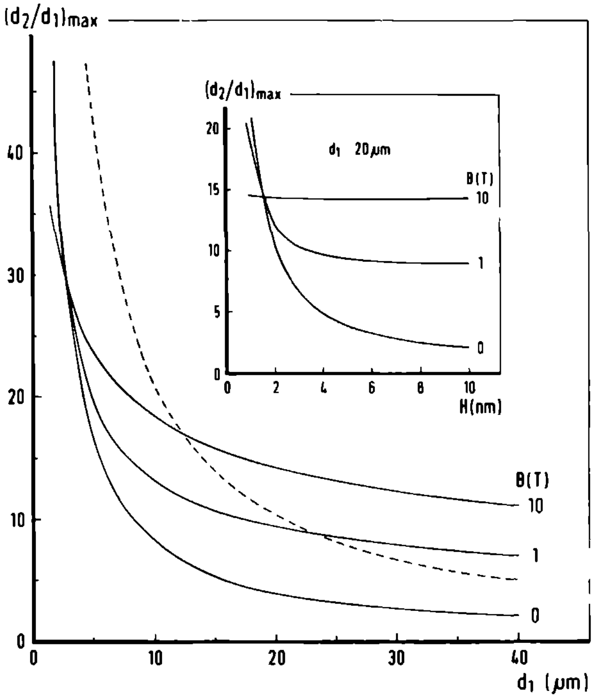

Figure 4.3.1. Maximum diameter of the lower particle relative to the size of the upper particle in a binary cluster, settling in a non-uniform magnetic field B. The smallest distance between the particles is 5 nm, except for the dashed curve, which represents the case of a smallest distance of 2 nm in the absence of a field. The inset shows the maximum diameter as a function of the smallest distance H for d_1=20 µm.

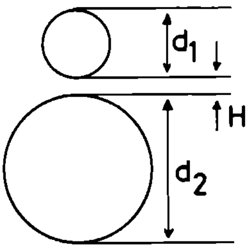

except in the absence of a magnetic field, where $d_{2,max}$ is nearly independent of d_1. In the inset of Figure 4.3.1, the dependence of $(d_2/d_1)_{max}$ on the interparticle distance H is shown for a 20 µm-diameter upper particle. The curves, belonging to different values of the applied magnetic field, intersect at about H = 1.5 nm. Additional calculations have shown that this intersection 'point' shifts towards higher values of H for smaller values of d_1.

5. Kinetics of Magnetic Flocculation

5.1 Rapid coagulation

A colloidal dispersion may be considered stable if the total number of "particles" remains constant. The main mechanism through which this total number can vary is flocculation, in which the particles come into close contact, under the influence of their Brownian motion, and form clusters. The collision rate is therefore determined by diffusion processes.

Von Smoluchowski (35), in his theory on rapid coagulation, assumed that there was no interaction present between the spherical, monodisperse particles and that Brownian motion was the only driving force through which collisions could occur. In addition, he assumed that every collision led to a permanent contact between the particles. Then the initial rate of coagulation is given by

$$-\frac{dn_o}{dt} = Kn_o^2 , \qquad (5.1.1)$$

where n_o is the initial number density of single particles and K is the rate constant, associated with the disappearance of singlets. K is related to the diffusion coefficient and the particle radius a via

$$K = 16\pi Da . \qquad (5.1.2)$$

The influence of interparticle interaction on the rate of coagulation can be included (36) by a factor W, according to

$$-\frac{dn_o}{dt} = \frac{K}{W} n_o^2 , \qquad (5.1.3)$$

where W is given by

$$W = 2a \int_{2a}^{\infty} \exp\left(\frac{V_T}{kT}\right) \frac{dr}{r^2} . \qquad (5.1.4)$$

Here, V_T is the total potential energy of interaction. The factor W is called the stability ratio and measures the ratio of rapid to slow coagulation. In principle, W can be modified to account for dissimilar particle sizes (20, 37) and for the decrease in diffusion coefficient at small interparticle distances (38, 39).

A characteristic relaxation time τ of a flocculation process can be defined as the time, required for the original number of singlets to decrease by a factor of two. In the case of rapid coagulation, this relaxation time is given by

$$\tau = \frac{1}{8\pi D a n_o} \qquad (5.1.5)$$

5.2 Flocculation frequency for magnetic flocculation

Theories on coagulation of colloidal particles, as proposed by Von Smoluchowski, together with the more recent modifications, are based on the spherical symmetry of the interparticle interactions. Therefore, these theories cannot, directly, be extended to include for a magnetically induced interaction, because of its lack of spherical symmetry. However, the problem can be solved in a semi-analytical way by means of the dynamical model, introduced in section 3.2 (40).

Consider a monodisperse colloid of, say, α-Fe_2O_3 particles. For moderate values of the magnetic interaction, a typical flocculation orbit in a two-particle system (c.f. Figure 2.3.1) is illustrated by the dashed curve in Figure 5.2.1. Because of the assumption that inertia can be neglected, the particle, released at any point on the trajectory, will trace an orbit which coincides with the remaining part of the original trajectory. Therefore, each point of the orbit in Figure 5.2.1 is related to a variable which indicates the time needed for the particle to flocculate with the particle at the origin, when it is released at that particular point. Since there exists a whole continuum of flocculation trajectories like the one shown in Figure 5.2.1, there will also exist an infinite collection of starting points of capture trajectories with equal orbit times. Such a collection will describe a curve in the xy-plane of Figure 5.2.1 and may be called an *isochronal* curve. Several isochronal curves, for different capture times, are shown in Figure 5.2.1 for a

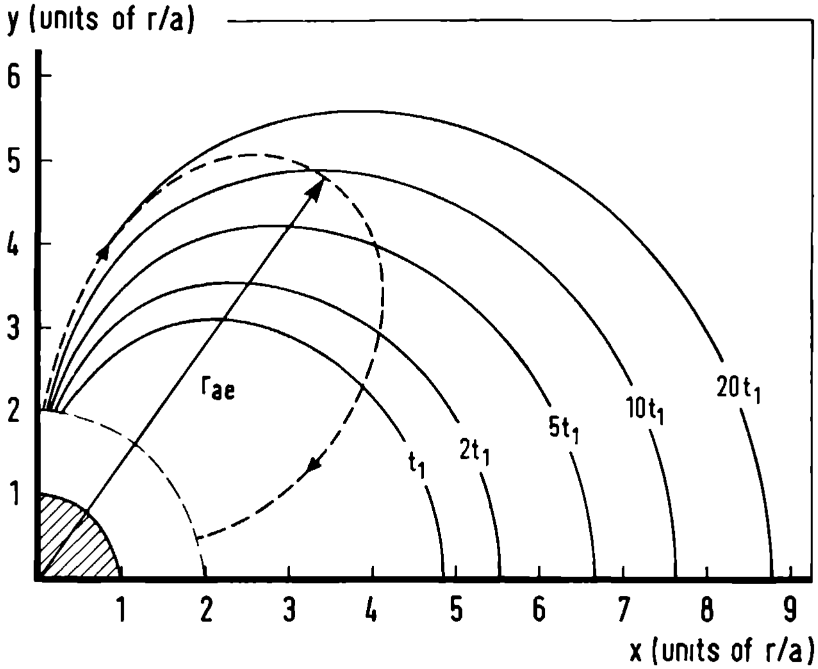

Figure 5.2.1. *Isochronal curves with various capture times for 1 micron-radius haematite particles in a field of 1.0 tesla, directed along the x-axis.*
t_1 = *3.7 ms.*

set of system parameters as used in the preceding sections.

The isochronal curve has the same symmetry as the magnetic dipole-dipole interaction between the two particles, i.e. rotational symmetry around the x-axis and mirror symmetry about the yz-plane. Thus, by applying these symmetry conditions, each isochronal curve generates an *isochronal surface* $S_I(t_c)$: the total collection of particle release points with a capture time t_c.

In order to study the kinetic properties of magnetically induced flocculation, it is convenient to represent a colloid of number density n_o as being built up of $n_o/2$ particle pairs per unit volume, thus reducing the system to a two-particle problem. Every particle pair occupies an *equivalent volume* Ω_o, such that

$$\Omega_o = 2/n_o \ . \tag{5.2.1}$$

In addition, we assume that there is no interaction between neighbouring equivalent volumes. With one of the particles situated at the centre of an equivalent volume Ω_o, the complete colloid can be represented by a two-particle system if the second particle is represented by a homogeneously distributed particle cloud of number density $n_o/2$, i.e. each point within Ω_o can, with equal probability, be the initial position of the second particle. However, only those particles with an initial position inside the isochronal surface $S_I(t_c)$ are able to flocculate with the central particle within a time t_c. Because of the random distribution, the fraction of particles that flocculate within t_c is given by the ratio of the total volume enclosed by $S_I(t_c)$ and the equivalent volume, i.e. $V_I(t_c)/\Omega_o$. Then the number of particle pairs, formed per unit volume and per unit time (flocculation frequency), is given by

$$\nu_m = \frac{V_I(t_c)}{4t_c}\, n_o^2 \equiv Q(t_c)\, n_o^2 \ . \tag{5.2.2}$$

Here, $V_I(t_c)$ is the total volume enclosed by $S_I(t_c)$ and $Q(t_c)$ is a cumulative time rate of expansion of this *isochronal volume* for a given set of system parameters.

Assuming that $Q(t_c)$ does not explicitely depend on time, one can easily derive an expression for the relaxation time of magnetic flocculation, c.f. equation (5.1.5), yielding

$$\tau_m = (2Q(t_c)n_o)^{-1} \ . \tag{5.2.3}$$

Clearly, the flocculation frequency and half-life show the same dependence on particle number density as in the case of rapid coagulation.

The isochronal volume V_I is a function of both capture time t_c and magnetic field B. This is illustrated in Figure 5.2.2, where the normalized isochronal volume is plotted against capture time for several values of the applied magnietic field. Since no analytical expressions for the isochronal surface were available, the calculation of the isochronal volume was based on Monte Carlo integration techniques. In Figure 5.2.2, each of the four curves eventually

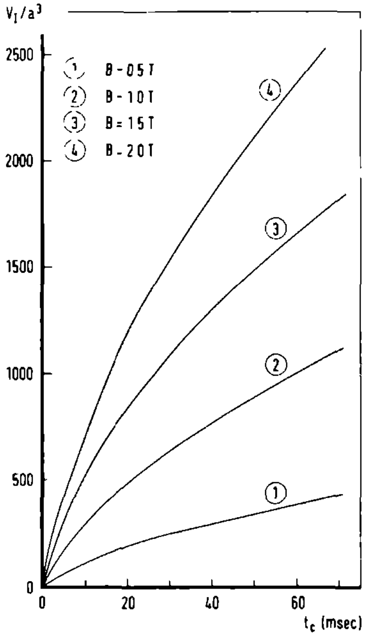

Figure 5.2.2. Dependence of the normalized isochronal volume on capture time for various values of the applied magnetic field.

becomes linearly dependent upon t_c at higher values of the capture time. This indicates the validity of equation (5.2.3). The field dependence of $Q(t_c)$ is shown in Figure 5.2.3 for several values of the capture time and is essentially a linear one.

In the following it is convenient to consider the equivalent volume Ω_o of a pair of particles to be of spherical shape, with one of the particles at its centre. Clearly, a limiting situation occurs when the isochronal volume touches the surface of the sphere, but is still completely surrounded by it, i.e. when the equivalent volume intersects with the x-axis at $x = (3\Omega_o/4\pi)^{1/3}$. Since only those particles, situated inside the isochronal volume are able to flocculate with the central particle, this situation will not result in 100% flocculation. In fact, for the isochronal volumes at $t_c = 5t_1$, $10t_1$ and $20t_1$ (see Figure 5.2.1), $V_I/\Omega_{o,limit}$, and thus the fraction of particles that are able to flocculate, is approximately 0.4.

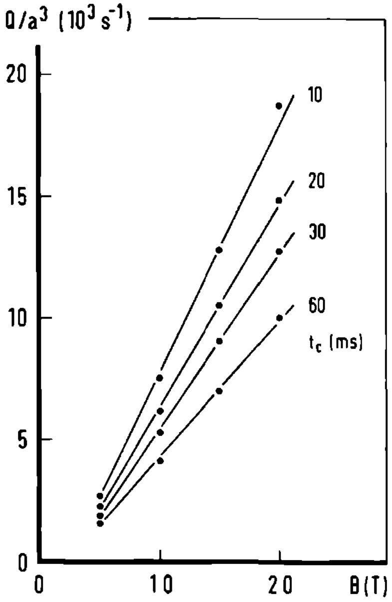

Figure 5.2.3. Dependence of $Q(t_c)$ (eq. 5.2.2) on the applied magnetic field for several capture times.

Increase in particle number density and/or increase in capture time will lead to a situation where the isochronal volume is truncated by the equivalent volume, in the first case because of a smaller equivalent volume and in the second case because of a larger isochronal volume. However, this truncated volume will, for real situations, always be smaller than Ω_o. Therefore, total magnetic flocculation is not to be expected. The capture time reduces to a value equal to the orbit time around the maximum excursion distance r_{ae} (c.f. Figure 5.2.1).

5.3 Non-static colloids

Although the above considerations relate to a static colloid, Brownian motion of submicron particles can be included. On the other hand, the effects of relative motion of the particles acquires a different approach. Relative motion of the particles can be brought about in various ways, such as mechanical stirring, settling of polydisperse colloids or by applying non-uniform magnetic fields. The simplest possible approach is to consider a colloid in which a fraction of the (monosized) particles moves with a drift velocity v_d, parallel to the magnetic field. If the colloid contains αn_o stationary and $(1-\alpha)n_o$ moving particles per unit volume ($0 < \alpha < 1$), then it can be shown that the flocculation frequency is given by

$$\nu_m = \pi\alpha(1-\alpha)r_{ca}^2(v_d)v_d n_o^2 \ . \tag{5.3.1}$$

Here, $r_{ca}(v_d)$ is the normalized capture radius of a stationary particle for the case that an identical particle moves with drift velocity v_d, parallel to the field axis. Although this capture radius diminishes with increasing drift velocity, the product $r_{ca}^2 v_d$ increases steadily, showing an approximately linear dependence for $v_d/a > 2$, for 1 micron-radius haematite particles. Therefore, at a certain value of v_d, the flocculation frequency will exceed that of the static colloid. An upper limit is reached when v_d becomes that large that hydrodynamic forces will destabilize the doublets.

6. Experimental Results

6.1 Magnetic flocculation of coarse paramagnetic particles

Coarse particles (> 1 μm), suspended in water, will settle under the influence of gravity, since the effect of Brownian motion is too small to prevent this. After some time, the suspension will be completely settled down, thus being changed into a sediment with a layer of clear liquid on top of it. The volume of this sediment is a measure of the stability of the suspension or, better, of the degree of flocculation. In a stable (unflocculated) suspension, the particles in the sediment are able to find positions of minimal potential energy and thus the sediment will be a very close-packed arrangement of particles. On the other hand, a flocculated system sediments more rapidly due to aggregate formation and the sediment will be quite porous since the particles remain in the position in which they first touched each other. In this case the volume of the sediment will be larger. Although this method of determining stability conditions by measuring the sediment volume can be of great help in preparing a stable suspension, it is quite useless in studying the process of magnetic flocculation.

As pointed out before, instability of a suspension is clearly detectable via its settling velocity, since this quantity is directly related to the size of the settling particles or aggregates. Studies on magnetic field induced flocculation have been carried out, using a number of mineral suspensions, by determining the settling rate as a function of the applied vertical magnetic field (41, 42). The field was generated by a 15 tesla Bitter magnet. The suspensions were held in calibrated test tubes, which were placed inside the bore of the magnet, just above the point of maximum field, in a region of low field gradient. The settling velocities were measured at a fixed point, by determining the rate of fall of the interface between the sedimenting particles and the liquid, using the optical arrangement of the type shown in Figure 6.1.1. The samples comprised mineral suspensions of Fe_2O_3, $MnCO_3$, Mn_2O_3, $Mn_2P_2O_7$, MnO, Cr_2O_3 and CuO in water. The characteristics are given in Table 6.1.1.

Repeated measurements on these samples have clearly shown the influence on

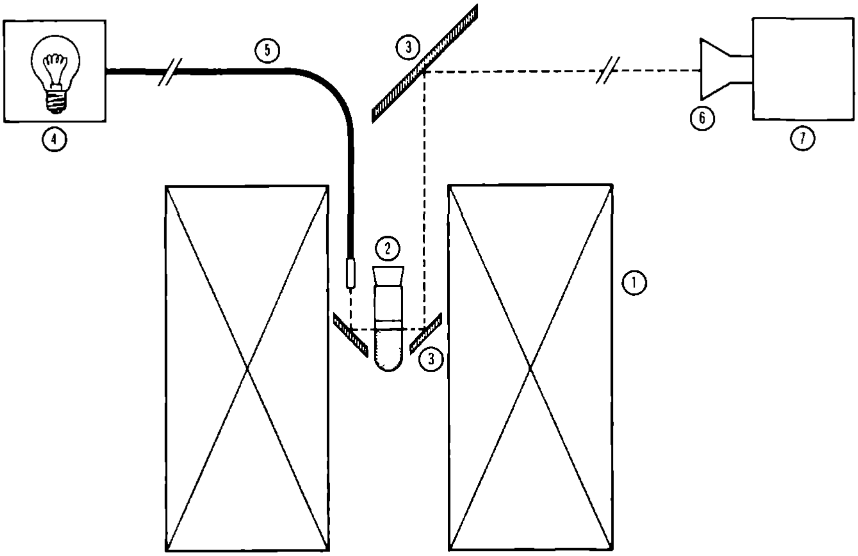

Figure 6.1.1. Optical arrangement for measuring settling velocities. (1) Bitter magnet; (2) sample in test tube; (3) beam deflectors; (4) light source; (5) light guide; (6) telelens; (7) video camera.

the settling rate of the gradient in the applied magnetic field. The magnetic forces on the particles are proportional to the field and to the gradient of the field, which, for the present situation, is expressible at any point on the axis of the magnet by a geometrical function, say ξ, times the field. Therefore, paramagnetic particles of volume V settle under the combined influence of gravitational and magnetic dipolar forces according to, within first approximation, a force-balance equation of the form

$$V(\rho_p-\rho_l)g + V(\chi_p-\chi_l)\xi \frac{B_o^2}{\mu_o} = 6\pi\eta a_S v_S , \qquad (6.1.1)$$

where $(\rho_p-\rho_l)$ and $(\chi_p-\chi_l)$ respectively are the net density and susceptibility of the particles, with respect to the fluid, v_s is the settling velocity and a_S is the Stokes radius of the particle. Typical settling rates for fine mineral suspensions as a function of the magnetic field are shown in Figure 6.1.2. At relatively low fields, the settling rate increases with the square of the magnetic field, under the influence of a magnetic force according to equation (6.1.1). Then, at some critical value of the field, a discontinuity appears, while at higher fields again a quadratic field dependence can be observed. This discontinuity clearly indicates the pair formation of particles, since,

Table 6.1.1 Characteristics of suspensions.

Material	Volume susceptibility (SI-units)	Zero field settling velocity (10^{-5} m/s)	Flocculation threshold field (T)	Stokes radius (10^{-6} m)
Fe_2O_3	$2 \cdot 10^{-2}$	0.5	-	0.9
Mn_2O_3	$5.3 \cdot 10^{-3}$	5.5	2.2	2.5
$Mn_2P_2O_7$	$4.7 \cdot 10^{-3}$	0.5	5.5	3.0
MnO	$4.6 \cdot 10^{-3}$	1.0	4.3	1.0
$MnCO_3$	$4.3 \cdot 10^{-3}$	0.8	3.9[1]	1.3
Cr_2O_3	$1.6 \cdot 10^{-3}$	3.8	>15	2.0
CuO	$2.4 \cdot 10^{-4}$	1.5	>15	1.1

[1] Suspended in a 0.25 M solution of $MnCl_2 \cdot 4H_2O$.

when this occurs, the volume term on the l.h.s. of equation (6.1.1) is doubled, while the Stokes radius of the singlet in the r.h.s. is replaced by that of the doublet. In fact, according to equation (6.1.1), the slope of the linear curves in Figure 6.1.2 on either sides of the discontinuity should differ by a factor equal to $V_d a_{Ss}/V_s a_{Sd}$, where the subscripts s and d refer to singlet and doublet respectively. For the experimental results in Figure 6.1.2, this factor varies from 1.8 ($MnCO_3$) via 1.9 ($Mn_2P_2O_7$) and 2.1 (Mn_2O_3) to about 3 for MnO, thus confirming the assumption that doublets are formed with about twice the volume of a singlet, while the Stokes radius stays about the same. For suspensions of CuO and Cr_2O_3, no evidence of magnetically induced flocculation was found for fields up to 15 tesla.

On the basis of the experimental results we can draw the following conclusions. First, no signs of the formation of aggregates, higher than doublets, were observed in the experimentally available field interval. Second, the doublets appear to be stable, even at enhanced settling velocities in high magnetic fields. Third, a suitable field gradient in combination with magnetically induced flocculation and high fields is able to enhance the settling rate by at least a factor of 12, for fields up to $\sqrt{2}$ times the flocculation threshold field. Finally, the experimental results show that this threshold field is inversely proportional to the magnetic susceptibility, although particle size and double layer potential have a strong influence.

For suspensions of Cr_2O_3 and to a less extend for Mn_2O_3, the settling velocity (see Figure 6.1.2) passes through a minimum at low fields, before the influence of the dipolar force becomes observable. This is believed to be caused by an anisotropic nature of the particles themselves. It is well-established (43, 44) that non-spherical particles do not settle in orientations that are hydrodynamically most favourable. For a settling suspension of, say, disc-shaped particles, it is therefore fair to assume that values for the angle θ between the normal to the disc and the direction of settling will turn out to be homogeneously distributed between -π/2 and π/2. For small particles, the anisotropy in magnetic susceptibility is often between directions in the plane of the disc and normal to it. Such a particle with principle susceptibilities $\chi_{/\!/}$ and $\chi_\perp$ and volume V will experience a torque τ, due to the magnetic field, given by

$$\tau = \tfrac{1}{2}(\chi_\perp - \chi_{/\!/})H^2 V \sin 2\theta \ . \qquad (6.1.2)$$

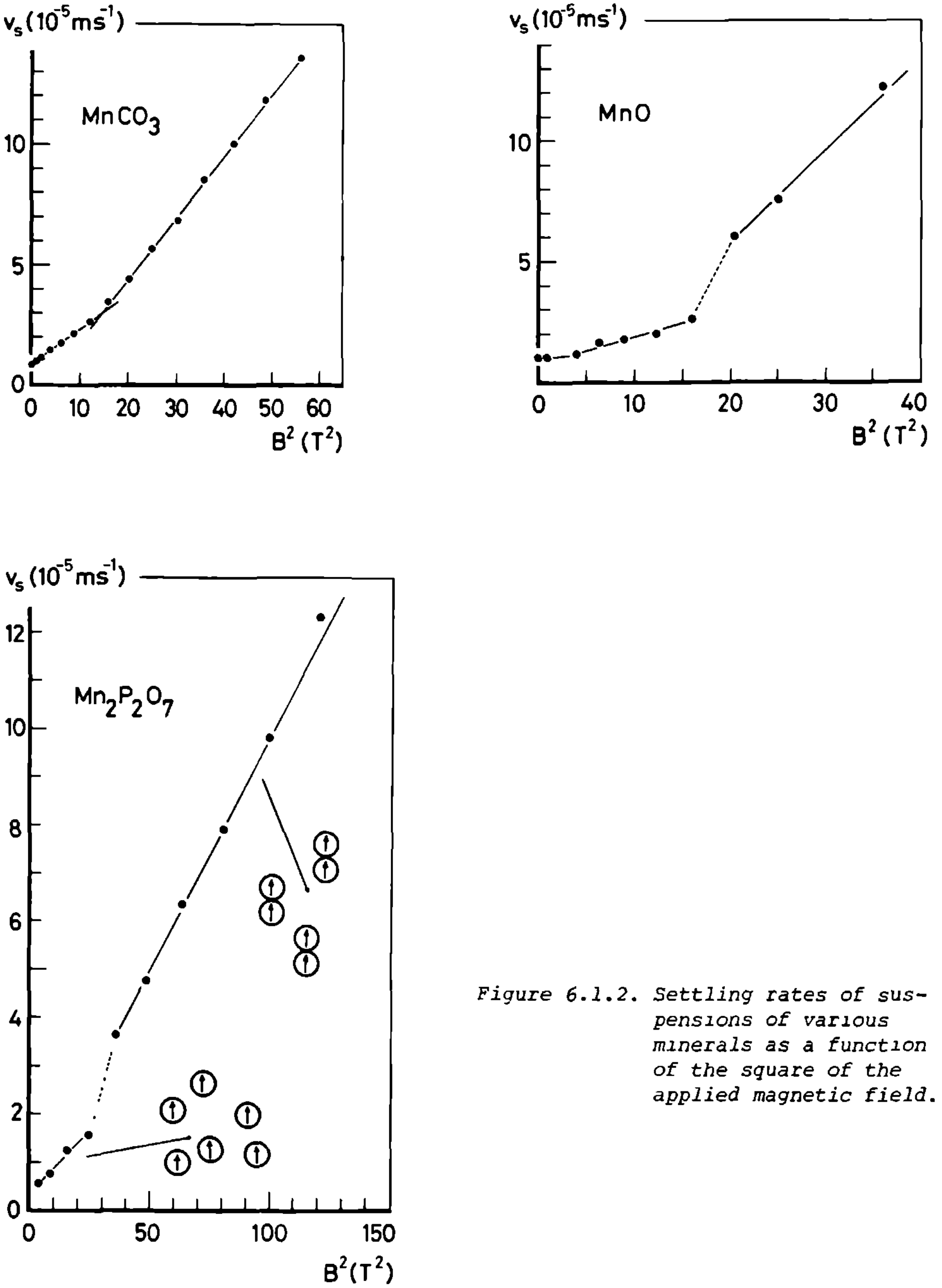

Figure 6.1.2. Settling rates of suspensions of various minerals as a function of the square of the applied magnetic field.

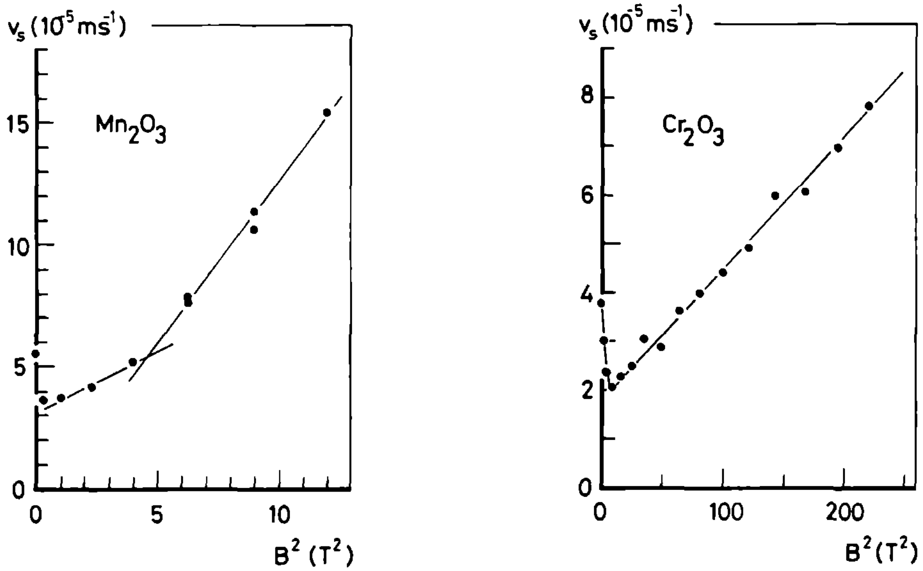

In a fluid medium of viscosity η, the related relaxation time for magnetic orientation will be of order

$$t_M \sim 6\mu_0\eta/(\chi_\perp - \chi_\parallel)B_0^2 \ . \qquad (6.1.3)$$

It can therefore well be that the minimum in settling rate in suspensions of Cr_2O_3 and Mn_2O_3 is caused by a magnetically induced orientation of the particles, leading towards a hydrodynamically unfavourable arrangement. Although both Cr_2O_3 and Mn_2O_3 are antiferromagnetic and therefore are expected to exhibit a magnetic anisotropy below the Néel temperature, this does not explain the orientation effect in Mn_2O_3, since room temperature is well above its particular Néel temperature; this in contrast with Cr_2O_3. It could well be that in Mn_2O_3 a certain anisotropy is caused by particle shape. In section 6.3 a more detailed treatment is given of the subject of magnetic anisotropy.

In Figure 6.1.3, the settling velocity of a suspension of α- Fe_2O_3 particles in water is plotted against the square of the applied magnetic field. The experimental conditions were the same as above. Here, no signs of formation

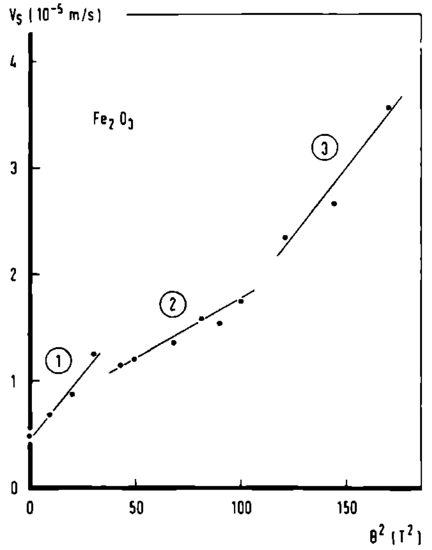

Figure 6.1.3. Magnetically enhanced settling velocity of a suspension of α-Fe_2O_3 particles in water.

of doublets can be observed, which is not surprising because of the strong magnetic properties of α-Fe_2O_3. Calculations show that flocculation can be expected at fields of 0.2 tesla or less, which was below the adjustability of the Bitter magnet. However, the settling behaviour as shown in Figure 6.1.3 is quite different from the other experimental results. The curve may be characterized into three separate parts, of which part 1 is probably connected with the settling of clusters of particles. In part 2 these clusters appear to be breaking up under the influence of hydrodynamic forces at high settling velocities. Finally, in part 3 it seems that more stable clusters are formed, which are capable of withstanding the shear forces, generated by the fluid. Optical examination by microscope shows clear evidence of macroscopic clusters of particles at those high fields. A similar settling curve was also reported by other authors (45).

6.2 Magnetic flocculation of diamagnetic particles

It is clear from the theoretical analysis in the preceding sections that for diamagnetic suspensions, in which χ is negative, the same theory holds, since the magnetic interaction energy is proportional to χ^2. Unfortunately, all diamagnetic materials are of exceedingly small volume susceptibility and because the magnetic interaction in equation (2.4.1) shows a χ^2B^2-dependence, exceedingly high threshold fields for flocculation can be expected. However, if the diamagnetic particles, of volume susceptibility χ_p, are immersed in a paramagnetic liquid, e.g. a solution or melt of a paramagnetic salt with a high volume susceptibility χ_l, the net volume susceptibility of the particles,

$$\chi = \chi_p - \chi_l \, , \tag{6.2.1}$$

can be arranged to be strongly negative. In fact, the diamagnetic properties of the particles are effectively enhanced by the fluid medium.

In this section, a method is presented to study flocculation and in particular the influence of chemical processes on the stability of suspensions, by introducing the external magnetic field as an additional physical parameter.

Studies on magnetic flocculation of diamagnetic particles have been carried out, using suspensions of quartz particles in a solution of $MnCl_2$ in water (46). Five test suspensions were prepared, of equal volume concentration of quartz, but with different concentrations of the paramagnetic salt. The characteristics of the samples are given in Table 6.2.1. The suspensions were held in calibrated test tubes and were placed in the bore of a Bitter magnet, with the fluid meniscus just below the point of maximum field, this in contrast with paramagnetic suspensions which have to be placed above the central field point in order to achieve magnetically enhanced settling. The threshold field for flocculation was determined by the same method as described in section 6.1. Experimental results are shown in Figure 6.2.1, where, for each of the five samples, the settling velocity is plotted against the square of the magnetic field. Here, with all of the five samples, discontinuities are observed which indicate the formation of binary pairs. In each case the slope of the linear curve before and after the discontinuity changes by about a factor 1.5, which is consistent with the approximate model, described in the last section. The experiment was repeated on sample number 3, which led to the observation of a second discontinuity, as is shown in the inset of Figure 6.2.1. Again, the slope changes by a factor 1.5.

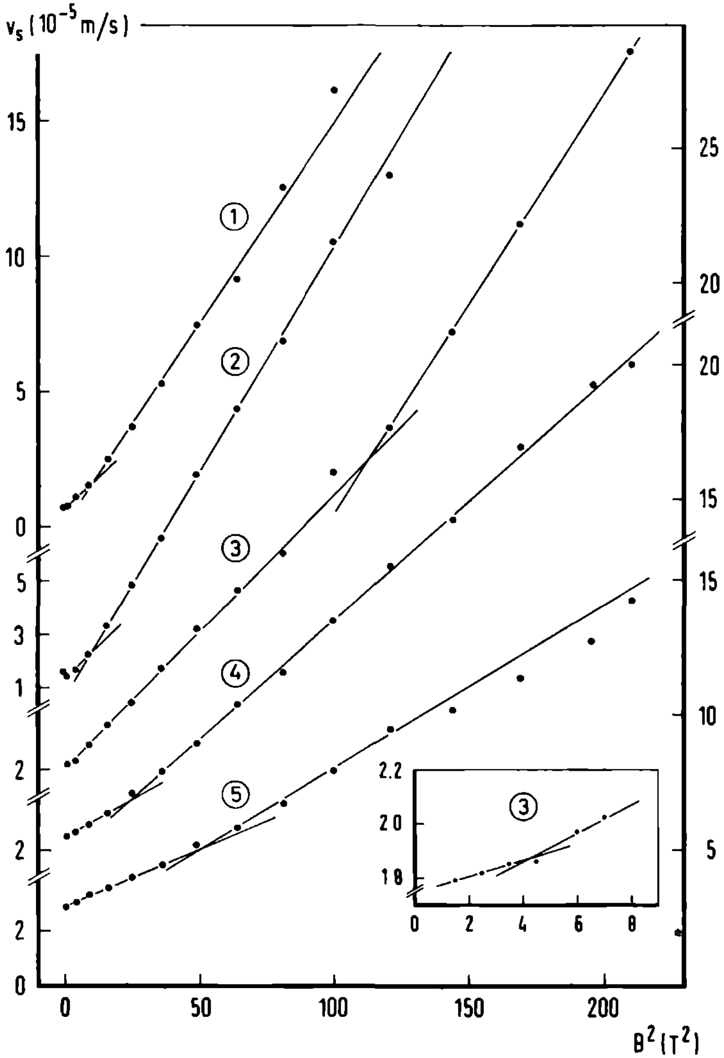

Figure 6.2.1. Magnetically enhanced settling rates of diamagnetic quartz particles in solutions of $MnCl_2$.

The curves are numbered according to the sample numbers in Table 6.2.1.

Table 6.2.1. Characteristics of suspensions of quartz particles in a $MnCl_2$-solution.
Volume susceptibility quartz: $-1.65 \cdot 10^{-5}$ (SI-units)
Volume concentration: 17 %
Particle size: -325 mesh (specified)

Sample number	Concentration $MnCl_2 \cdot 4H_2O$ (wt-%)	Net volume susceptibility (10^{-4} SI-units)	pH	Flocculation threshold field (tesla)
1	50.0	-6.11	3.24	3.5
2	37.8	-4.24	3.93	3.5
3	28.6	-3.03	4.35	2.0 and 10.5
4	20.9	-2.09	4.73	4.5
5	15.4	-1.49	4.93	7.5

Clearly, the influence of the dissolved manganous chloride on the flocculation process is twofold. First, the paramagnetic salt directly determines the magnetic susceptibility of the quartz particles. Second, the double layer potential ψ_o is strongly influenced by specific adsorption of Mn^{2+} ions at the surface of the particles, or better, at the inner Helmholtz plane. As mentioned before, the double layer potential can even change sign when the adsorption process is sufficiently strong. The expression for the double layer potential is of the form (11)

$$\psi_o = \frac{kT}{e} \ln \frac{c}{c_o} , \tag{6.2.2}$$

where c denotes the concentration of potential determining ions at a point outside the double layer, where the electrical potential is zero, and where c_o is the concentration at the zero point of charge. Therefore, c_o is completely determined by the physical properties of the particle system.

In this particular case, the double layer potential is determined by a combination of the pH-value of the liquid and the concentration of the Mn^{2+} ions. Since it turned out that the pH-value of the electrolyte was linearly dependent upon the concentration of manganous chloride, equation (6.2.2) can also be written in the form

$$\psi_o = \frac{kT}{e\ \ln 10}\,(pH_o - pH)\ , \qquad (6.2.3)$$

where pH_o is the isoelectric point (IEP). ($kT/e\ln 10 \approx 1.12\cdot 10^{-2}$ V at room temperature)

It follows from the analysis in sections 2.2 and 2.3 that, since the London-van der Waals interaction does not depend on the concentration of the electrolyte and, anyhow, is very small, ψ_o^2 should be proportional to $\chi^2 B_F^2$, where B_F is the threshold field for flocculation. In Figure 6.2.2, the product of net volume susceptibility and observed threshold field for flocculation is plotted

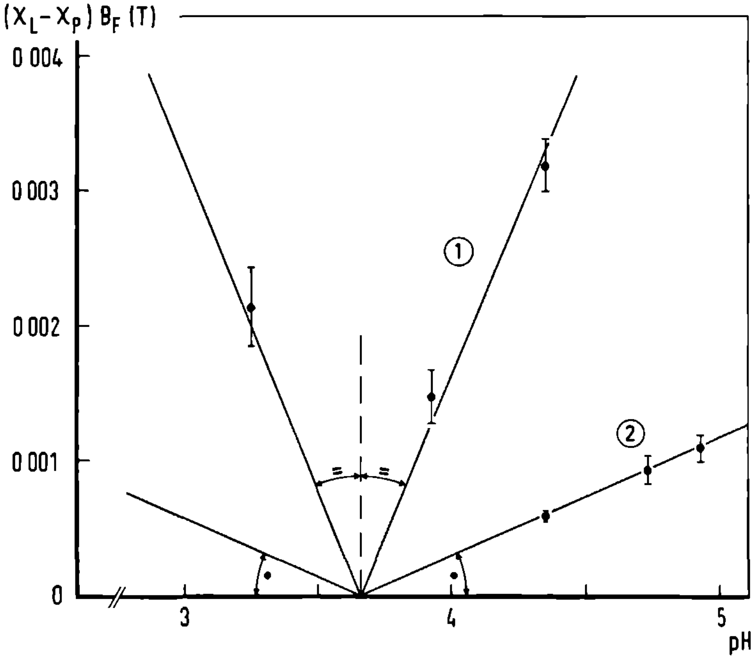

Figure 6.2.2. Product of net volume susceptibility and observed flocculation threshold field as a function of the 'intrinsic' pH-value of the manganous chloride solution.

against the pH-value of the fluid for each of the curves in Figure 6.2.1. According to equation (6.2.3), the pH-value is directly related to the double layer potential ψ_o. Obviously, the observed threshold fields can be divided into two types, which both show the expected linear relation between $|\chi B|$ and $|\psi_o|$, but with different proportionality constants. All branches intersect at a point (3.66, 0), i.e. $B_F=0$ at pH=3.66, the isoelectric point, at which spontaneous flocculation occurs. Since the IEP for quartz in water is $pH_o=2.2$ (47), we may conclude that specific adsorption of cations has shifted the IEP towards a higher pH-value. It can be shown that the slope of the branches in Figure 6.2.2 is proportional to the reciprocal value of the particle radius. The slopes between the branches of type 1 and 2 were found to differ by a factor 5, indicating the presence of two distinct size fractions. Electron microscope pictures of the particulate material indeed confirm this indication, although the size distributions are rather broad.

6.3 The influence of magnetic anisotropy on the settling velocity

As mentioned before, an anisotropic magnetic susceptibility will cause particles to rotate in a magnetic field, until an energetically favourable orientation is achieved. For non-spherical particles, this will lead to a change in their Stokes diameter, which is observable in a sedimentation experiment. Diamagnetic particles will orient themselves with the smaller susceptibility axis parallel to the field. For quartz, the magnetic anisotropy is (48): $\chi_{/\!/} - \chi_{\perp} = -6.68\cdot10^{-8}$ (SI-units), where $\chi_{/\!/}$ and $\chi_{\perp}$ are respectively the magnetic susceptibility parallel and perpendicular to the principle axis of the crystal.

Stott (49) has described magneto-optical effects in graphite colloids, due to the orientation of particles in a magnetic field, in terms of a parameter

$$\alpha^2 = (\chi_{\perp} - \chi_{/\!/})B^2V/2\mu_o kT \ , \tag{6.3.1}$$

which represents the ratio of rotational energy to the thermal energy of the particles. This theory directly applies to the settling of the relatively flat quartz particles used in the above experiments, because of the equivalence between direction of light and direction of settling and between projected area and hydrodynamic area. One can easily show that $(v_s-v_{so})/v_s$ is proportional to $1-m_B$, where $m_B = A_B/A_o$, the ratio of hydrodynamic area with a field B and without

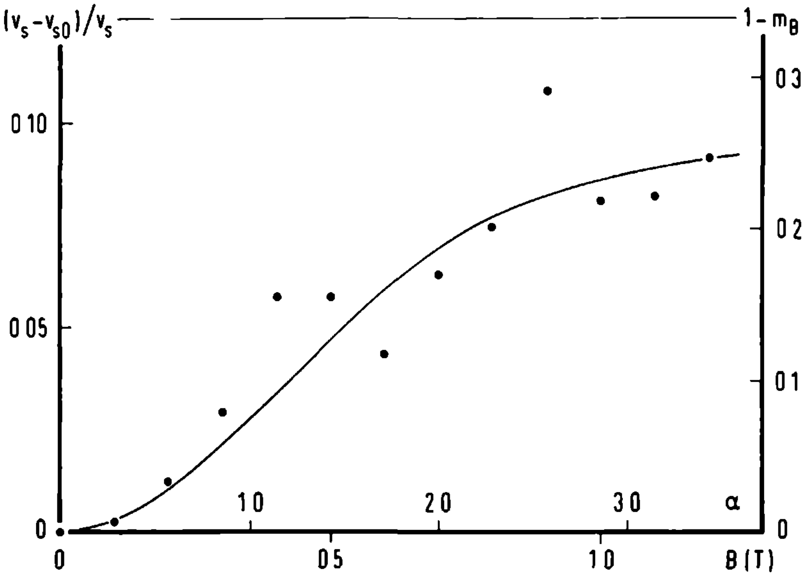

Figure 6.3.1. Normalized differential settling rate of quartz particles in a horizontal magnetic field. The solid line represents the closest fit of the theoretical relation between 1-m_B and α, as discussed in the text.

field and where v_{so} is the settling velocity in the absence of a magnetic field.

The settling velocity of quartz particles, immersed in a solution of $MnCl_2$, in a horizontal magnetic field, was determined and the results are shown in Figure 6.3.1. Note that the concentration of $MnCl_2$ has no influence on the magnetically induced orientation process, since the latter is caused by a *difference* in susceptibility along two crystal axes. The solid line in Figure 6.3.1 represents the closest theoretical fit of 1-m_B against α, using Stott's expression for the case of light normal to the field. From this fit, one obtains a value of α/B, which is proportional to the square root of the particle's volume. For the experiment of Figure 6.3.1, we found for the mean volume of the particles: $V = 1.2\ 10^{-18}\ m^3$, which implies that the particle sizes are in the micron range. Electron microscopy shows that, for a settling suspension, this method under-estimates the actual particle size. This can be due to several facts, like interparticle interaction during settling in a dense suspension, or because of severe deviations from the, theoretically assumed, disc-

Figure 6.3.2. Scanning electron micrograph of quartz particles as used in the experiments. Note the overall tendency to relatively flat particle shapes.

shape of the particles. The latter is illustrated in Figure 6.3.2.

References

1. W. Gestner, J. Oil and Coll. Chem. Ass., 49, (1966), p 954.
2. J. Lyklema in *"Scientific Basis of Flocculation"*, K.J. Ives (Ed.), Sijthoff & Noordhoff, Alphen a/d Rijn, (1978).
3. G.D. Parfitt in *"Dispersion of Powders in Liquids"*, G.D. Parfitt (Ed.), Elsevier Amsterdam, (1969), p 82.
4. J.V. Bondi, R.L. Schnaare, P.J. Niebergall and E.T. Sugita, J. Pharm. Sci., 62, (1973), p 1731.
5. W.D. Corry and G.V.F. Seaman, J. Colloid Interface Sci., 63, (1978), p 139.
6. O. Stern, Z. Elektrochem., 30, (1924), p 508.
7. D.C. Grahame, Chem. Revs., 41, (1947), p 441.
8. G.Gouy, J. Phys. (4) 9, (1910), p 457; Ann. Phys. (9) 7, (1917), p 129.
9. D.L. Chapman, Phil. Mag. (6) 25, (1913), p 475.
10. P. Debye and E. Huckel, Physik. Z., 24, (1923), p 185.
11. E.J.W. Verwey and J.Th.G. Overbeek, *"Theory of the Stability of Lyophobic Colloids"*, Elsevier Amsterdam, (1948).
12. D.Y.C. Chan and D.J. Mitchell, J. Colloid Interface Sci., 95, (1983), p 193.
13. B. Derjaguin, Kolloid-Z., 69, (1934), p 155; Acta Physicochimica URSS, 10, (1939), p 333.
14. R. Hogg, T.W. Healy and D.W. Fuerstenau, Trans. Faraday Soc., 62, (1966), p 1638.
15. J. Lyklema, Adv. Colloid Interface Sci., 2, (1968), p 65.
16. H.C. Hamaker, Physica, 4, (1937), p 1058.
17. H.B.G. Casimir and D. Polder, Phys. Rev., 73, (1948), p 360; Nature, 158, (1946), p 787.
18. J. Visser, Adv. Colloid Interface Sci., 3, (1972), p 331.
19. F. M. Fowkes, Ind. Eng. Chem., 56, (1964), p 40.
20. J.Th.G. Overbeek in *"Colloid Science"*, vol I, H.R. Kruyt (Ed.), Elsevier Amsterdam, (1952).
21. First suggested by C.P. Bean on 21 January 1971 in an informally published document entitled: *"Stability of Colloids in a Magnetic Field"*.
22. J. Svoboda, Int. J. of Mineral Proc., 8, (1981), p 337.
23. J.H.P. Watson, Proc. 6th Int. Cryogenic Eng. Conf., Grenoble (1976), p 223.
24. J. Svoboda and J. Žofka, J. Colloid Interface Sci., 94, (1983), p 37.
25. J. Svoboda, IEEE Trans. on Magn., MAG-18, (1982), p 796.
26. J.H.P. Watson, J. Appl. Phys., 44, (1973), p 4209.

27. M.R. Parker, R.P.A.R. van Kleef, H.W. Myron and P. Wyder, J. Magn. Magn. Mater., 27, (1982), p 250.

28. R.R. Birss and M.R. Parker, J. Magn. Magn. Mater., 15-18, (1982), p 1567.

29. M.R. Parker, R.P.A.R. van Kleef, H.W. Myron and P. Wyder, IEEE Trans. on Magn., MAG-18, (1982), p 1647.

30. R.P.A.R. van Kleef, H.W. Myron, P. Wyder, D. Fletcher, J.P. Glew, M. Rowley and M.R. Parker, IEEE Trans. on Magn., MAG-19, (1983), p 2118.

31. W. Stöber, A. Berner and R. Blaschke, J. Colloid Interface Sci., 29, (1969), p 710.

32. H. Lamb, *"Hydrodynamics"*, Cambridge University Press, (1963).

33. R.P.A.R. van Kleef, H.W. Myron, P. Wyder and M.R. Parker, I. Chem. E. Symposium Series No. 69, (1983), p 83.

34. P.J.J.M. van Mil, D.J.A. Crommelin and P.H. Wiersema, J. Colloid Interface Sci., 98, (1984), p 61.

35. M. Von Smoluchowski, Z. Physik. Chem., 92, (1917), p 129; Phys. Z., 17, (1916), p 585.

36. N. Fuchs, Z. Phys., 89, (1934), p 736.

37. H. Müller, Kolloid-Z., 38, (1926), p 1; Kolloidchem. Beihefte, 26, (1928), p 257.

38. B.V. Derjaguin and V.M. Muller, Dokl. Akad. Nauk. SSSR (English Translation), 176, (1967), p 738.

39. L.A. Spielman, J. Colloid Interface Sci., 33, (1970), p 562.

40. M.R. Parker, R.P.A.R. van Kleef, H.W. Myron and P. Wyder, to be published in J. Colloid Interface Sci.

41. R.P.A.R. van Kleef, H.W. Myron, M.R. Parker and P. Wyder, Proc. of World Filtration Congress III, (1982), p 769.

42. R.P.A.R. van Kleef, M.R. Parker, H.W. Myron and P. Wyder, IEEE Trans. on Magn., MAG-18, (1982), p 1650.

43. G. Barr, *"A Monograph of Viscometry"*, Oxford University Press, London, (1931), Chapter VIII.

44. H. Rouse, *"Elementary Mechanics of Fluids"*, John Wiley, New York, (1946).

45. M.R. Parker and D.R. Kelland, IEEE Trans. on Magn., MAG-18, (1982), p 1653.

46. R.P.A.R. van Kleef, H.W. Myron, P. Wyder and M.R. Parker, J. Appl. Phys., 54, (1983), p 4223.

47. G.A. Parks, Chem. Rev., 65, (1965), p 177.

48. K. Lonsdale, Rep. Prog. Phys., IV, (1937), p 373.

49. F.D. Stott, Proc. Phys. Soc., 7-B, (1949), p 418.

APPENDIX I.

The Magnetic Force between two Spherical Particles

The magnetic field $\vec{H}(\vec{r})$ in the vicinity of a spherical particle of radius a, polarized by a strong external magnetic field H_o, can be described by the relation

$$\vec{H}(\vec{r}) = - \vec{\nabla}\phi(\vec{r}) \ , \tag{AI.1}$$

where $\phi(\vec{r})$ is the magnetic scalar potential.

By considering the known solutions of Laplace's equation in spherical geometry, it may be seen that the magnetic potential of the sphere can be expressed, in polar coordinates, by

$$\phi = Cr\cos\theta + Dr^{-2}\cos\theta \ , \tag{AI.2}$$

where C and D are constants to be determined from the boundary conditions. These boundary conditions at the surface of the sphere require that

1) the tangential component of $\vec{H}(\vec{r})$ is continuous across the boundary between particle and medium and
2) the normal component of the magnetic induction field $\vec{B}(\vec{r})$ is continuous across the boundary.

Inside the sphere, the field is uniform and therefore, according to equation (AI.2), the magnetic potential is given by

$$\phi_1 = - H_1 r\cos\theta \qquad (r<a) \ . \tag{AI.3}$$

Outside the sphere, as $r \to \infty$, the field becomes uniform and equal to the external field H_o and therefore

$$\phi_2 = - H_o r\cos\theta + Dr^{-2}\cos\theta \qquad (r>a) \ . \tag{AI.4}$$

In a polar coordinate system, the above boundary conditions at the surface of the particle can be written as

$$- \frac{1}{r} \frac{\partial \phi_1}{\partial \theta} = - \frac{1}{r} \frac{\partial \phi_2}{\partial \theta} \qquad \text{(AI.5)}$$

and

$$- \mu_1 \frac{\partial \phi_1}{\partial r} = - \mu_2 \frac{\partial \phi_2}{\partial r} , \qquad \text{(AI.6)}$$

where μ_1 and μ_2 are the permeabilities of the particle and of the fluid medium respectively. Equation (AI.5) results in the condition

$$H_1 = H_o - Da^{-3} . \qquad \text{(AI.7)}$$

The radial components of $\vec{B}$ can be written as

$$\mu_o M\cos\theta - \mu_o \frac{\partial \phi_1}{\partial r} = \mu_o (M+H_1)\cos\theta \qquad \text{(AI.8)}$$

and

$$- \mu_2 \frac{\partial \phi_2}{\partial r} = \mu_o (H_o + 2Dr^{-3})\cos\theta , \qquad \text{(AI.9)}$$

for points, respectively inside and outside the sphere. The permeability of the medium is approximated by that of free space, which is valid for all normal fluids.

The magnetic field inside the sphere can be calculated by combining the boundary condition of equation (AI.6) and the expression of H_1 in equation (AI.7), thus leading to

$$\begin{aligned} H_1 &= H_o - \tfrac{1}{3}M \\ &= H_o(1 - \tfrac{1}{3}\chi) , \qquad \text{(AI.10)} \end{aligned}$$

where χ is the volume susceptibility of the particle with respect to the surrounding fluid.

It follows from equations (AI.7) and (AI.10) that

$$\phi_2 = -\left(1 - \frac{a^3\chi}{3r^3}\right)H_o r\cos\theta \ . \tag{AI.11}$$

The radial and azimuthal components of the magnetic field are, respectively,

$$H_r = -\frac{\partial\phi_2}{\partial r} = \left(1 + \frac{2\chi a^3}{3r^3}\right)H_o\cos\theta \tag{AI.12}$$

and

$$H_\theta = -\frac{1}{r}\frac{\partial\phi_2}{\partial\theta} = -\left(1 - \frac{\chi a^3}{3r^3}\right)H_o\sin\theta \ . \tag{AI.13}$$

Neglecting terms of order χ^2, the total magnetic field in the vicinity of the particle can then be written as

$$H^2(r,\theta) = H_o^2\left\{1 + \chi a^3 r^{-3}\left(\frac{1}{3} + \cos 2\theta\right)\right\} \ . \tag{AI.14}$$

It is well-established that the magnetic tractive force $\vec{F}_m$ on a particle of volume V_p and of volume susceptibility χ_p, immersed in a medium of volume susceptibility χ_m and in the presence of a magnetic field $\vec{H}$ is given by

$$\vec{F}_m = \tfrac{1}{2}\mu_o V_p(\chi_p - \chi_m)\ \vec{\nabla}(\vec{H}\cdot\vec{H}) \ . \tag{AI.15}$$

If the particle is spherical and of radius b, then

$$\vec{F}_m = \frac{2\pi}{3}\mu_o(\chi_p - \chi_m)b^3\ \vec{\nabla}H^2 \ . \tag{AI.16}$$

The magnetic force between two spherical particles with radii a and b is obtained by substituting equation (AI.14) in equation (AI.16). This leads to the following expressions for the radial and azimuthal components of $\vec{F}_m$:

$$F_{m,r} = -\frac{2\pi\chi^2 B_o^2 a^3 b^3}{3\mu_o r^4}(1 + 3\cos 2\theta) \qquad \text{(AI.17)}$$

and

$$F_{m,\theta} = -\frac{4\pi\chi^2 B_o^2 a^3 b^3}{3\mu_o r^4}\sin 2\theta \ , \qquad \text{(AI.18)}$$

where $\chi = \chi_p - \chi_m$.

APPENDIX II.

Basic Principles of a Fourth Order Runge-Kutta Method

In the dynamical model of section 3.2, a fourth order Runge-Kutta method was used to calculate the trajectories of a particle from the expressions for the radial and azimuthal components of the particle velocity. In general, a fourth order Runge-Kutta method is used to numerically solve a pair of coupled differential equations of the form

$$\frac{dy}{dx} = F(x,y,z) \qquad \text{(AII.1a)}$$

$$\frac{dz}{dx} = G(x,y,z) \ , \qquad \text{(AII.1b)}$$

with boundary conditions $y(x_o) = y_o$ and $z(x_o) = z_o$.

Starting with these conditions, we can, according to equations (AII.1a) and (AII.1b), find new values for y and z, belonging to a certain value $\bar{x}$, by using

$$y_{n+1} = y_n + \frac{1}{6}(k_1 + 2k_2 + 2k_3 + k_4) + O(h^5) \qquad \text{(AII.2a)}$$

and

$$z_{n+1} = z_n + \frac{1}{6}(m_1 + 2m_2 + 2m_3 + m_4) + O(h^5) \ . \qquad \text{(AII.2b)}$$

Here, $h = (\bar{x}/n)$ and the various parameters k_i and m_i are given by

$$k_1 = hF(x_n, y_n, z_n) \tag{AII.3a}$$

$$k_2 = hF(x_n+\tfrac{1}{2}h,\ y_n+\tfrac{1}{2}k_1,\ z_n+\tfrac{1}{2}m_1) \tag{AII.3b}$$

$$k_3 = hF(x_n+\tfrac{1}{2}h,\ y_n+\tfrac{1}{2}k_2,\ z_n+\tfrac{1}{2}m_2) \tag{AII.3c}$$

$$k_4 = hF(x_n+h,\ y_n+k_3,\ z_n+m_3) \tag{AII.3d}$$

and

$$m_1 = hG(x_n, y_n, z_n) \tag{AII.4a}$$

$$m_2 = hG(x_n+\tfrac{1}{2}h,\ y_n+\tfrac{1}{2}k_1,\ z_n+\tfrac{1}{2}m_1) \tag{AII.4b}$$

$$m_3 = hG(x_n+\tfrac{1}{2}h,\ y_n+\tfrac{1}{2}k_2,\ z_n+\tfrac{1}{2}m_2) \tag{AII.4c}$$

$$m_4 = hG(x_n+h,\ y_n+k_3,\ z_n+m_3)\ . \tag{AII.4d}$$

high gradient magnetic separation and magnetic flocculation of ultra-fine colloids

3

1. High Gradient Magnetic Filtration of Ultra-fine Particles

1.1 A theoretical approach to the capture process of ultra-fine particles

High gradient magnetic separation (HGMS) has made it possible to separate even weakly paramagnetic particles from non-magnetic ones for particle sizes slightly less than 1 µm. Up to now, little work, both theoretical and experimental, has been done on magnetic separation/filtration of ultra-fine particles (<< 1 µm), although the interest in this particular part of separation science is increasing rapidly. One of the major differences in the separation of ultra-fine particles, compared to conventional HGMS, is the fact that the capture process cannot any longer be described in terms of individual particles, since, for decreasing particle sizes, this individuality is gradually lost, due to particle diffusion processes. Therefore, the capture process can best be described in terms of particle fluxes.

Consider a system of particles with number density $n(\vec{r},t)$, which is a function of position and time. Transport processes in such a system are described by the continuity equation

$$\frac{\partial n}{\partial t} + \vec{\nabla}\cdot\vec{j} = 0 \ , \qquad (1.1.1)$$

where $\vec{j}$ is the total particle flux. In the absence of any fluid flow, this flux consists of two components. One component, $\vec{j}_D$, is the flux of particles, due to thermal diffusion, given by

$$\vec{j}_D = -D\vec{\nabla}n \ , \qquad (1.1.2)$$

where D $(= kT/6\pi\eta b)$ is the Einstein diffusion coefficient. The other component of the flux, $\vec{j}_F$, arises from external forces, acting on the particles:

$$\vec{j}_F = n\vec{v} \ , \qquad (1.1.3)$$

where $\vec{v}$ is the drift velocity of the particles, due to the external forces. This drift velocity, of course, can be derived from a force balance equation, comprising the Stokes hydrodynamic force and the total sum of external forces. As a result, equation (1.1.1) can be written as

$$\frac{\partial n}{\partial t} = D\nabla^2 n - \vec{\nabla}\cdot(n\vec{v}) \ . \tag{1.1.4}$$

For a small, spherical non-ferromagnetic particle of radius b and with a net susceptibility χ, in the presence of a ferromagnetic cylindrical fiber of radius a and with a saturation magnetization M_s, magnetized in a uniform magnetic field H_o perpendicular to the fiber, the radial and azimuthal components of the magnetic force are respectively given by (1)

$$F_{M,r} = -\frac{4\pi}{3}\chi b^3 \frac{M_s H_o}{a}\left\{\frac{\cos 2\theta}{r_a^3} \pm \frac{K}{r_a^5}\right\} \tag{1.1.5a}$$

and

$$F_{M,\theta} = -\frac{4\pi}{3}\chi b^3 M_s H_o \sin 2\theta \ , \tag{1.1.5b}$$

where θ is measured with respect to the direction of the field, $r_a = r/a$ and K is a dimensionless parameter, given by

$$K = \frac{M_s}{2\mu_o H_o} \ . \tag{1.1.6}$$

Note that the above equations are expressed in Kennelly SI units, in which the magnetization is measured in units of tesla.

If, to a first approximation, interparticle interactions in the colloid are neglected, the drift velocity in equation (1.1.4) depends totally on the magnetic interaction between particle and fiber. Then, $\vec{v}$ can be expressed in terms of the magnetic velocity v_M, which is given by (1,2)

$$v_M = \frac{2\chi M_s H_o b^2}{9\eta a} \ , \tag{1.1.7}$$

and a magneto-geometrical function $\vec{G}_M(r_a,\theta)$. Along the symmetry direction ($\theta=0$), $\vec{G}_M$ is of the form

$$\vec{G}_M(r_a,0) = \{\frac{1}{r_a^3} \pm \frac{K}{r_a^5}\}\ \hat{r} \tag{1.1.8}$$

and equation (1.1.4) may be solved analitically for steady-state conditions ($\partial n/\partial t = 0$), yielding (3,4)

$$n(r_a) = n_o \exp\{\frac{W}{kT}(\frac{1}{r_a^2} \pm \frac{K'}{2r_a^4})\}\ , \tag{1.1.9}$$

where n_o is the particle number density at $r_a \to \infty$ and W is given by

$$W = \frac{2\pi|\chi|b^3 MH_o}{3}\ . \tag{1.1.10}$$

Here, M is the magnetization of the fibers, K' is $M_s/2\mu_o H_o$ for $H_o \geq M_s/2\mu_o$ and 1 for $H_o < M_s/2\mu_o$. In addition, the plus-sign in the equations (1.1.5), (1.1.8), and (1.1.9) is for paramagnetic and ferromagnetic particles and the minus-sign is for diamagnetic particles. The time dependent solutions of equation (1.1.4) can be found numerically.

It may be noted that, at a given value of the magnetic field, a fixed saturation value n_{sat} of the particle number density at the surface of the fiber (r_a=1) corresponds to a critical value of the particle radius, b_c, given by

$$b_c = \left(\frac{3W_c}{2\pi|\chi|MH_o}\right)^{1/3}, \tag{1.1.11}$$

where W_c can be derived from equation (1.1.9) by substituting r_a=1. Thus,

$$b_c = \left(\frac{3kT\ \ln(n_{sat}/n_o)}{\pi|\chi|MH_o(2\pm K')}\right)^{1/3}\ . \tag{1.1.12}$$

A similar form of this one-third power law has been reported previously for the limiting size of particle capture at domain walls (5) and for a lower particle size limit in magnetically induced flocculation (see Chapter 2, section

4.1 and Reference (6)).

One can now distinguish between three types of particle build-up on the fiber:

1) For larger particles with radii $b>\frac{1}{2}kT/|\vec{F}|$ (3), the conventional HGMS theory applies and a *static* build-up occurs, which is related to a direct physical contact between the particles. Here, $\vec{F}$ is the total force acting on a particle.
2) For $b_c<b<\frac{1}{2}kT/|\vec{F}|$, a combination of static and dynamic build-up occurs. In the case of *dynamic* build-up, particles are captured dynamically, i.e. a cloud of particles is formed around the fiber, in which the particles are free to move and in which a particle number density gradient is present. In this size interval, particles form a static build-up on the fiber, surrounded by a dynamic build-up.
3) Finally, for $b<b_c$, only dynamic build-up takes place.

In the above considerations one assumes that the diffusion constant D and the fluid viscosity η are independent of the particle number density, which, of course, is not true in practice. However, the theory may be generalized to take these effects into account (7). In addition, the above theory does not consider any form of interparticle interaction. Generally, the drift velocity in equation (1.1.4) is related to the total external force acting on the particle, which includes London - van der Waals forces, electrical double layer forces and magnetic forces due to particle-particle and particle-fiber interactions. An attempt to include these interactions is made by Glew and Parker (8,9), who calculated the contours of equal particle number density, *isoplethals*, around a fiber. To distinguish between static and dynamic build-up they use the (arbitrary) criterion that, for dynamic build-up, the increase in total potenial energy of a particle of radius b, when it is moved away from the fiber by a distance 2b, should be larger than kT. The static and dynamic isoplethals are shown to be clearly influenced by surface forces between the particles (8,9).

It has been argued recently (10), that the effect of electrical double layer interactions can be accounted for by introducing an additional term in equation (1.1.4) of the form

$$\vec{\nabla}\cdot(D^{*}\vec{\nabla}n) , \qquad (1.1.13)$$

where the Fletcher-Parker double layer diffusion coefficient D^{*} is given by

$$D^{*} = \frac{(8\pi/3)(\varepsilon_r \varepsilon_o \psi_o^2 \; \delta r)(3\zeta/4\pi)^{2/3}}{6\pi\eta b} . \qquad (1.1.14)$$

Here, ζ expresses the colloid concentration as a volume ratio and δr is the differential nearest neighbour separation along the direction of the density gradient.

1.2 Preparation of ultra-fine colloids

Colloidal dispersions of ultra-fine particles are commercially available in the form of ferrofluids. However, two properties of ferrofluids make them less suitable for the experimental investigation of high gradient magnetic filtration of ultra-fine particles. First, they exhibit a ferromagnetic (superparamagnetic) behaviour with a low saturation magnetization and second, they are stabilized by means of surfactants. Therefore, their stability properties are not as well-defined as for aqueous dispersions of particles (see Chapter 2) and in addition, stability cannot be varied with comparable simplicity. Consequently, we had to produce suitable colloids ourselves, which would satisfy the following conditions. The (water-based) colloids had to be stable for long periods of time, the particle sizes had to be appreciably smaller than the diffusion limit and finally, the magnetic properties of the colloids had to be such that an intermediate value for the recovery of the particles in a filtration experiment could be expected over a field interval, ranging from zero to at least 8 tesla. Satisfactory results were obtained with colloids of CuO. The preparation of the colloids started with ball-milling of the CuO-powder for a period of 24 hours to reduce the number of coarse particles (> 1 μm). A high-speed centrifugal ball-mill was used, with agate milling equipment. Afterwards, the particles were dispersed in distilled water, containing 2.00 gl^{-1} $Na_4P_2O_7 \cdot 10H_2O$ as an ionic dispersing agent, and prefiltered to remove the large particles. Subsequently, the colloids were filtered with membrane filters (Schleicher & Schull). In this way we could produce CuO colloids with particle sizes >3 μm, <3 μm, <0.6 μm, <0.45 μm, and <0.2 μm. The concentration of CuO in these colloids varied between 0.5 and 1.5 gl^{-1} (0.0078 % - 0.023 % (v/v)). Unfortunately, it was not possible to obtain colloids with well-defined particle sizes, i.e. particle sizes within a certain size interval. This, because the residue on the sub-micron filters could not be redispersed.

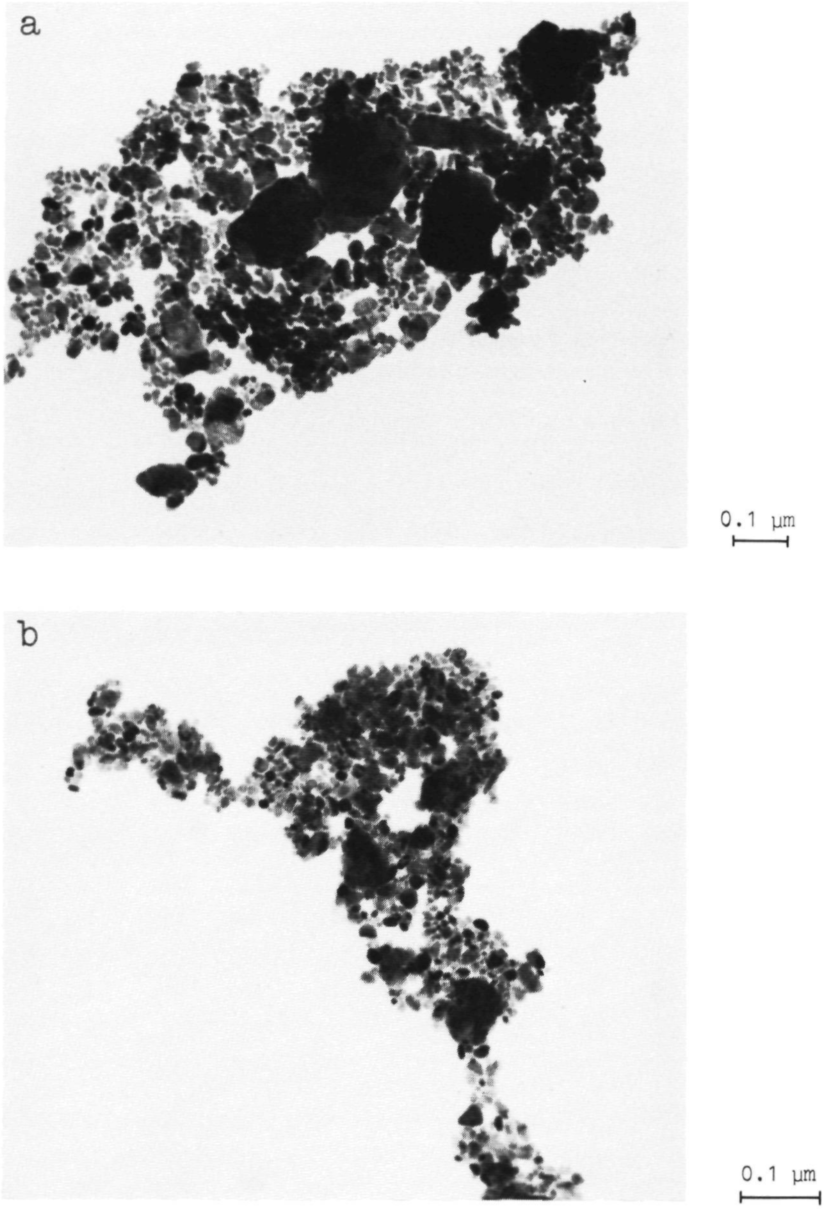

Figure 1.2.1. Transmission electronmicrographs of CuO colloids. The aggregation has most probably occurred during the preparation of the microscope grid.

a) Prefiltered colloid. Clearly, relatively large particles are still present.

b) Filtrate of a 0.45 μm membrane filter.

Figure 1.2.1 c) *Tails of an HGMF experiment at 2 T.*

In practice it is very difficult to obtain reliable data on the actual particle size distribution of the colloidal particles. Because the expected mean particle size is such that, with respect to the scattering of visible light, neither Rayleigh scattering nor Mie scattering is applicable, we decided to use electronmicroscopy to determine the particle size distributions.

However, in order to employ electronmicroscopy on colloids, the particles, dispersed in the electrolyte have to be deposited on a formvar film (polyvinylformaldehyde), which covers the microscope grid and which has to be dried before the grid can be inserted in the vacuum chamber of the microscope. The major problems encountered with respect to electronmicroscopy are related to these two aspects of sample preparation, since at these stages, particles are induced to aggregate. Several preparation techniques were used, such as, among others, spraying of the colloid on the grid, followed by either air-drying or freeze-drying. In each of the cases, however, the particles had formed large clusters on the surface of the formvar film. The best results were obtained by adding an aqueous solution of polyethyleneglycol 20,000 to the colloid, to a final concentration of 0.1 gl^{-1} and transferring a droplet of this mixture to the microscope grid, which was allowed to dry in air. Typical examples of the results of this preparation method are given in Figure 1.2.1 for three colloids of CuO. Clearly, aggregation of particles has occurred, but we have reason to believe that this has taken place during the preparation of the microscope grid and that hence these clusters were not present in the original colloid. First, the size of the clusters is such that they would not have been dispersed by Brownian motion and therefore they would not have been present in the colloid because the sediment in a storage vessel is always removed before starting an experiment. Second, the particles appear to be deposited on the surface of the formvar film in a monolayer. This is very unlikely to happen with particles which already had aggregated in the colloid. Finally, one can remark that the clusters in Figure 1.2.1 have a very porous structure, which is undoubtedly related to instability of the colloid, while the original colloids appeared to be very stable and stayed well-dispersed for periods longer than six months. Therefore we may seriously expect that the particles, present in the colloid are the individual particles appearing on the electronmicrographs of Figure 1.2.1. In the prefiltered colloid, clearly, relatively large particles are still present, this in contrast to the filtrate of a 0.45 µm membrane filter. In the tails of an HGMF experiment at an applied field of 2 T, only small particles can be observed (average particle size: 20 nm).

In order to check the above conclusions with respect to electronmicroscopy by an independent determination of the average size of the particles present in the colloid, the extinction of light by a <0.2 µm CuO colloid was measured on a spectrophotometer. From these data, a wavelength interval could be determined in which the turbidity decreased proportional to, approximately, the fourth power of the wavelength (Rayleigh-type scattering). In this interval, the average particle size could be determined from the experimental data (11), yielding $b \simeq 80$ nm. A more careful analysis (12), involving more terms in the expression for the specific turbidity of the colloid yielded for the average particle radius $b \simeq 20$ nm. Thus, the results of electronmicroscopy and optical techniques are consistent.

1.3 Experimental

In order to investigate the process of high gradient magnetic filtration of ultra-fine colloids in high magnetic fields, a special arrangement was built, which could be operated at very low fluid velocities and which only required small amounts of colloid. The high gradient magnetic filter consisted of a

Table 1.3.1. A characterization of the matrix materials and the colloids, used in the HGMF experiments.

Matrix type	Fiber diameter (μm)	M_{sat} (A/m)
Stainless steel wire (AISI 430)	50	$1.34 \cdot 10^6$
Bekinox 316 L	12	$7.11 \cdot 10^5$
Bekinox 316 L	8	$8.30 \cdot 10^5$

Colloids: Aqueous dispersions of CuO.
Concentration CuO: 0.5 - 1.5 gl^{-1}.
Concentration dispersant (TSPP): 2.00 gl^{-1}.
CuO: $\rho = 6400 \ kgm^{-3}$
$\chi_v = 2.64 \cdot 10^{-4}$.

small glass canister, filled with the matrix material. The matrix compartment was closed by flat plates of porous sintered glass, which also served as flow distributors. An upper limit to the dimensions of the matrix was set by the dimensions of the relatively homogeneous part of the magnetic field. Typically, the canister was 10 mm in diameter and 30 mm in length. In some cases a filter length of 60 mm was used but at high fields, effects due to a contraction of the matrix could clearly be observed. The colloid was pumped through the matrix by a variable-speed peristaltic flow inducer, via 1 mm inner diameter flexible tubes. Although the pump speed was controlled by an optical tachometer, the flow rate gradually increased during a measurement, due to wear of the tubing. Therefore, the flow rate was measured before and after each filtration run and the experimental results were corrected accordingly. The total deviation in flow rate, however, never exceeded 20%, over a measuring period of more than four hours. The matrix consisted of a random arrangement of stainless steel micro-fibers of which the specifications are given in Table 1.3.1. The packing fractions were of the order of 5%. An impression of the filtration efficiency of HGMF is given in Figure 1.3.1, for a colloid of CuO particles.

During a filtration run, samples were taken from both the feed material and the tails, which were analysed at a later stage. When a sufficient amount of colloid was collected (usually one or two canister volumes), the magnetic field,

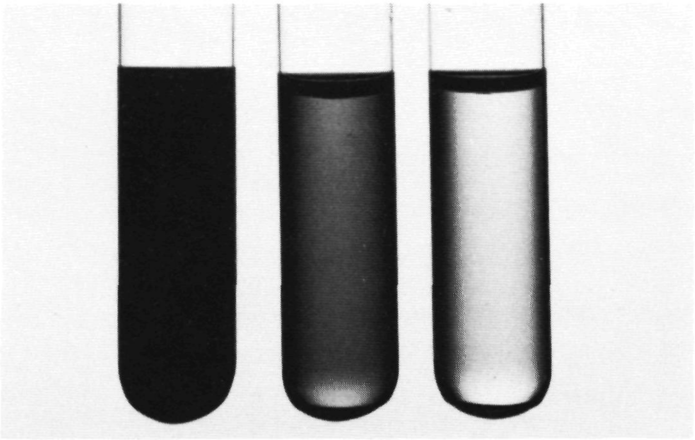

Figure 1.3.1. High Gradient Magnetic Filtration of a CuO colloid. From left to right: Original colloid (feed) and tails at applied magnetic fields of respectively 5 and 10 T.

generated by a Bitter magnet, was switched off and the matrix was rinsed thoroughly by backflushing with water, containing the same concentration of dispersing agent as the colloid itself. After this, the next filtration run was started. The sample of the tails was not collected until several canisters of fresh colloid had passed through the matrix. This to avoid a dilution of the tails by flush water which is still present in the filtration system (canister and tubes) at the start of a new run and which, because of the very low fluid velocities, is not removed until after quite some time.

The filtration performance is expressed in terms of *recovery*, which is determined from the concentrations of CuO in the tails and in the feed. These concentrations, as mentioned above, typically of the order of 1 gl^{-1} for the feed, were measured very accurately by an atomic flame absorption technique on a Perkin-Elmer type 372 spectrometer. For this purpose, the CuO was dissolved by addition of nitric acid, after which the Cu^{2+} concentration was determined by measuring the absorption at a wavelength of 324.8 nm.

1.4 Preliminary Results and Discussion

It is well-established that the capture efficiency E (recovery) of a magnetic filter can be expressed, in terms of the concentration of particles entering and leaving the filter, by

$$E = \frac{c_{in} - c_{out}}{c_{in}} , \qquad (1.4.1)$$

where,

$$c_{out} = c_{in} \exp(-\xi r_{ca} F L_a) . \qquad (1.4.2)$$

Here, $r_{ca} = r_c/a$ is the capture radius of a single fiber, normalized with respect to the fiber radius a, F is the packing fraction (i.e. the ratio of volume, occupied by the filter material, and total volume of the matrix), $L_a = L/a$ is the normalized filter length and ξ is a geometrical factor. For ordered matrices in the longitudinal case (field parallel to fluid velocity), the filter constant is $\xi = 2/\pi$ (13,14). For random filters it is not a simple matter to calculate the filter constant since this involves the evaluation of magnetic depolarization effects in random arrangements. Watson (1) has approximated a random arrangement of fibers by assuming that one-third of the fibers is directed parallel to the field, and therefore ineffective in the filtration process, and two-thirds of the fibers are aligned orthogonal to the field. In this approximation the filter constant is shown to be $\xi = 4/3\pi$ (1). Experimentally determined values of the capture radius, however, appear to be an order of magnitude lower than those, calculated on the basis of the above considerations. More sophisticated calculations have been reported by Birss et al. (15) and by Sheérer et al.(16).

According to equations (1.4.1) and (1.4.2), the recovery of a magnetic filter can be expressed as

$$E = 1 - \exp(-\xi r_{ca} F L_a) . \qquad (1.4.3)$$

It is well-known that the capture radius r_{ca} is dependent upon a certain power of the ratio of magnetic and competing forces. Usually, the competing forces are related to hydrodynamic drag and hence proportional to the fluid velocity v_o. By analogy, the magnetic forces are related to a magnetic velocity v_M, given by equation (1.1.7). Thus, the capture radius can be expressed, to a first approximation, by

$$r_{ca} \propto \left(\frac{v_M}{v_o}\right)^{\gamma} \propto \left(\frac{B_o}{v_o}\right)^{\gamma} , \qquad (1.4.4)$$

where γ is of the order of 1/3 (17).

In Figure 1.4.1, the filtration characteristics are plotted of random filters with fiber diameters of 8 µm, 12 µm, and 50 µm. During the experiments, the fluid velocity in the matrix was kept constant at a value of about $2 \cdot 10^{-4}$ ms^{-1} and the field was varied between 1 and 8 tesla. Clearly, the experimental results are consistent with the power law of equation (1.4.4). However, a considerable influence of particle size can be noticed. For relatively large particles (b>1.5 µm), a dependence of the capture radius upon $(B/v)^{\gamma}$ is observed

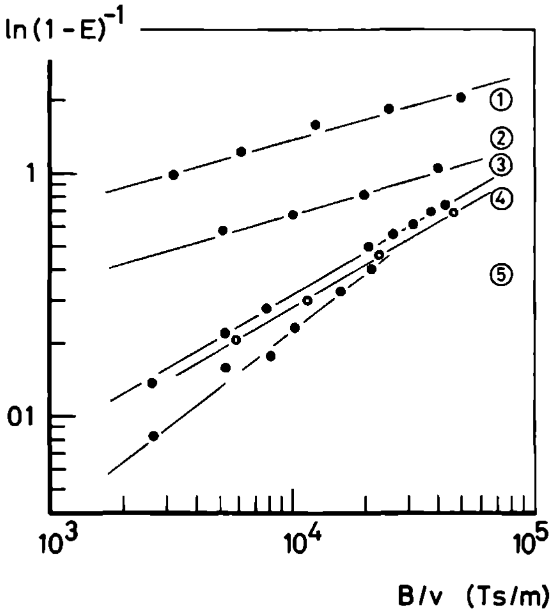

Figure 1.4.1. *Log-log plot of* $\ln(1-E)^{-1}$*, proportional to the capture radius, against the ratio of applied field and fluid velocity for various types of filters (L=3 cm) and particle sizes for colloids of CuO.*

1) a= 4 µm; b>1.5 µm; F=0.04; $v_o=1.6 \cdot 10^{-4}$ ms^{-1}; $\gamma=0.27$.

2) a=25 µm; b>1.5 µm; F=0.06; $v_o=2.0 \cdot 10^{-4}$ ms^{-1}, $\gamma=0.29$.

3) a=25 µm; b<0.3 µm; F=0.04; $v_o=1.9 \cdot 10^{-4}$ ms^{-1}; $\gamma=0.58$.

4) a=25 µm; b<0.1 µm; F=0.06; $v_o=1.8 \cdot 10^{-4}$ ms^{-1}; $\gamma=0.58$.

5) a= 6 µm; b<0.3 µm; F=0.04; $v_o=1.9 \cdot 10^{-4}$ ms^{-1}; $\gamma=0.77$.

with for the value of the power: $\gamma \simeq 0.28$. This is slightly less than the theoretically predicted one-third power law. For the colloids with particle sizes <0.2 µm and <0.6 µm, however, γ appears to be between 0.58 and 0.77. Uchiyama and Hayashi (18) have calculated the capture radius of a single fiber in the longitudinal case for both the potential flow approximation and the viscous flow approximation and predict values of γ in the range between 1/4 and 1/3 for larger values of v_M/v_o (large particle sizes). For the present experimental conditions and for particle sizes smaller than 0.1 µm, v_M/v_o is of the order of 0.01 to 0.1. In this range, the predicted values of γ are considerably larger (γ = 0.5 to 1.0) (18). Thus, the experimental results are quite consistent with this theory. In addition, the overall capture radius is seen to be smaller for smaller particle sizes, as can be expected on the basis of the conventional HGMS theory. Figure 1.4.2 shows similar filtration characteristics for a random filter of 3 cm length and with 50 µm diameter fibers. The packing fraction was 6.2 %. In this figure, results are included of both experiments in which the fluid velocity was kept constant and experiments at constant field. Again, the power law of equation (1.4.4) is satisfied. In accordance with the theory on HGMS for the case of relatively large particles, the capture radius is not

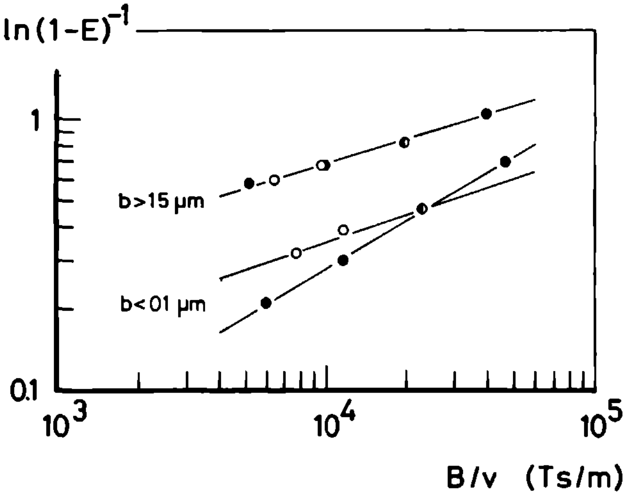

Figure 1.4.2. Dependence of the capture radius on the quantity B_o/v_o for a colloid of CuO. Filtration runs were carried out at constant applied magnetic field (o: $B_o \simeq 4$ T) and at constant fluid velocity (●: $v_o \simeq 1.9 \cdot 10^{-4}$ ms^{-1}).

affected by whether v_M or v_O is varied, as long as v_M/v_O stays constant. However, for the case of small particles (b<0.1 μm), the curves related to filtration runs at constant v_M and thus at constant magnetic field and runs at constant fluid velocity do not coincide. In fact, the values of γ, derived from Figure 1.4.2, are, respectively, $\gamma=0.33$ (B_O=constant) and $\gamma=0.59$ (v_O=constant). Of course, even for small particles, the curves should coincide if only magnetic and drag forces are involved. Therefore, an additional effect has to be present, which only influences the filtration efficiency at small particle sizes. Most probably, such an effect will be related to particle diffusion. For small particles, the diffusion process opposes the magnetic capture process, since the latter is related to creating a higher particle number density in the vicinity of the fiber. As mentioned above, the capture radius in magnetic filtration depends on the ratio of magnetic and competing forces and therefore one can argue that the capture radius should be proportional to $(v_M/(v_O+v_D))^\gamma$, where v_D is a particle drift velocity, related to the diffusion process. It can be shown (19) that the slopes of the two curves in Figure (1.4.2), related to particles smaller than 0.2 μm, are equal for a drift velocity $v_D \simeq 10^{-4}$ ms^{-1}. Velocities of this order of magnitude are far too high to be exclusively caused by thermal diffusion processes. Takayasu et al. (4) obtained from their calculations for particles of 0.1 μm radius a drift velocity of the order of 10^{-6} ms^{-1}. Therefore, a second mechanism has to be present, which induces a diffusion of particles and which is stronger than the thermal diffusion process. Of course, such a process should be related to the double layer interaction between the particles. As is mentioned in section 1.1 of this chapter, the double layer effect has an algebraic similarity to thermal diffusion (10). In addition, the term in the numerator of equation (1.1.14) is much larger than kT.

As a consequence, v_D depends on the stability of the colloid and can be affected by e.g. changing the pH of tne electrolyte. It should therefore be possible, by altering the concentration of dispersing agent, or the pH, to bring the curves of constant velocity and of constant field together. An attempt has been made to show this experimentally, using a filter matrix of 50 μm fibers and with a length of 3 cm. The pH of a part of a stable colloid of CuO (<0.2 μm) was changed by addition of a certain amount of NaOH-solution. As a result, the pH changed from 8.2 (the "intrinsic" pH of the colloid, containing 2.00 gl^{-1} TSPP) to 10.5, while the concentration TSPP in the colloid decreased to 1.96 gl^{-1}. With both the modified and the original colloids, HGMF measurements were carried out, at constant field, as well as at constant

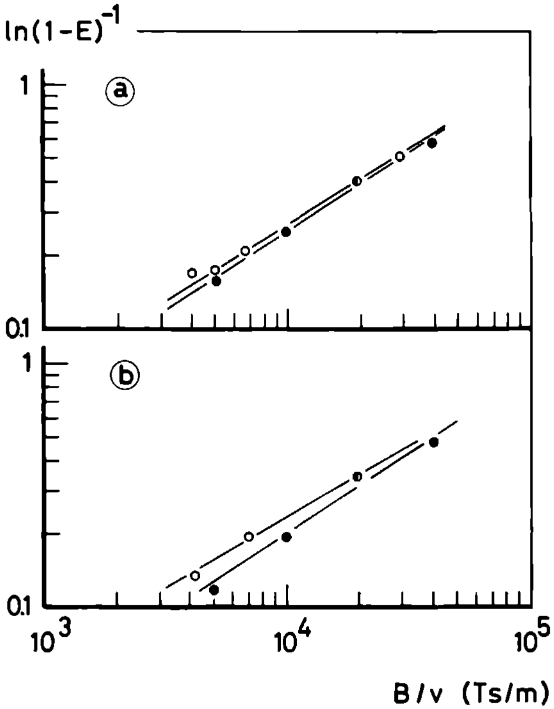

Figure 1.4.3. *Dependence of the capture radius on the quantity* (B_o/v_o) *for a colloid of CuO* (<0.2 μm). *Filtration runs were carried out at constant magnetic field* (o: B_o=4 T) *and at constant fluid velocity* (●: $v_o=2\cdot10^{-4}$ ms^{-1}).
a) pH = 10.5
b) pH = 8.2.

fluid velocity. The results are shown in Figure 1.4.3. Clearly, at a pH of 10.5 the curves of constant velocity and constant field are closer together than at a pH of 8.2. From the difference between the two curves at a certain value of B/v, one can, on the basis of the above considerations, make an estimate of the drift velocity v_D. For the experimental data of Figure 1.4.3, we found $v_D = 1.4\cdot10^{-4}$ ms^{-1} (pH=8.2) and $v_D = 0.5\cdot10^{-4}$ ms^{-1} (pH=10.5). Clearly, these values for the drift velocity are of the right order of magnitude and also, they are dependent upon the pH of the colloid. At present, however, there are not enough experimental data available to draw further, quantitative conclusions.

On the basis of the preliminary experiments, described above, we can conclude that, for ultra-fine colloids, the conventional theory, describing the process of high gradient magnetic filtration/separation, has to be modified in order to explain the observed anomalies concerning the influence of fluid velocity and magnetic field on the capture efficiency. These have been experimentally shown to occur for particles smaller than about 0.1 µm. An explanation is given, which takes into account an additional effect, opposing the magnetic interaction between the particles and the fibers. Clearly, this effect is related to particle diffusion, by which the particles gain an additional drift velocity. However, the effects of thermal diffusion are not sufficiently strong, this in contrast to diffusion effects related to a double layer interaction, that have been shown to be expressible in terms of an additional diffusion constant. The consequent dependence of the drift velocity on the pH of the colloid has been demonstrated experimentally.

Results of a more quantitative nature can be expected from HGMF experiments involving ordered matrices and colloids which are precisely classified in terms of particle size distribution, concentration and ζ-potential. This, however, requires a different method of colloid preparation, preferably by particle growth from a solution or vapour, which also makes it possible to produce smaller particles.

2. Magnetic Flocculation of Ultra-fine Particles

2.1 Introduction

In chapter 2, a review was given of an experimental study on magnetically induced flocculation of relatively coarse (quasi-) paramagnetic and diamagnetic particles. For suspensions with particle sizes larger than one micron, the phenomenon of magnetic flocculation can be observed by measuring the magnetically enhanced settling rate of the dispersion. Since the ratio of particle volume and Stokes radius is different for clusters (doublets) and single particles, a discontinuity in the rise of the settling velocity appears at the threshold field for flocculation. The experimental results show a quite sharp transition to a flocculated state, probably caused by the stimulating influence on the flocculation process of differences in settling velocity of the particles, due to a large particle size distribution.

For colloidal particles (sizes << 1 μm), other methods have to be employed in order to detect magnetic flocculation, simply because, in practice, the sedimentation process is too slow to detect or even absent because the particles are permanently dispersed by Brownian motion. Therefore, we have chosen for light transmission techniques to study the behaviour of paramagnetic colloids in high magnetic fields.

2.2 Preparation of paramagnetic colloids

The colloids used in the light transmission experiments were prepared quite similarly to those used for high gradient magnetic filtration. The main differences in preparation arise from specific requirements, such as a higher concentration and much larger quantities in the case of HGMF and smaller particles in the case of light transmission.

The preparation starts with commercially available powder (usually specified as -325 mesh), which is ball-milled for at least 24 hours in a high-speed centrifugal ball-mill, with balls and jar made of agate. At this stage, the powder becomes slightly polluted with abrasion products of the balls and the jar, but since these mainly consists of SiO_2 (99.91 %), the effect on the magnetic properties of the powder is negligible. In addition, the powder is dispersed in an electrolyte, usually an aqueous solution of $Na_4P_2O_7 \cdot 10H_2O$ (TSPP), and placed in an ultrasonic bath for a few minutes. In order to determine the stability of the colloid, a whole series of test batches is prepared simultaneously, each sample having a different concentration of dispersing agent. Then, the colloids are stored at room temperature in small (50 ml) glass flasks and are allowed to settle for about one week. During this time, the larger particles settle to the bottom of the flask. In stable colloids, the remaining colloid is transparant, sometimes displaying colour bands, related to particle number density. Just before the start of a light transmission experiment, a small sample is taken from one of these layers and transferred to a measuring cell.

Using the preparation method, described above, we were able to produce stable colloids of α-Fe_2O_3, Mn_2O_3, MnO_2, MnO, $Mn_2P_2O_7$, $MnCO_3$ and SiO_2. The best results were obtained for colloids of Mn_2O_3, which stayed in dispersion for periods of months. In Figure 2.2.1, electron microscope pictures are shown of both the original Mn_2O_3 - powder, before ball-milling, and of the colloidal particles, present in the top layer of one of the stable colloids after settling for one week. Obviously, the majority of the individual colloidal particles is smaller than 500 Å.

2.3 Experimental set-up

In order to avoid the drift of particles, due to non-uniformity of the magnetic field, the measuring cell to which the colloid is transferred at the start of a light transmission experiment has to be as small as possible. On the other hand, wall effects lead to a destabilization of the colloid. These effects become stronger with decreasing size of the measuring cell. Eventually, satisfactory results were obtained with a cell of 10 mm diameter, a thickness, along the path of the light, of 2 mm and with 0.1 mm glass windows.

In order to get an impression of the magnetic forces, acting on the colloidal particles, due to non-uniformity of the field, the field profile of the Bitter magnet which was used here was measured with a differential Hall-probe. Thus, we were able to determine the vertical component of the field in the vicinity of the centre of the magnet. The results are shown in Figure 2.3.1, for displacements of one of the probes in both radial (horizontal) and axial (vertical) directions. The origin in the Figures 2.3.1a and 2.3.1b corresponds to the point of maximum axial field. The homogeneity of the field appeared to

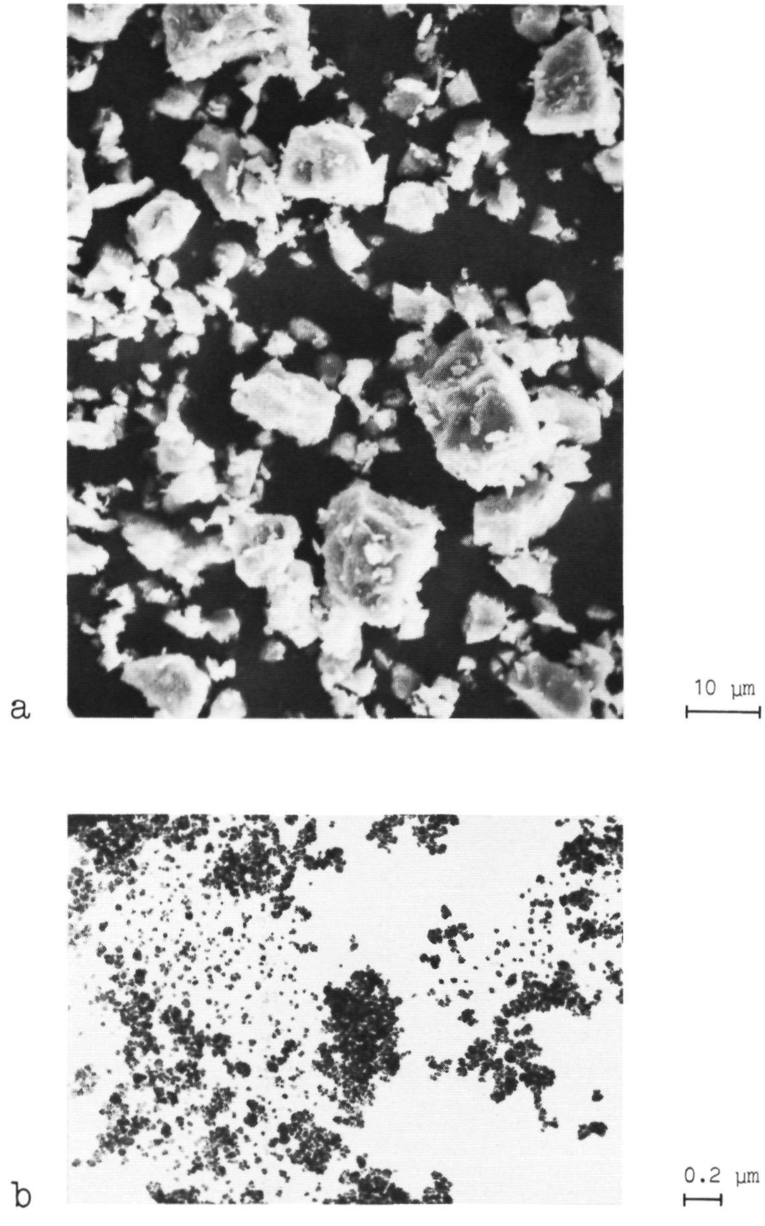

Figure 2.2.1 a) SEM of Mn_2O_3 powder (-325 mesh), before grinding.

b) TEM of Mn_2O_3 particles in a colloid, prepared as described in the text. The formation of clusters has most probably occurred during the preparation of the microscope grid.

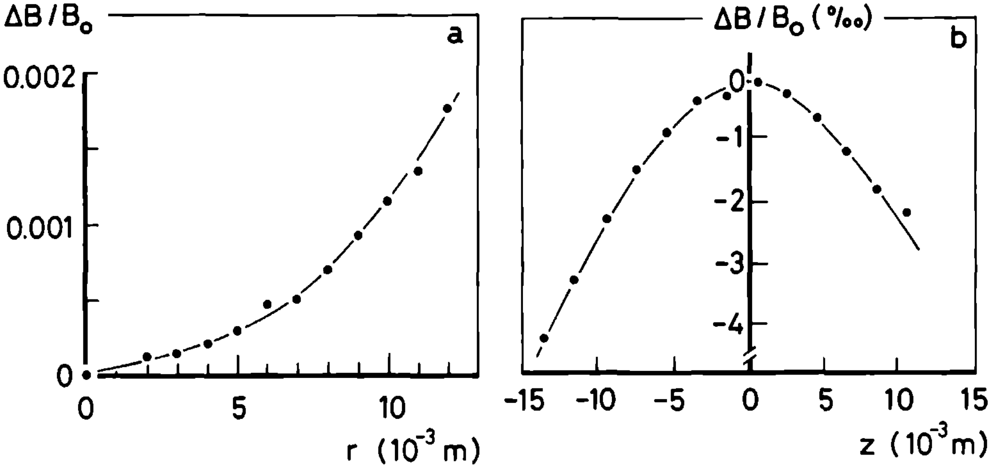

Figure 2.3.1. Field profile near the centre of a 15 T Bitter magnet of the Nijmegen High Field Magnet Laboratory (Bitter stack 830315). The vertical field component was determined relative to its value at the point of maximum on-axis field in both a radial (a) and axial (b) direction.

be better than $5 \cdot 10^{-4}$ over the entire volume of the measuring cell and even better along the path of the light. Hence, a 0.1 µm radius particle will, in an applied field of 15 tesla, gain a drift velocity of at most 0.4 µms^{-1}, which is small compared to Brownian motion.

The behaviour of paramagnetic and quasi-paramagnetic colloids and especially the aspects of magnetically induced destabilization (flocculation) was studied by measuring the extinction of the light through these colloids, parallel to the applied magnetic field. A krypton laser, of which the blue line (476.2 nm) was used, served as a light source. A chopper was placed in the laser beam in order to enable ac-detection of the transmitted light by means of a photocell and a lock-in amplifier. Magnetic field sweeps could be made at nearly any desired speed. For each measurement an upper limit in sweep rate was determined by the RC-time of the lock-in amplifier. Further influence of the sweep rate on the experimental results was not observed. A typical sweep velocity was 2 T per minute.

2.4 Experimental Results

Several light transmission experiments were carried out on colloids, prepared as described above. The field dependence of the transmission was determined in field sweeps with increasing field, as well as with decreasing field. Except for colloids of Cr_2O_3 (on glycerin base) and SiO_2, which are respectively weakly anti-ferromagnetic and diamagnetic, considerable hysteresis effects were observed, i.e. the shapes of the transmission curves differed for increasing and decreasing field, indicating the occurrence of irreversible processes in the colloid. When, subsequently, the measuring cell was removed from its place inside the bore of the magnet, placed in an ultrasonic bath for a few minutes and then re-installed, the transmission curve (i.e. transmission vs. field) was of the original shape, this in contrast with situations in which the samples were not ultrasonically shaken.

Depending on colloid stability, concentration and magnetic properties, several types of transmission curves could be observed. An illustration of this is given in Figure 2.4.1, in which the normalized change in transmission (T_B is the transmission at an applied field B and T_0 the transmission at zero field) of colloids of Mn_2O_3 is plotted against the field. In fact, only the detector signal was recorded, but this signal appeared to be proportional to the intensity of the light that was transmitted to the detector. Also, the detector itself was not influenced by the applied magnetic field, nor by the polarization of the light. The curves in Figure 2.4.1 are obtained from field sweeps (0 to 9 T) at a speed of 2 T per minute, for colloids with different concentrations of the dispersing agent (TSPP). The corresponding concentrations are indicated in grams per litre. Colloids with TSPP concentrations above 0.4 gl^{-1} appeared to be very stable. The colloids with smaller TSPP concentrations were prepared in order to study the influence of a magnetic field on colloids at the "edge" of stability. For all TSPP concentrations, except 0.30 gl^{-1} and, to a less extent, 0.35 gl^{-1}, the transmission rises at low fields, reaches a maximum and subsequently decreases. Then, at higher fields the transmission once more starts to increase, quite rapidly this time. In this region, the transmission keeps rising, even at a constant field, indicating the occurrence of quite drastic processes in the colloid.

The experimental results in Figure 2.4.1 suggest that, basically, the influence of a magnetic field on a colloid can be described by one characteristic transmission curve. Depending on the various aspects of stability, such

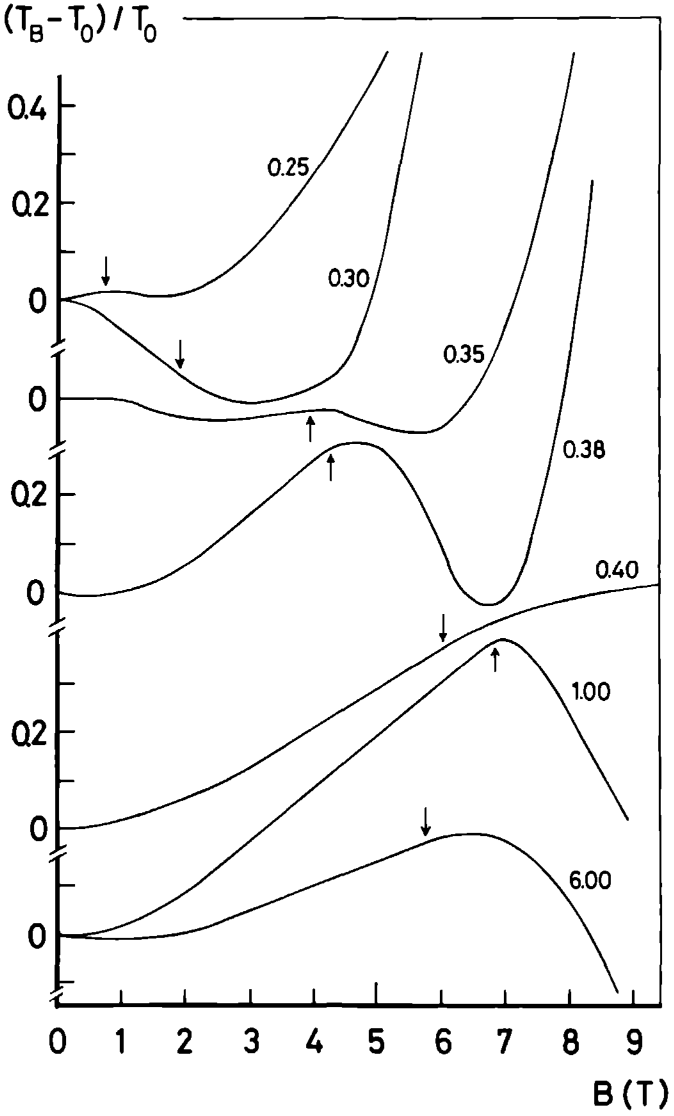

Figure 2.4.1. Transmission curves of Mn_2O_3 *colloids. The normalized change in light transmission with the applied magnetic field is plotted for colloids with different concentrations of dispersing agent. These concentrations are indicated in* gl^{-1}*. The arrows mark the end of a nearly monotonically varying part of the transmission curves.*

as double layer potential (related to the concentration of the dispersing agent), particle size, particle number density and magnetic properties, the various parts of the transmission curve appear at different values of the applied magnetic field. In fact, the first, rising part of the transmission curve of a stable colloid covers a larger field interval than that of a less stable one. Of course, this is just a rough indication, since the various aspects of colloid stability are expected to influence the transmission curve in a rather complex way.

When magnetically induced flocculation occurs in the colloid, initially two-particle clusters will be formed. These will orient themselves with their long axes of symmetry parallel to the magnetic field. The light transmission through the colloid, parallel to the field, is expected to increase, since the total projected area of the particles along the path of the light is decreased, due to a reduction of the number of single particles. We therefore have reason

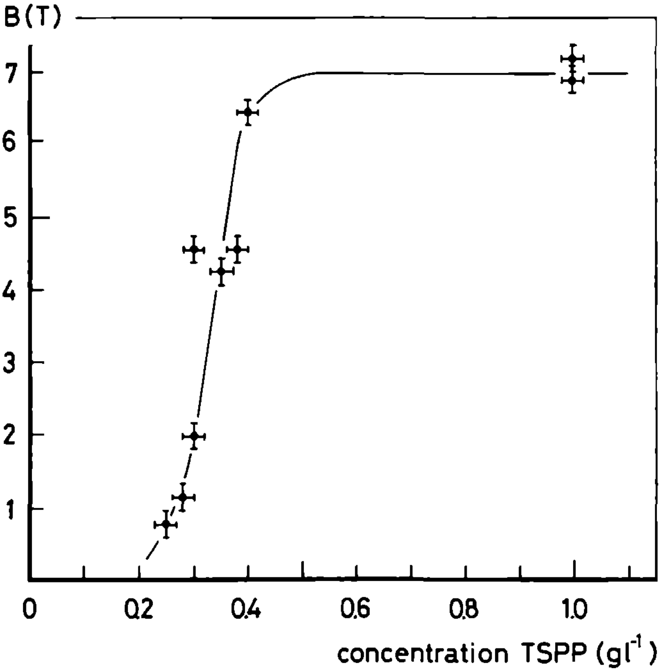

Figure 2.4.2. Values of the applied magnetic field, corresponding to the end of the monotonically varying parts of the transmission curves (see Figure 2.4.1), as a function of the concentration of the dispersing agent in the particular colloids.

to believe that the initial, rising part of the transmission curves in Figure 2.4.1 is related to a magnetically induced flocculation process. This can be illustrated by means of Figure 2.4.2, in which the fields at which the first, nearly linear part of the transmission curve ends, are plotted against the concentration of dispersing agent in the corresponding colloid. Other experimental results than those, shown in Figure 2.4.1 are also included in Figure 2.4.2. Obviously, the curve in Figure 2.4.2 is related to colloid stability, since a less stable colloid requires a smaller magnetic field to destroy the barrier in the potential energy of interaction. In addition, this is confirmed by other, independent observations, such as the turbidity of the colloid after a storage period of a few days. In less stable colloids, interparticle collisions cause the formation of particle clusters, which grow in size until gravitational settling dominates the process of Brownian motion. Therefore, less stable colloids settle down much faster than stable ones and hence their turbidity is lower. The values of the applied magnetic field, appearing in Figure 2.4.2 can, in fact, be identified as threshold field values for a transition to a magnetically induced state of flocculation. This transition, however, is of a different nature and occurs less abruptly than for the case of relatively coarse particles. This will be explained in the following section.

According to the Lambert-Beer law, the optical transmission T of a dispersion of particles is given, to a first approximation, by

$$T = \exp(-nAEd) \ , \qquad (2.4.1)$$

where n is the number density of the particles, A is the projected area of a particle, d the thickness of the cell along the direction of the light and E the extinction factor, through which both the absorption and scattering of the light by a single particle are taken into account.

When a magnetic field is applied, the transmission changes because, due to magnetic flocculation, the number density of the 'particles' changes and in addition because the extinction factor of a single particle and a doublet may differ. Assume that, at a certain value B of the applied magnetic field, a fraction f(B) of the particles are flocculated, i.e. those particles have formed doublets. The colloid then consists of $(1-f(B))n_o$ single particles and $\frac{1}{2}n_of(B)$ doublets per unit volume and the optical transmission can, according to equation (2.4.1), be expressed by

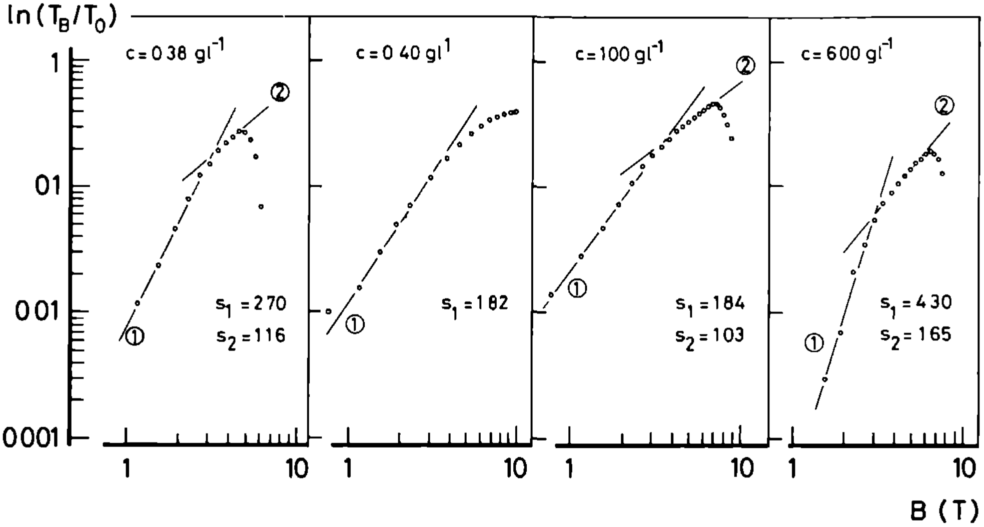

Figure 2.4.3. Dependence of the quantity $\ln(T_B/T_o)$ *on the applied magnetic field for colloids of* Mn_2O_3 *with various concentrations of dispersant. The points are derived from the experimentally determined light transmission in field sweeps up to about 9 T. In each of the cases, the concentration TSPP (c) and the slopes* (s_1) *of the linear parts are indicated.*

$$T_B = \exp\{-dA_sE_s(1-f(B))n_o - \tfrac{1}{2}dA_dE_dn_of(B)\} \ . \qquad (2.4.2)$$

Here, the subscripts s and d stand for, respectively, singlet and doublet. The influence of the applied magnetic field on the optical transmission can now be described by

$$\ln(T_B/T_o) = (A_sE_s - \tfrac{1}{2}A_dE_d)dn_of(B) \ . \qquad (2.4.3)$$

The only field dependent quantity in the r.h.s. of this equation is the fraction f(B) of the particles that are flocculated. According to the kinetic theory, described in section 5 of chapter 2, this fraction is given by the ratio of *isochronal* volume and *equivalent* volume and hence it is proportional to the original particle number density via

$$f(B) = \frac{V_I(B)}{\Omega_o} = \frac{V_I(B)}{2} n_o \ . \qquad (2.4.4)$$

Therefore, $\ln(T_B/T_o)$ is expected to be proportional to the square of the particle number density and to exhibit the same field dependence as the isochronal volume.

In order to investigate these properties, the transmission curves of several stable colloidal dispersions of Mn_2O_3 (c.f. Figure 2.4.1) are plotted on a log-log scale in Figure 2.4.3. A similar curve is shown in Figure 2.4.4, for a stable colloid of MnO_2. Clearly, at low fields, the quantity $\ln(T_B/T_o)$ rises proportional to a fixed power of the magnetic field. Then, at a certain value of the field, this power law is abandonned and a less rapidly rising field dependence is observed. For the colloids with the highest concentrations of dispersing agent, the quantity $\ln(T_B/T_o)$ in this field region seems, once more, to be related to a power law, however with a lower power value. For the

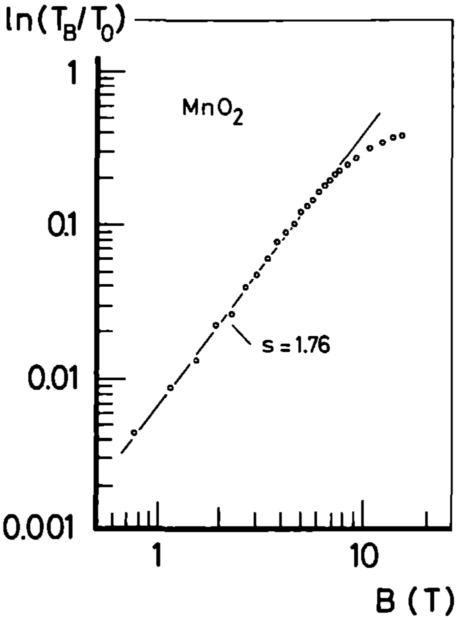

Figure 2.4.4. Dependence of the quantity $\ln(T_B/T_o)$ *on the applied magnetic field in a light transmission experiment, using a stable colloid of* MnO_2.

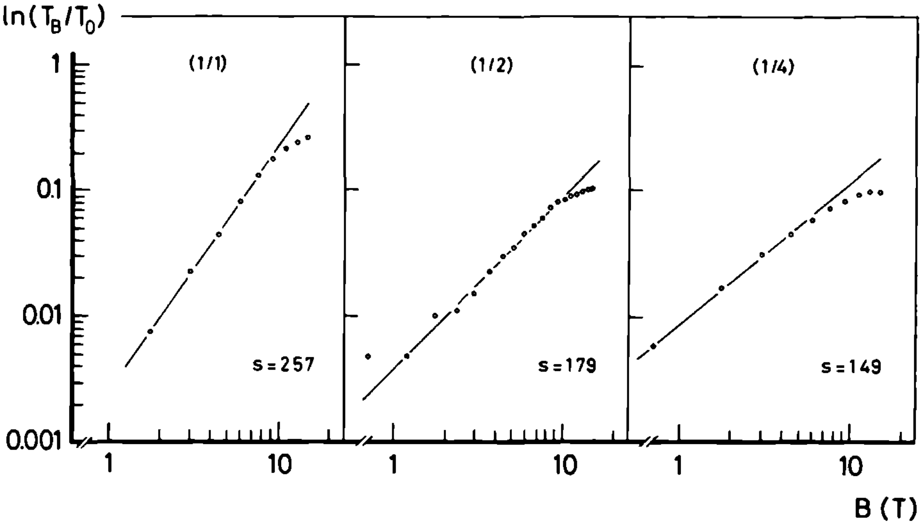

Figure 2.4.5. Dependence of the quantity ln(T_B/T_o) on the applied magnetic field in a light transmission experiment, using stable colloids of Mn_2O_3 (concentration TSPP: 1.0 gl^{-1}. The only difference between the three colloids is the particle number density n: (1/1): $n=n_o$; (1/2): $n=n_o/2$; (1/4): $n=n_o/4$.

MnO_2 colloid, the experimental results (see Figure 2.4.4) show a much larger fixed power region, this in accordance with the weaker magnetic properties of this compound. In addition, the transition fields for the Mn_2O_3 colloids do not show a clear dependence upon electrolyte concentration.

The dependence of the magnetically induced flocculation process on particle number density was investigated by means of three samples of a stable colloid of Mn_2O_3. One sample, (1/1), consisted of the original colloid, a second one, (1/2), was diluted to one-half of the original particle concentration and a third sample, (1/4), to one-quarter of this concentration. The influence of the applied magnetic field on the optical transmission of the three samples was recorded during field sweeps from 0 to 11 tesla, at a sweep rate of 2 T per minute. The experimental results are displayed in the log-log plot of Figure 2.4.5. Again, the low-field region (up to about 7 T) is characterized by a fixed power law, while a deviation from this law occurs at higher fields. Furthermore, the slope of the linear parts in Figure 2.4.5 (i.e. the value of the power in the power law) appears to be dependent upon particle number density.

2.5 Discussion and Conclusions

The kinetic theory of magnetically induced flocculation, as described in chapter 2, section 5, for relatively coarse particles, is not directly applicable to colloids because here, thermal diffusion effects appear. One of the major influences of particle diffusion will be on the capture time parameter, which measures the time, needed for a particle to trace the remaining part of its orbit with respect to the central particle. This, because the diffusion process destroys the direct relation between the release point of a particle and the corresponding capture time, which was one of the basic principles of the kinetic theory. It seems reasonable that, for the case of colloidal particles, the isochronal volume V_I, which is related to the fraction of the particles that are able to flocculate, does not depend on (real) time, but only on the applied magnetic field. Thus, V_I corresponds to the volume around the central particle in which the particles flocculate almost immediately, while outside this volume particles do not flocculate at all. The size of this volume, however, is determined by the magnetic field.

Now, one can try to give a qualitative explanation of the experimental results, shown in the previous section. At relatively low magnetic fields, the modified isochronal volume $V_I(B)$ grows inside the equivalent volume. This corresponds to the linear part of the curves in the Figures 2.4.3, 2.4.4 and 2.4.5. The rate at which the isochronal volume increases with respect to the field, of course, depends on both the magnetic and electrochemical properties of the particles. As can be derived from Figure 5.2.2 of chapter 2, for 1 µm-radius haematite particles, the isochronal volume increases proportional to B^α, where α is of the order of 1.3. For Mn_2O_3 and MnO_2 particles of colloidal sizes, however, α appears to be of the order of 1.8 for highly stable colloids and 2.7 to 4.3 for the less stable ones. This is consistent with the idea that the influence of the field is stronger on a less stable colloid. Furthermore, in contradiction to the kinetic theory, α is seen to depend upon particle number density, which does not appear to be unreasonable since, in the modified picture of the isochronal volume, the diffusion process itself depends on particle number density.

At a given value of the applied magnetic field, $V_I(B)$ has become sufficiently large to extend beyond the surface of the equivalent volume Ω_o, which is inversely proportional to the particle number density n_o. However, the fraction of the particles, capable of flocculating is only proportional to the part of $V_I(B)$ that lies inside Ω_o. This truncated part of $V_I(B)$ still increases with increasing field, but not as rapidly as the total volume. Therefore, at the corresponding field values, the quantity $\ln(T_B/T_o)$, which, according to the equations (2.4.3) and (2.4.4), is proportional to $V_I(B)$, will start to deviate from the observed power law. In the log-log plots of the Figures 2.4.3, 2.4.4 and 2.4.5, this situation corresponds to the field interval in which a gradual deviation from the straight line is observed. The field at which this deviation appears is, as mentioned above, the field at which $V_I(B)$ touches the surface of the equivalent volume and should therefore depend on particle number density. The latter is confirmed by the data in Figure 2.4.5.

For 1 µm-radius haematite particles, the ratio of isochronal volume and equivalent volume is about 0.4 for the case when V_I and Ω_o just touch each other, indicating that 40 % of the particles have flocculated. From the experimental data in the Figures 2.4.3, 2.4.4 and 2.4.5, this fraction can be determined easily, however only with respect to the state of flocculation at the maximum of the transmission curve. When this maximum is identified with complete flocculation, i.e. the complete disappearance of single particles, the fraction of the particles that are flocculated when V_I touches Ω_o are, for the Mn_2O_3 colloids: 47 % ($c=0.38\ gl^{-1}$), 37 % ($c=0.40\ gl^{-1}$), 41 % ($c=1.00\ gl^{-1}$), 26 % ($c=6.00\ gl^{-1}$), 45 % (1/1), 61 % (1/2), 45 % (1/4) and for the MnO_2 colloid: 45 %.

To investigate the dependence of the flocculation process on particle number density, the value of $\ln(T_B/T_o)$, at the field where deviation from the constant power law takes place, is plotted against $\ln(V_o^{-1})$ on a log-log scale in Figure 2.5.1. This is done for each of the three Mn_2O_3 colloids with different dilution factors. Here, V_o is the detector signal at zero field, which is directly proportional to the transmission T_o. $\ln(T_o^{-1})$, in its turn, is proportional to the initial particle number density, according to equation (2.4.1). Since it is difficult to determine the exact point where deviation from the constant power law takes place, the error bars in Figure 2.5.1 are large. The kinetic theory, described in the previous chapter, predicts that the fraction f(B) of the particles that are flocculated is proportional to the particle number density n_o and therefore the quantity $\ln(T_B/T_o)$ should be proportional to n_o^2. The straight line in Figure 2.5.1 is drawn to indicate this condition and clearly, the experimental data are in good agreement with it. We therefore may conclude that the kinetic theory predicts a dependence on particle concentration which also holds in the case of colloidal particles in the presence of thermal diffusion processes.

Finally, the part of the transmission curves in Figure 2.4.1, at higher

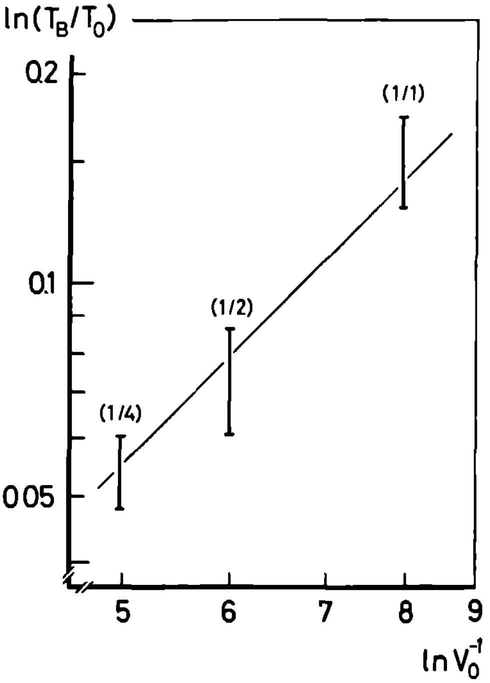

Figure 2.5.1. *Logarithm of the normalized light transmission at the field at which deviation from the linear part of the curves in Figure 2.4.5 takes place, as a function of the logarithm of the observed zero-field detector voltage (proportional to* T_0*), for the same* Mn_2O_3 *colloids as in Figure 2.4.5.*

fields than that, at which the first maximum in transmission appears, is most probably related to a combination of magnetically induced formation of higher-than-binary particle clusters, particle drift and deposition on the optical windows. The fact that, in some colloids, the transmission falls off to a value below its zero-field value before increasing quite drastically, can considered to be an indication of this.

In conclusion, we can remark that the kinetic theory of magnetically induced flocculation is capable of, qualitatively, describing this process in colloids of ultra-fine paramagnetic particles. However, some of the other observed characteristics of the flocculation process are, as mentioned above, not predicted by this, admittedly, rather simple theory.

In addition, one can remark that the observed flocculation events occur at unexpectedly low values of the applied magnetic field. These flocculation events can therefore well be related to flocculation into secondary minima. In the configuration used, i.e. the field parallel to the light, it is not possible to determine the difference between secondary and primary minimum flocculation. However, this does not invalidate the line of argument in this chapter. A better picture, both qualitatively and quantitatively, can certainly be obtained by accurate measurements of the experimental parameters involved (particle size, concentration, double layer potential etc.) and by employing other optical techniques, e.g. with the light orthogonal to the field and techniques such as X-ray small angle scattering.

References

1. J.H.P. Watson, J. Appl. Phys., 44, (1973), p 4209.
2. C.P. Bean, Bull. Am. Phys. Soc., 16, (1971), p 350.
3. R. Gerber, M. Takayasu and F.J. Friedlaender, IEEE Trans. on Magn., MAG-19, (1983), p 2115.
4. M. Takayasu, R. Gerber and F.J. Friedlaender, IEEE Trans. on Magn., MAG-19, (1983), p 2112.
5. R.R. Birss and M.R. Parker, J. Magn. Magn. Mater., 15-18, (1980), p 1567.
6. R.P.A.R. van Kleef, H.W. Myron, P. Wyder, D. Fletcher, J.P. Glew, M. Rowley and M.R. Parker, IEEE Trans. on Magn., MAG-19, (1983), p 2118.
7. R. Gerber, Digests of Intermag Conf., paper FC-01, Hamburg (1984).
8. J.P. Glew and M.R. Parker, Digests of Intermag Conf., paper FC-02, Hamburg (1984).
9. M.R. Parker, Proc. Symp. Electr. Magn. Sepn. Filtr. Techn., Antwerp (1984), p 1.
10. D. Fletcher and M.R. Parker, to be published in J. Phys. D.
11. E.J. Meehan and W.H. Beattie, J. Phys. Chem., 64, (1960), p 1006.
12. H.K. Dettmar, W. Lode and E. Marre, Kolloid Zeitschrift und Zeitschrift für Polymere, 188, (1962), p 28.
13. T.J. Sheerer, Ph. D. Thesis, University of Salford, (1981).
14. R.R. Birss, R. Gerber and M.R. Parker, Filtration & Separation, July/August (1977), p 1.
15. R.R. Birss, M.R. Parker and T.J. Sheerer, IEEE Trans. on Magn., MAG-16, (1980), p 830.
16. T.J. Sheerer, M.R. Parker, F.J. Friedlaender and R.R. Birss, IEEE Trans. on Magn., MAG-17, (1981), p 2807.
17. W.H. McNeese, P.C. Wankat, F.J. Friedlaender, T. Nakano and M. Takayasu, IEEE Trans. on Magn., MAG-15, (1979), p 1520.
18. S. Uchiyama and K. Hayashi, Proc. Int. Conf. on Industrial Applications of Magn. Sepn., Y.A. Liu (Ed.), IEEE Publication No. 78CH1447-2MAG, (1979), p 169.
19. D. Fletcher and M.R. Parker, private communication.

application of selective magnetosedimentation in a continuous flow magnetic separator

4

1. General Introduction

Generally, magnetic separation techniques can be divided into two groups, according to the influence of the magnetic field on the particle - medium system (1).

Magnetic separation techniques of the *first* kind are based on magnetization of the particulate material and the separation is characterized by the inherent magnetic susceptibility of the particles involved. Examples are High Gradient Magnetic Separation (HGMS), High Intensity Magnetic Separation (HIMS) and Open Gradient Magnetic Separation (OGMS).

In magnetic separation techniques of the *second* kind, the medium surrounding the particles is magnetized, rather than the particles themselves. In this case non-magnetic particles can be separated according to differences in their specific density. Examples of techniques belonging to this group are magneto-gravimetric separation (MCM), magnetohydrostatic separation (MHS) and magneto-hydrodynamic separation (MHD). Both MGM and MHS separation techniques are based on creating a levitation force by the magnetized medium. This force is balanced by the gravitational force (2). In MGM, the medium consists of a colloidal dispersion of ultrafine ferro- or ferrimagnetic particles (ferro-fluid). Since the particle sizes are such that each particle contains not more than one magnetic domain, the colloid exhibits a superparamagnetic behaviour. Because of its stability the ferrofluid can be considered as a one-phase system. Its apparent density is determined by the spatial gradient of the applied magnetic field.

In MHS separation (3-9), the fluid consists of a solution or melt of a paramagnetic salt. In this case the medium is a true fluid. Because, in comparison with a ferrofluid, paramagnetic fluids are characterized by a magnetic moment which is a factor 10^3 to 10^4 smaller and which does not show saturation effects, separation by means of MHS forces will also depend on the magnetic properties of the separated particles.

In MHD separation techniques, an electromagnetic thrust force is created in an electrolyte by means of crossed electric and magnetic fields. This force depends on the *electrical* conductivity of both the separated particles and the fluid medium and therefore the separation will be determined by these two quantities together with the net density of the particles with respect to the fluid (3,6,10).

Magnetic separation techniques of the *first* kind can be divided, according to the characteristics of the separation process itself, into a group of particle capture techniques and a group of particle deflection techniques. In this chapter we will mainly consider separation methods belonging to the second group. These techniques, often referred to as Open Gradient Magnetic Separation (OGMS), are based on the fact that particles, moving in a non-uniform magnetic field, experience magnetic forces proportional to their individual magnetic characteristics. These forces tend to deflect them from their original paths, as a result of which they can be collected separately. Magnetic separation techniques of the first group are based on the removal of magnetic particles from a particle stream by entrapment on an appropriate surface by means of magnetic forces. The particles are usually captured on the surface of fibrous ferromagnetic material (e.g. steel wool) of which the filter matrix is constructed. These particles can be collected at a later stage and under different conditions. In practice this means that, except for devices like a carousel type separator (12) or a reciprocating canister separator (13), the separation process is cyclic with a duty cycle of considerably less than ideal. In fact, the duty cycle is defined as the time fraction of a complete cycle in which the separator is in effective operation. For a HGMS system this duty cycle is given by (14)

$$n_o\tau \;/\; (n_o\tau + n_r\tau + D), \qquad (1.1)$$

where n_o is the number of canister volumes of slurry that can be processed before the capture efficiency becomes unacceptably low due to saturation of the matrix and where τ is the residence time of particles in the matrix; i.e. $\tau = L/v_o$ for a matrix of length L and a slurry velocity v_o. When the matrix is saturated it is rinsed, in full field, by n_r canisters of clean water in order to remove non-magnetic particles. Then, the field is switched off to enable the washing of the matrix with high-speed wash water (collection of magnetic particles), after which the field is switched on again for a new separation cycle. The time needed for this complete operation is D. In conventional magnet systems, D is of the order of 100 - 200 seconds. In superconducting solenoids, however, D is several times larger. As a result, the high-field advantage of superconducting magnets is lost through large system dead-times.

The great advantage of open gradient magnetic separation is the fact that it operates in a continuous mode, i.e. the magnetic field is allowed to be constant in time. Here, the magnetic system is not only expected to provide a field of sufficient intensity but, moreover, with a specific non-uniformity in order to create appropriate magnetic forces on the particles. Therefore, the design of the magnet itself is a very important aspect of the total design of the separator.

One of the earliest forms of open gradient magnetic separation is the Frantz Isodynamic Separator (15). In this device the poles of the magnet are especially designed to produce a uniform separating force (isodynamic field) in the gap between the pole pieces. Particles, released inside this gap move downwards under the influence of gravity and are deflected in a lateral direction, according to their magnetic mass susceptibility.

Other forms of open gradient magnetic separation make use of annular quadrupole magnets, either with concentric vertical pipes, the central one for transportation of the slurry and the outer one for collection of the deflected magnetic fraction (introduced by Kolm (14)), or with helical feed pipes, wound spirally around the outer surface of the magnet (16-18).

Nowadays, much attention is paid to OGMS systems provided with a linear multipole superconducting magnet, as illustrated in Figure 1.1.

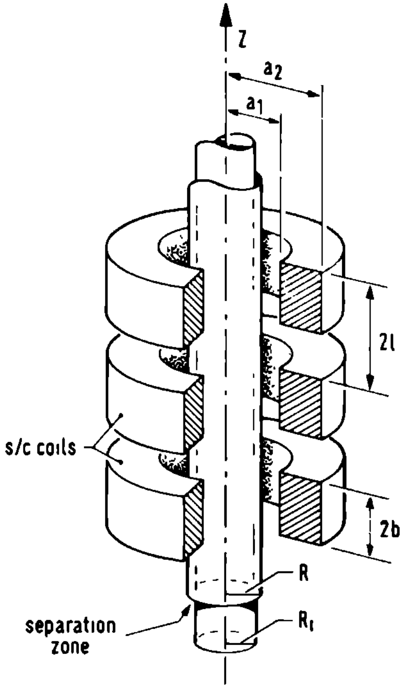

Figure 1.1 Schematic of linear multipole OGMS system (after Schönert et al. (19)).

An annular stream (wet or dry) of particles moves downwards through the bore of the magnet system. Magnetic particles are deflected radially outwards by magnetic forces in the spaces between the various coils, which are energized in opposition. This type of device was first introduced by Shönert et al. (19) for wet OGMS. Several studies, both experimental and theoretical (20-24), have been performed on this and related devices since.

OGMS devices based on separation through a competition between magnetic and centrifugal forces are reported by Eyssa and Boom (25) and Gerhold and Schmidt (26).

A more detailed review on open gradient magnetic separation is given by Parker (27, 28).

2. Aspects of Selective Magnetosedimentation

When a suspension of magnetic particles is placed in the upper half of the field of a vertical-axis solenoid, the particles settle under the combined influence of gravity and a magnetic force due to non-uniformity of the field.

An example of the application of magnetosedimentation in industrial processes is given by Lindley (29), who reported the use of magnetic fields to settle out finely divided Raney Nickel catalyst in chemical reactor vessels.

Experimental studies on non-ferromagnetic particles have shown (30-32) that it is possible to achieve settling rate enhancements of one order of magnitude or more, depending on such quantities as magnetic susceptibility, volume and Stokes' diameter of the particles involved. At applied magnetic fields, sufficiently high to destabilize the suspension and, thus, to induce magnetic flocculation, the influence of the magnetic forces becomes even stronger. This is discussed more completely in Chapter 2.

In heterogeneous suspensions of mixed susceptibilities it is possible to obtain *selective* magnetosedimentation since strongly magnetic particles gain higher magnetically enhanced settling velocities than weakly magnetic ones.

A demonstration of selective magnetosedimentation is given, using a dense aqueous suspension of fly ash, obtained from electrical power plants. Fly ash is composed of various materials, having a wide range of magnetic susceptibilities. Particle sizes from less than one micron up to a few hundred microns are found. In Table 2.1 the chemical composition is given of four types of fly ash, originating from different types of coal but produced by the same small (130 MW) production unit. Suspensions of these four fly ash samples were held in glass tubes, sealed with porous glass filters and placed in the bore of a 15 tesla Bitter magnet, just above the midpoint of the Bitter-coil. In this region of the field, magnetic particles are forced down towards the centre of the magnet. After letting the suspension completely settle out at high field, the remaining clear liquid was removed, still with the field on, via the glass filters. In this way the sediment was fixed, allowing an analysis at a later stage. Figure 2.1 shows the results of selective magnetosedimentation at high fields for each of the four types of fly ash. Clearly, particles with the highest magnetic moments have migrated through the settling suspension towards the energetically most favourable position: the point of maximum field. The black band at this position is most probably composed of (ferromagnetic) γ-Fe_2O_3.

In a sample of a fifth type of fly ash, originating from an unknown type of coal and produced by the Nijmegen electrical power plant, as many as six colour bands appeared after sedimentation at high field (33). This sample was quickly frozen in liquid nitrogen and then cut into slices to separate the different bands. Of each slice the magnetization was measured as a function of magnetic field, from which the relative concentration of the ferromagnetic compounds and the mean susceptibility of the paramagnetic components could be

Table 2.1 Chemical composition (%-wt) of fly ash samples.
(After Sikkenga, Segal, van Driel and Kerkdijk (34))

	Original coal type			
Compound	Germany (Ruhr)	Poland	U.S.A.	Australia
SiO_2	47.1	46.0	58.0	51.7
Al_2O_3	22.2	22.6	28.2	31.0
Fe_2O_3	8.7	7.8	4.8	5.0
CaO	3.4	5.1	1.0	1.4
MgO	3.0	3.38	0.73	0.57
Na_2O	1.0	0.74	0.22	0.10
K_2O	3.9	1.8	1.5	1.4
TiO_2	0.9	1.86	1.61	1.22
SO_3	0.64	0.64	0.21	0.19
C	10.6	3.5	1.4	2.9

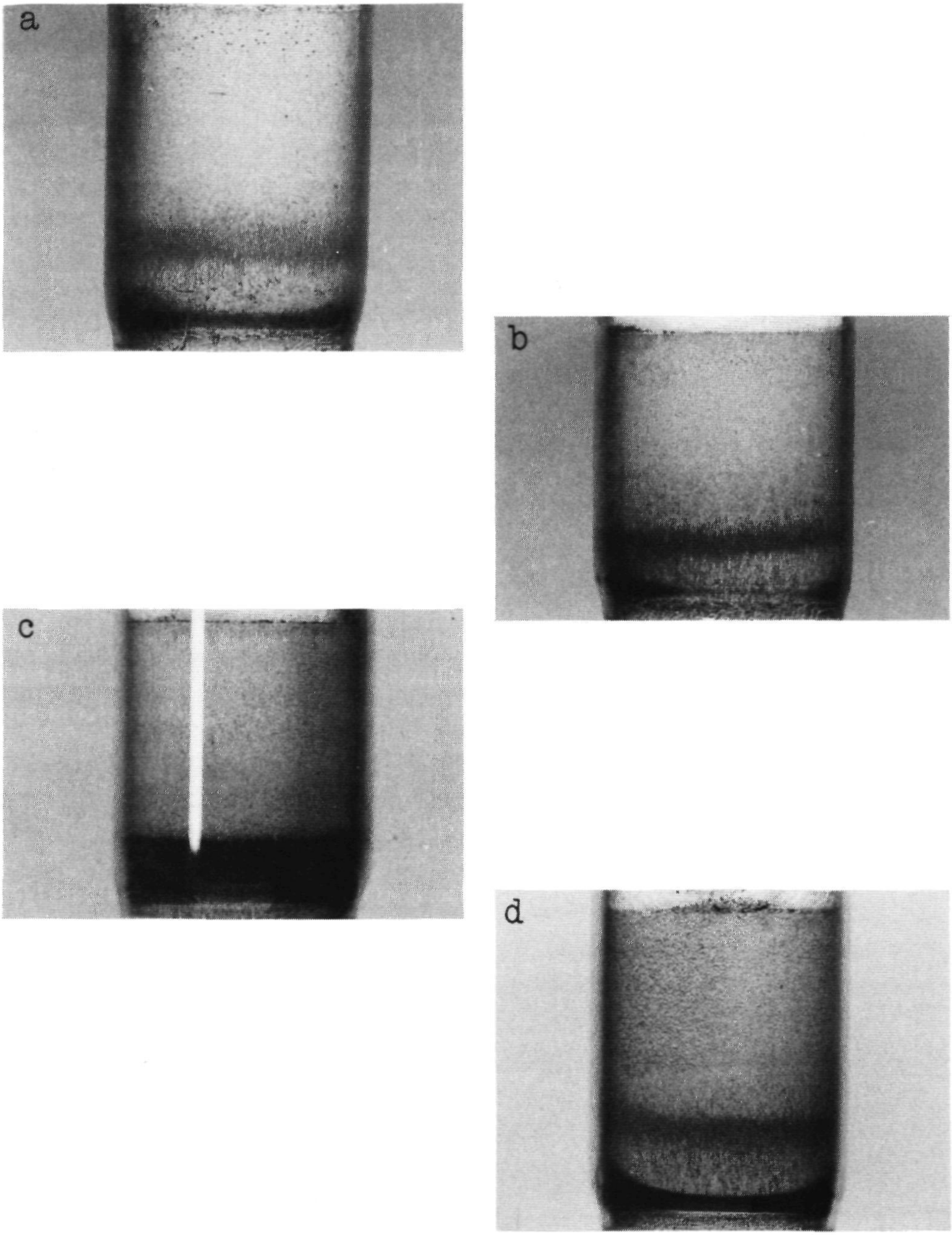

Figure 2.1 Colour bands in suspensions of flyash from an electrical power plant after complete settling in a high magnetic field. Origin of fly ash: a) German coal, b) Polish coal, c) coal from the U.S.A., d) Australian coal.

determined. Results are given in Table 2.2. Clearly, a separation according to magnetic properties has occurred. Practically all of the ferromagnetic material is concentrated in the black band at the bottom of the sample.

In samples that had settled outside the magnetic field no signs of concentration of ferromagnetic material could be observed.

3. Continuous Flow Magnetic Separation

3.1 Operating principles

As mentioned at the beginning of this chapter, the settling rate of suspensions of non-ferromagnetic particles can be enhanced, at field gradients of a few tesla per metre, by more than one order of magnitude. Since the enhanced settling rate depends, among others, on the volume susceptibility of the particles, this criterion can be used to separate magnetic particles from non-magnetic ones by allowing them to settle under the influence of a magnetic force in a fluid stream directed upwards. Magnetic particles will gain a velocity, sufficiently high to actually settle against the fluid stream, while non-magnetic particles are carried away by the fluid. A schematic picture of the separation device is given in Figure 3.1.1. Basically, it is of the type described earlier by Hencl and Svoboda (35), who applied the

Table 2.2 Selective magnetosedimentation of fly ash.
Characteristics of observed colour bands.

Slice number (from bottom to top)	Concentration ferromagnetic material, relative to slice 1.	Susceptibility of paramagnetic component (10^{-6} emu/g)
1	1	27.6
2	0.0131	6.5
3	0.0057	5.5
4	0.0042	5.4
5	0.0032	4.5
6	0.0023	4.0

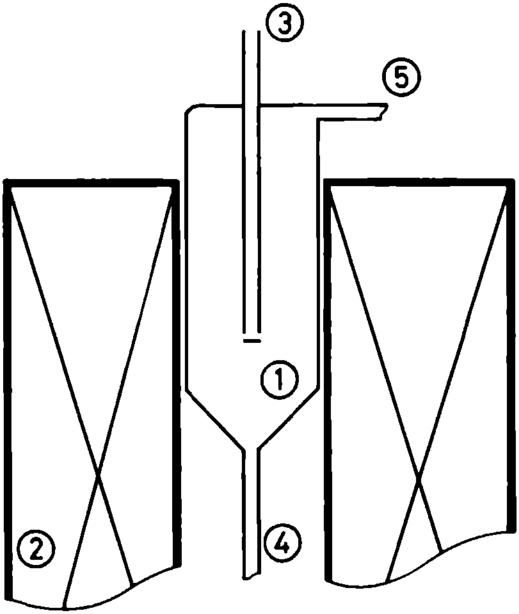

Figure 3.1.1 Schematic of the Continuous Flow Magnetic Separation device. 1) Separation tube, 2) Solenoid-type magnet, 3) Feed pipe, 4) Outlet mags, 5) Outlet non-magnetics (overflow).

homogeneous field of an iron-bound solenoid in order to induce magnetic flocculation of mineral particles. As a test sample they used ground ore, with as main ingredient manganese sideroplesite (83% $FeCO_3$, 11% $MgCO_3$, 5% $MnCO_3$ and 1% $CaCO_3$). Unfortunately, for paramagnetic particles in a homogeneous magnetic field, flocculation causes only a very limited enhancement in settling rate and therefore the separation process is very sensitive to changes in slurry characteristics. In addition, the threshold field for flocculation is inversely dependent upon particle size and susceptibility, which implies that the maximum field available determines a lower limit for both quantities. However, according to the schematic picture of the separator used by Hencl and Svoboda (35), the field cannot be expected to be homogeneous over the whole separation zone because of the large openings in the flux return frame through which the separator was placed in the magnet. Therefore, the separation performance was certainly not, as reported (35), exclusively caused by magnetic flocculation, but also influenced by field gradients (36).

In the separation device of Figure 3.1.1, full advantage is taken of high and, especially, non-uniform magnetic fields. The separation tube (1) is placed in the bore of a solenoid-type magnet (2), in such a way that it is completely above the point of maximum field. A slurry is fed into the device through the feed pipe (3) and enters the separation tube in a radial direction. Here, the ferro- and paramagnetic particles experience a magnetic force directed downwards and leave the tube via outlet (4). The magnetic force on diamagnetic particles is negligible and so they only experience a hydrodynamic force and are carried away by the fluid towards outlet (5) (overflow).

The process of magnetically enhanced settling can be described, in the inertialess approximation, by a force balance equation of the form

$$V(\rho_p - \rho_l)g + V(\chi_p - \chi_l)B\nabla B / \mu_o = 6\pi\eta b_S u, \qquad (3.1.1)$$

where V is the particle volume, $\rho_p - \rho_l$ the net density of the particle with respect to the liquid, $\chi_p - \chi_l$ the net volume susceptibility, g the gravitation constant, B the applied magnetic field, η the viscosity of the fluid, b_S the particle's Stokes radius and u its velocity with respect to the fluid. Equation (3.1.1) can be rewritten as

$$u = \alpha \frac{V}{b_S} (\rho + \rho_M), \qquad (3.1.2a)$$

or, for spherical particles of radius b,

$$u = \alpha' b^2 (\rho + \rho_M), \qquad (3.1.2b)$$

where α and α' are constants and $\rho_M = \chi B\nabla B/\mu_o g$ is the magnetic density of the particle.

3.2 Experimental results

In order to study the feasibility of continuous flow magnetic separation, a laboratory-scale separator of the type shown in Figure 3.1.1 was built. The device was completely made of non-magnetic material, with a 40 mm (inner) diameter separation tube and a 10 mm (outer) diameter feed pipe. The outlet of the feed pipe was situated 100 mm above the midpoint of a 15 tesla Bitter magnet with a 60 mm diameter bore. At this point, the magnetic force density $f_m = \mu_o H\nabla H$ is about maximal. The slurry velocity was controlled by a peristaltic

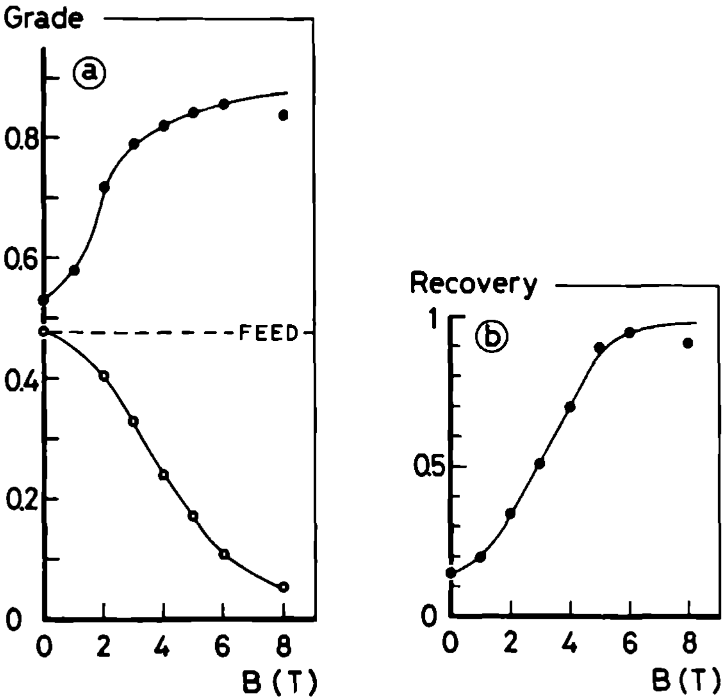

Figure 3.2.1 Grade of the separation products and recovery of $MnCO_3$ in the mags as a function of the applied magnetic field for a slurry of $MnCO_3$ and SiO_2.
●: Mags; o: Overflow.

pump in combination with a restriction valve at outlet (5), by which the system could be pressurized. In order to collect the magnetic fraction (mags), these particles have to be transported from an energetically favourable position at the centre of the magnet to a place outside the field. This was done via a tube with a small inner diameter, which was connected to outlet (4) and cut off by a magnetic valve at a place outside the field. This valve was opened periodically, allowing a small quantity of magnetic material to leave the magnet without seriously affecting the flow in the separation zone. The pressure on the system ensured a high enough flow through this outlet to avoid blockage at high fields.

Systematic separation experiments were carried out using both two-component and multi-component slurries (37-39). The two-component slurries consisted of

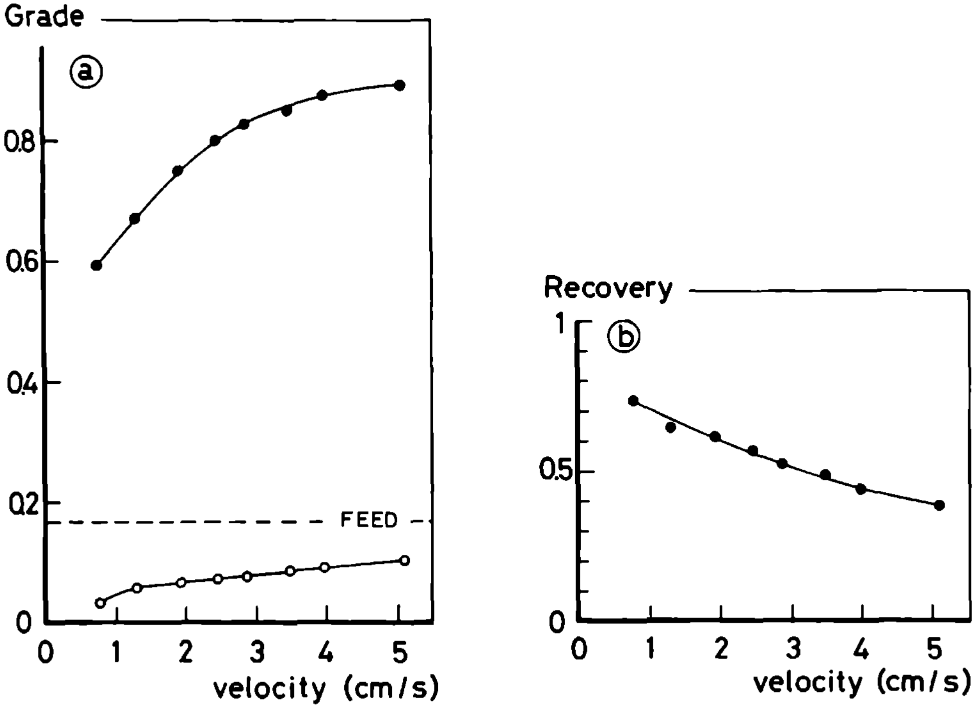

Figure 3.2.2 *Grade of the separation products and recovery of $MnCO_3$ in the mags as a function of fluid speed in the separation zone for a slurry of $MnCO_3$ and SiO_2.*
●: Mags; o: Overflow.

a mixture of paramagnetic $MnCO_3$ and diamagnetic SiO_2. The volume susceptibilities of these compounds are $\chi_V = 4.3 \cdot 10^{-3}$ and $\chi_V = -1.6 \cdot 10^{-5}$ (SI-units) respectively. All material was sieved to a particle size smaller than 38 µm and dispersed in tapwater, without pH-adjustment or addition of dispersants. The slurries were ultrasonically shaken before being fed into the separation device.

In Figure 3.2.1a the grade, i.e. the concentration of magnetic material, of the separation products is shown as a function of the applied magnetic field for a 2.0 % (v/v) test slurry of $MnCO_3$ and SiO_2 in water. The fluid velocity in the separation tube was 16 mms^{-1}. The difference in grade between the separation products at B=0 is caused by gravity separation, due to differences in net density and/or particle size. Clearly, in the grade of the mags, signs of saturation begin to appear at about 3 T, caused by non-magnetic particles which are swept down along with the magnetic ones and collected in the mags. The recovery of magnetic material in the mags, defined as the fraction of magnetic material in the feed which is collected in the mags, is shown in Figure 3.2.1b. For the same experimental conditions the recovery rises until at about 6 T a limit of 0 93 is reached.

The influence of fluid velocity in the separation zone on the separation process was studied, using a 1.5 % (v/v) slurry containing 17 % $MnCO_3$, at a fixed central field of 6 T. The results are shown in Figure 3.2.2, where the grade of the separation products and the recovery of $MnCO_3$ in the mags are plotted against fluid velocity. As could be expected, the grade of the overflow increases with increasing fluid velocity because, starting with the smallest particles, the magnetically enhanced part of the settling velocity is not sufficient to prevent them from being carried away by the fluid. On the other hand, since gravitational settling is less for higher fluid velocities, the amount of non-magnetics in the mags will decrease, resulting in an increase in grade to about 0.90 for u = 50 mms^{-1}.

Obviously, a higher fluid velocity leads to a worse recovery of $MnCO_3$ in the mags, as can be seen in Figure 3.2.2b

Another parameter in the separation process is the grade of the feed. In Figure 3.2.3 the grade of the separation products and the recovery of $MnCO_3$ is plotted against its relative concentration in the feed for separation runs at 6 T and with a fluid velocity of 16 mms^{-1}. The absolute concentration of particulate material in the feed was about 2 % (v/v). Obviously, the recovery is hardly influenced by the grade of the feed.

In addition to changing the grade of the feed at constant slurry concentration, one can vary the concentration of particulate material in the feed at constant feed grade, field value and fluid velocity. The experimental results are shown in Figure 3.2.4a and Figure 3.2.4b, where respectively the recovery of magnetic material in the mags and the grade of the separation products are plotted for a slurry with a relative concentration of 20 % $MnCO_3$. The separation device was operated at a somewhat higher fluid velocity of 18 mms^{-1} in a field of 6 T, generated by a different Bitter magnet as before. The latter could lead to small changes in the separation performance due to a different field profile. As illustrated in Figure 3.2.4b, the slurry concentration hardly affects the grade of the separation products, although the purity of the mags is somewhat higher at low feed concentrations. The recovery, however, reaches a maximum of about 0.90 at slurry concentrations of approximately

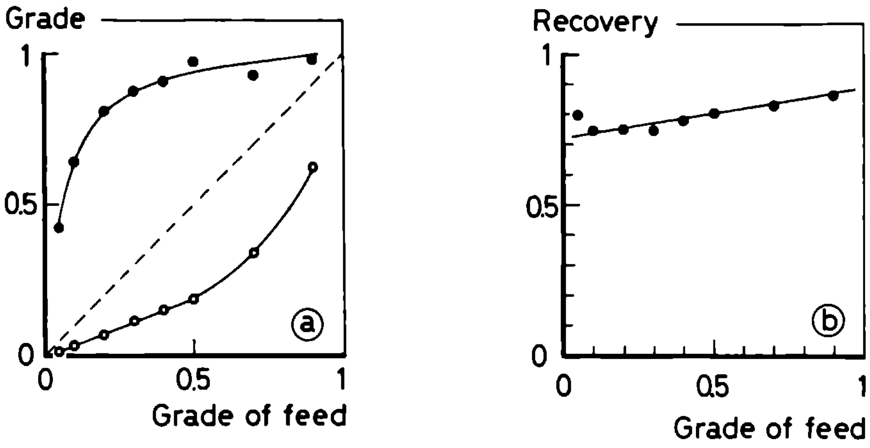

Figure 3.2.3 *Dependence of the grade of the separation products and the recovery of* $MnCO_3$ *in the mags on its concentration in the feed.*
●: *Mags;* o: *Overflow.*

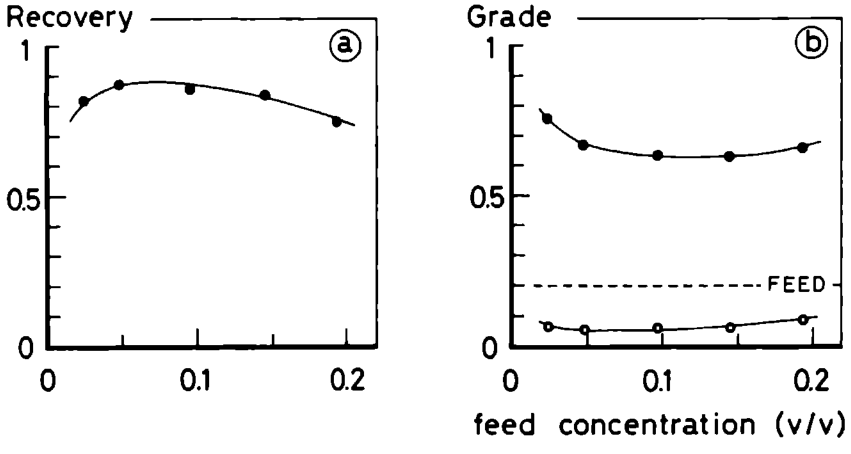

Figure 3.2.4 *Dependence of the recovery of* $MnCO_3$ *in the mags and the grade of the separation products on the concentration of particulate material in the feed.*
●: *Mags;* o: *Overflow.*

5 % (v/v).

In order to investigate the separator performance for slurries of larger particles, several tests were carried out using wolframite ore and fly ash from electrical power plants. The magnetic properties of the different size fractions are given in Table 3.2.1. Here, the saturation magnetization M_{sat} is a measure of the overall concentration of the ferromagnetic component in the particular size fractions. χ_{para} is the mean susceptibility of the paramagnetic components. Clearly, for fly ash, the bulk of the ferromagnetic material is present in the smallest size fraction, while for wolframite ore it is more evenly distributed over the different fractions. The largest particles tend to be more ferromagnetic than the smaller ones. In addition, the paramagnetic components of wolframite ore are stronger than those of fly ash.

In Figure 3.2.5a the recovery of ferromagnetic material in the mags is plotted against the applied magnetic field for a slurry of 1.3 % (v/v) wolframite ore, processed at a fluid velocity of 52 mms^{-1}. The recovery rises sharply for fields up to 1 T. At higher fields the recovery still increases, while the concentration of ferromagnetic material in the mags, relative to the feed, as depicted in Figure 3.2.5b, reaches a maximum around 1 T. At

Table 3.2.1 Magnetic properties of wolframite ore and fly ash from the Nijmegen electrical power plant.

	Wolframite ore			Fly ash		
Particle Size Range (μm)	Weight (%)	M_{sat} (emu/g)	χ_{para} (10^{-6} emu/gG)	Weight (%)	M_{sat} (emu/g)	χ_{para} (10^{-6} emu/gG)
+106	11.2	0.468	36.6	5.2	0.438	18.8
90-106	6.3	0.367	25.5	2.3	0.570	6.4
75- 90	9.1	0.337	18.6	2.1	0.705	6.4
63- 75	11.2	0.225	11.8	2.3	0.890	6.6
53- 63	13.2	0.177	9.5	7.2	1.123	7.3
45- 53	11.4	0.219	10.9			
38- 45	13.9	0.296	12.7	3.6	1.007	6.1
-38	23.7	0.227	13.6	77.3	2.529	30.8

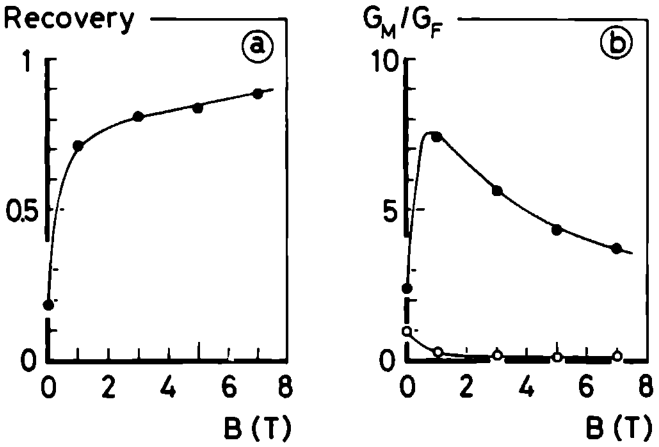

Figure 3.2.5 Recovery of ferromagnetic material and its relative concentration in the separation products for a slurry of wolframite ore as a function of the applied magnetic field.
●. Mags; o: Overflow.

higher fields, paramagnetic material is collected in the mags, resulting in a lower ferromagnetic grade.

In the case of fly ash a different method of processing was used: the cascade method. This means that after each run one of the separation products is used as feed material in the next run. Then, in the new run, process conditions like fluid velocity or magnetic field can be changed. This cascade method was employed in order to prevent total blockage of the outlet by a ferromagnetic build-up. In the results of Figure 3.2.6 the overflow product of each run was used as feed material in the next run at a higher field. The slurry, originally containing 2.5 % (v/v) fly ash, was processed at a fluid velocity of 27 $\mathrm{mms^{-1}}$. In Figure 3.2.6a the recovery of ferromagnetic material reaches a maximum at around 1 T, above which it gradually decreases. The major ferromagnetic component is collected in the mags at low fields, while at higher fields the concentration of the collected ferromagnetic component rapidly decreases; see Figure 3.2.6b. Above approximately 2 T a small ferromagnetic component is still collected, however, here the largest components present are paramagnetic.

For a processing method in which, for fields above 1 T, the feed material

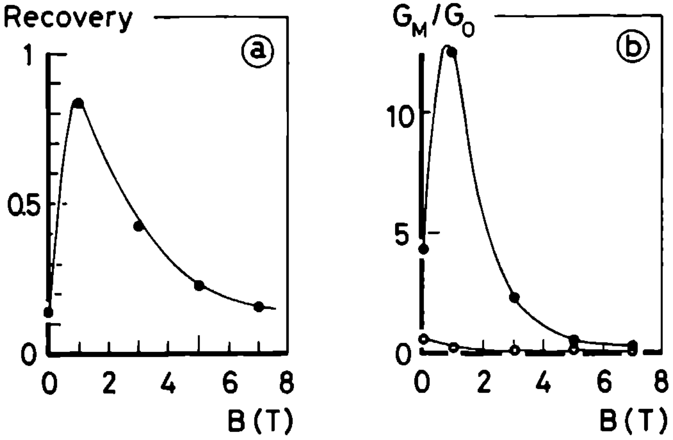

Figure 3.2.6 Field dependence of the recovery and concentration of ferromagnetic material in the separation products, relative to the original feed, in a cascade-type separation experiment on a slurry of fly ash in water.
● Mags; o· Overflow.

consisted of the overflow product of a separation run at 1 T, a maximum in the recovery was observed at an applied central field of 6 T. The concentration of the ferromagnetic component is then reduced by a factor 20.

4. Discussion and Conclusions

The role of the magnetic field in the above described continuous flow separator is twofold. First, gradients in the field cause the particles to settle at an enhanced rate, proportional to $B\nabla B$, and second, the field itself induces magnetic flocculation of particles, because of which the influence of the gradients becomes even stronger.

In this chapter we have demonstrated that the continuous flow separator is capable of processing slurries of both very fine particles and of relatively coarse multi-component mixtures. In addition, operation of the system is found to be very simple and truly continuous, although some difficulties can be expected in recollecting strongly ferromagnetic material because of possible build-up on the walls of the separator near the centre of the magnet.

However, we have demonstrated that, to a large extend, this can be avoided by employing a cascade-type separation process, 'scalping', in which the majority of the ferromagnetic component is removed at low fields.

Since the separation device, shown in Figure 3.1.1, is only situated in the upper half of the magnet bore, one half of the generated field is not used for separation purposes. In order to examine the possibility of also taking advantage of this part of the field, the separator was placed upside down in the lower part of the Bitter magnet. Of course, this new situation only distinguishes itself from the old one by the fact that, effectively, the direction of the gravitational force is now opposite. In other words, the density ρ in equation (3.1.2) has changed sign.

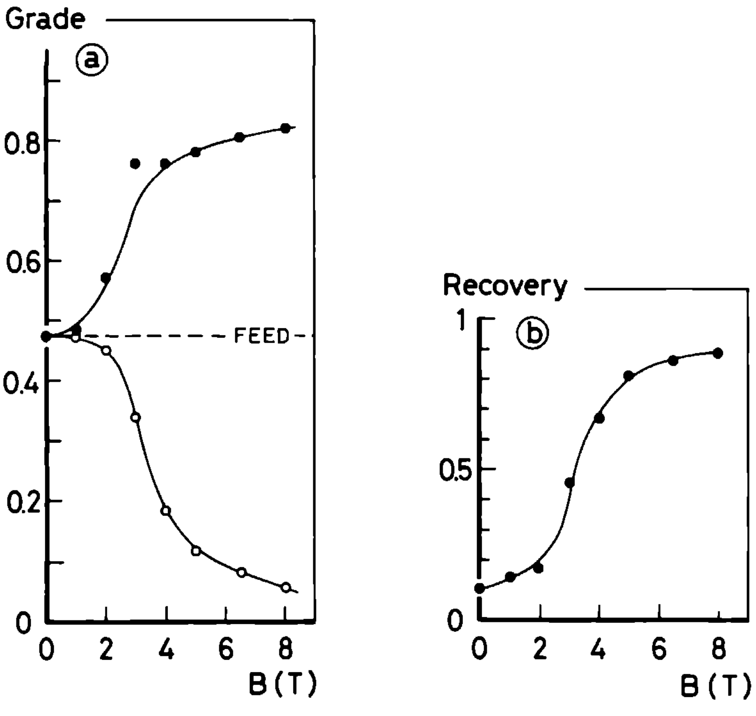

Figure 4.1 *Grade of the separation products and the recovery of* $MnCO_3$ *in the mags as a function of applied magnetic field for a slurry of* $MnCO_3$ *and* SiO_2*. The separator was placed upside down in the lower half of the magnet. (c.f. Figure 3.2.1)*

The results of a separation run with the separator in the upside down position are shown in Figure 4.1 for a slurry of $MnCO_3$ and SiO_2. All other experimental conditions were the same as in the experiment reported earlier (see Figure 3.2.1). Clearly, the separation performances are quite similar, which, in fact, can be expected in cases when the gravitational forces are small compared to the magnetic ones. One therefore may conclude that, in principle, a solenoid-type magnet can contain two separation devices, above and below its midpoint (mirror images), thereby doubling the maximal slurry throughput.

When the gravitational force on the magnetic particles becomes comparable to the magnetic force, the performances of the upper and lower separation devices will start to deviate. This is schematically illustrated in Figure 4.2. Here, a particle with radius b. net density ρ and magnetic density ρ_M

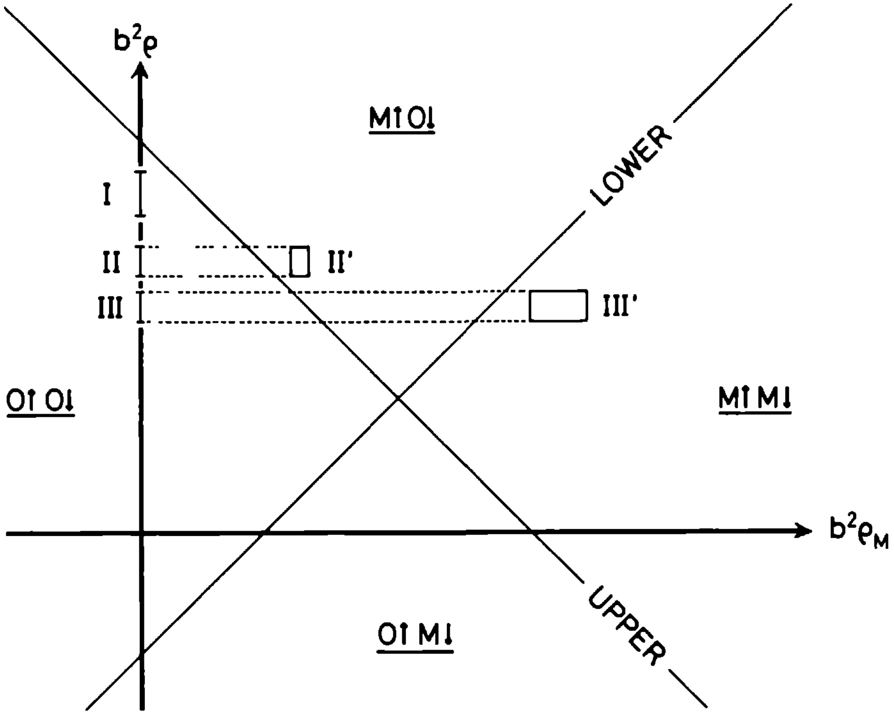

Figure 4.2 Schematic representation of the separation performance of a dual CFMS device. Explanation is given in the text.

(see equation (3.1.2)) is represented by a point $(b^2\rho_M, b^2\rho)$ in a rectangular coordinate system. Thus, in Figure 4.2, the gravitational aspects of a dispersion of particles are schematically represented along the y $(= b^2\rho)$ -axis, while the magnetic aspects of the particle-field system are represented along the x $(= b^2\rho_M)$ -axis. For the continuous flow magnetic separator, a balance situation occurs when the magnetically enhanced velocity of the particles with respect to the fluid, according to equation (3.1.2), equals the fluid velocity in the separation zone. For the upper and lower separation devices the balance conditions can be expressed as

$$b^2(\rho + \rho_M) = v_o/\alpha \tag{4.1}$$

and

$$b^2(-\rho + \rho_M) = v_o'/\alpha \tag{4.2}$$

respectively. Here, v_o and v_o' are the fluid velocities in respectively the upper and the lower device. The balance situations are represented by the tilted lines in Figure 4.2. Any point in the plane of Figure 4.2 which lies above the balance line of the upper separator corresponds to a particle with a settling velocity larger than the fluid velocity in the separation zone and therefore this particle will be collected in the mags. Thus, the half-plane *above* the balance line of the upper separator corresponds to the magnetic product M↑ and the half-plane *below* the balance line to the overflow product O↑. For the lower separator the half-plane *below* its particular balance line corresponds to the magnetic product M↓ and the *upper* half-plane to the overflow product O↓. Negative values of $b^2\rho$ and $b^2\rho_M$ occur when the values for, respectively, density and magnetic susceptibility of the fluid exceed those of the particles themselves.

The performance of the separator is now easily explained using Figure 4.2 for a two-component slurry. The non-magnetic component, $\chi=0$ (approximately) $\rightarrow \rho_M=0$, is represented by a certain interval I on the $b^2\rho$-axis. The width along this vertical axis is, of course, related to the particle size distribution. For all non-magnetic particles to be collected in the overflow product O↑ of the upper separator, the fluid velocity in this device has to be adjusted in such a way that the balance line intersects the $b^2\rho$-axis above the complete interval. At zero field, the magnetic component can also be represented by an interval (II) on the vertical axis. However, when a magnetic field is applied, the magnetic density will increase (horizontal axis). At a a certain applied field the magnetic component can be represented by a rectangle II', of which the width in horizontal direction is proportional to, among others, the particle size distribution, the magnetic susceptibility and the magnetic force density. By increasing the field, this rectangle can be situated completely above the balance line, as shown in Figure 4.2. Then, a complete separation between the magnetic and the non-magnetic particles is achieved.

When the magnetic fraction consists of two discrete components, represented, at zero field, by the intervals II and III, the magnetic field can be adjusted such that they are both collected in the mags M↑. In the presence of a field, these two components are represented by the rectangles II' and III'. Obviously, III' corresponds to the component with the higher susceptibility. It is possible to adjust the fluid velocity in the lower separator in such a way that the corresponding balance line separates II' and III', as shown in Figure 4.2. This implies that, when the mags M↑ of the upper separator are subsequently processed by the lower one, a complete separation between the magnetic components is achieved, since II' is collected in the overflow product O↓ and III' in the mags M↓. Other combinations are also possible. Of course, the fluid velocities in both devices can be adjusted separately, e.g. via variation of the diameter of the separation tubes. One can therefore conclude that a (dual) separation system as described here, placed in the bore of a solenoid-type magnet is capable of producing three well-defined fractions of a slurry in a continuous separation mode.

For a cylindrically-symmetric magnet, the magnetic field $H(r,z)$ is analytical and so is $H\nabla H$. In cases when the influence of gravity is negligible, an equilibrium situation occurs when the magnetic force is balanced by the hydrodynamic drag force. The fluid velocity in the separation zone can then be expressed as

$$v_o = v_M G(r_a, z_a), \tag{4.3}$$

where v_M is the magnetic velocity of the magnetic particles, defined as

$$v_M = \frac{2\chi\mu_o I^2 b^2}{9\eta a^3} . \tag{4.4}$$

Here, I is the total current in the coil and a is a mean coil radius. In equation (4.4), $G(r_a,z_a)$ is a purely geometrical function of the normalized cylindrical coordinates r_a and z_a, describing the spatial dependence of the magnetic force density. For the dual continuous flow magnetic separator, the maximum processing rate P will then be

$$P = 2Av_o = 2Av_MG(x,z_{ao}), \tag{4.5}$$

where A is the net cross-sectional area of the separation tube and where the optimum value $G(x,z_{ao})$, optimized over the cross-section of the magnet bore at the optimum axial position z_{ao}, can be obtained quite simply numerically.

In the above experiments, a fluid velocity of 10 mms^{-1} corresponds to a processing rate of about 72 m^3 per hour per m^2 of magnet bore cross-section.

For solenoid-type magnets, a barrier in the magnetic force density is present near the end of the coil, which, in the case of continuous flow magnetic separation, should prevent magnetic particles from being carried away by the fluid stream in the separation zone. The outlet of the feed pipe should therefore be situated between this barrier and the centre of the magnet.

Although in various figures in this chapter the separation performance is presented as a function of field, one should always bear in mind that it is not the field strength itself, but the product of field and gradient of the field which determines the performance of this system. To maintain constant separation efficiency, the applied magnetic field can be decreased by a certain factor if, at the same time, the gradient is increased by the same factor. Of course, if one wants to take advantage of magnetically induced flocculation, a lower limit is set to the field strength by the threshold field for flocculation.

As an example, the field profile and the corresponding field gradient and magnetic force density were calculated and plotted in Figure 4.3, for a solenoid with the same dimensions as the Bitter magnets used in the experiments. In contrast to a Bitter magnet, in which the current distribution is radially dependent, here a uniform current distribution was assumed. For a solenoid-type magnet, both the field and the field gradient and thus the magnetic force density are analytical (see Appendix III). For Figure 4.3, expression (AIII.4) of Appendix III was used, which only describes the field along the axis of the magnet. Obviously, the force density reaches a maximum near the end of the

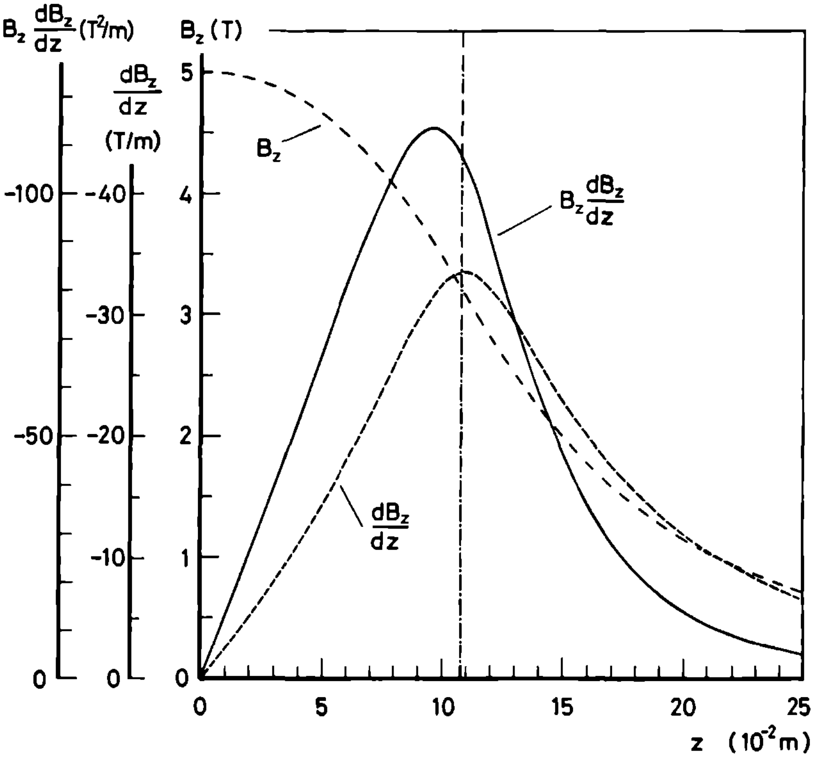

Figure 4.3 Calculated field profile, field gradient and a measure of the magnetic force density along the long axis of a solenoid with the same dimensions as a 15 tesla Bitter magnet. (α = 6.36; β = 3.09; see Appendix III)

coil, at a position where the field has dropped to about 70 % of its value at the centre of the magnet. This maximum in force density does not coincide with, but is near to the position where the field gradient reaches its maximum. In the Bitter magnets used in the experiments, we measured a barrier height of about $2 \cdot 10^8$ Nm^{-3} at a central field of 7 T.

Since these Bitter magnets were not designed to generate non-uniform fields, usually on the contrary, the separation performance of the CFMS-system, as reported in this chapter, can certainly be improved by employing a magnet system that is especially designed and constructed for this application. The designer also has to take account of certain practical aspects concerning the recollection of the mags from the centre of the magnet. A split-coil magnet will probably be satisfactory. The continuous mode of operation of the type of separator, described in this chapter, anyhow, strongly encourages the use of superconducting magnets.

Even with a properly designed separator, the magnetic forces involved will be several orders of magnitude smaller than those encountered in HGMS. Therefore, the separation performance of CFMS cannot be expected to be just as selective. However, CFMS is well suited to separate slurries in cases where selectivity is not a first requirement or in which the magnetic component is present in high concentrations. In addition, CFMS is a promising technique to treat mineral slurries prior to further processing, e.g. by means of other types of magnetic separation.

References

1. S.E. Khalafalla, IEEE Trans. on Magn., MAG-12, (1976), p 445.
2. R.E. Rosensweig, J. of AIAA, 4, (1966), p 1751.
3. U.T. Andres, Mineral Sci. and Engn., 7, (1975), p 99.
4. U.T. Andres, I. Lin and I. Yaniv, Proc. 5th Int. Conf. Magnet Techn., Rome (1975), p 389.
5. I.J. Lin and N.P. Finkelstein, J. South African Inst. Mining and Metallurgy, (1974), p 111.
6. Y. Zimmels, I. Yaniv, I.J. Lin and U. Levite, IEEE Trans. on Magn., MAG-14, (1978), p 269.
7. Y. Zimmels and I.J. Lin, IEEE Trans. on Magn., MAG-19, (1983), p 27.
8. Y. Zimmels and I.J. Lin, IEEE Trans. on Magn., MAG-18, (1982), p 921.
9. N. Pezlescu, V. Bădescu and E. Brânduşa Bradu, IEEE Trans. on Magn., MAG-17, (1981), p 3320.
10. D. Fletcher, Magn. Separation News, 1, (1983), p 37.
11. U.T.Andres, G.M. Bunin and B.B. Gil, Zh. Prikl. Mekhan. i Tekhn. Fiz., 3, (1966), p 158.
12. H.H. Kolm, J.A. Oberteuffer and D.R. Kelland, Scientific American, 233, (1975), p 46.
13. P.W. Riley and D. Hocking, IEEE Trans. on Magn., MAG-17, (1981), p 3299.
14. R.R. Birss and M.R. Parker in *"Progress in Filtration and Separation"*, Vol. 2, R.J. Wakeman, Ed., Elsevier Amsterdam (1981).
15. S.G. Frantz, *"Magnetic Separation Method and Means"*, U.S. Patent No. 2,056,426 (Oct. 6, 1936).
16. J.A. Good and E. Cohen, IEEE Trans. on Magn., MAG-12, (1976), p 493.
17. E. Cohen and J.A. Good, IEEE Trans. on Magn., MAG-12, (1976), p 503.
18. E. Cohen and J.A. Good, IEEE Trans. on Magn., MAG-12, (1976), p 552.
19. K.Schonert, A. Supp and H. Dorr, Proc. 12th Int. Min. Proc. Congress, Meeting 4, Paper 1, Sao Paulo, Brazil (1977).
20. E.C. Hise, IEEE Trans. on Magn., MAG-18, (1982), p 847.
21. E.C. Hise, A.S. Holman and F.J. Friedlaender, IEEE Trans. on Magn., MAG-17, (1981), p 3314.
22. H.K. Collan, M.A. Kokkala, O.E. Toikka and T. Meinander, Report TKK-F-A456, (1981), Helsinki Univ. of Techn.
23. J. Kopp and J.A. Good, IEEE Trans. on Magn., MAG-18, (1982), p 833.
24. P.A. Cheremnykh, V.K. Fyodorov and A.N. Piskunov, J. de Phys., 45, (1984),

p. C1-793.

25. Y.M. Eyssa and R.W. Boom, IEEE Trans on Magn., MAG-11, (1975), p 1585.
26. J. Gerhold and J. Schmidt, J. de Phys., 45, (1984), p C1-785.
27. M.R. Parker, J. de Phys., 45, (1984), p C1-753.
28. M.R. Parker, Proc. Int. Symp. Electr. Magn. Separation and Filtration Techn., Antwerp, (1984), p 1.
29. J. Lindley, IEEE Trans. on Magn., MAG-18, (1982), p 836.
30. M.R. Parker, R.P.A.R. van Kleef, H.W. Myron and P. Wyder, J. Magn. Magn. Mater., 27, (1982), p 250.
31. R.P.A.R. van Kleef, M.R. Parker, H.W. Myron and P. Wyder, IEEE Trans. on Magn., MAG-18, (1982), p 1650.
32. R.P.A.R. van Kleef, H.W. Myron, P. Wyder and M.R. Parker, J. Appl. Phys., 54, (1983), p 4223.
33. R.P.A.R. van Kleef, H.W. Myron, M.R. Parker and P. Wyder, Proc. World Filtration Congr. III, Downingtown, USA, Volume II, (1982), p 769.
34. J. Sikkenga, H.R. Segal, C.P. van Driel and C.B.W. Kerkdijk, *"Fly ash and AFBC ash upgrading by HGMS"*, December 1983, (available through FDO, Amsterdam).
35. V. Hencl and J. Svoboda, 13th Int. Min. Proc. Congr., Warsaw, (1979), p 209.
36. J. Svoboda, private communication.
37. R.P.A.R. van Kleef, H.W. Myron, P. Wyder and M.R. Parker, J. de Phys., 45, (1984), p C1-763.
38. R.P.A.R. van Kleef, H.W. Myron, P. Wyder and M.R. Parker, to be published in IEEE Trans. on Magn., September 1984.
39. R.P.A.R. van Kleef, Proc. Minisymposium Toegepaste Supergeleiding in Nederland, Petten, (1983), p 49.

APPENDIX III.

The Magnetic Field of a Solenoid

Various methods have been developed (1) for calculating the field of a solenoid at other points than its centre. However, the regions of the field to which the different methods apply are limited. In this appendix, expressions for the magnetic field will be given for the following cases:

a) Field along the axis of a coil,
b) Off-axis field in the central zone,
c) Fields outside the central zone.

Except for case c), the expressions will describe the field profile relative to the central field, which can be calculated separately.

a) Field along the axis of a coil.

Consider an axially uniform solenoid of length 2b, bore diameter $2a_1$ and outer diameter $2a_2$, as schematically shown in Figure AIII.1. This solenoid can be seen to be partitioned into two subcoils. The field $H_z(z,0)$ along the axis can then simply be calculated from a superposition of the end fields of two subcoils, extending distances of respectively (b + z) to the left and (b - z) to the right of the field point z. The end field of any uniform,

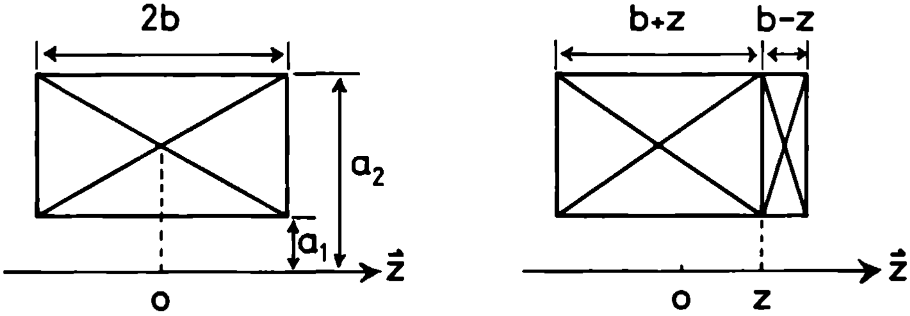

Figure AIII.1 Schematic representation of the superposition method for calculating the axial field of a solenoid.

cylindrically symmetric coil is given, by symmetry, by half the central field of a coil of twice the length.

For a coil of dimensions a_1, a_2 and $2b$, as shown in Figure AIII.1, the central field H_o is given by

$$H_o = j\lambda a_1 F(\alpha,\beta), \tag{AIII.1}$$

where $\alpha = a_2/a_1$, $\beta = b/a_1$, j is the current density and λ the space factor, defined as the ratio of active to total cross-section of the winding. $F(\alpha,\beta)$ is a geometric field factor, given by

$$F(\alpha,\beta) = \frac{4\pi\beta}{10}\{\sinh^{-1}(\alpha/\beta) - \sinh^{-1}(1/\beta)\}. \tag{AIII.2}$$

The field at a point z/a_1 on the axis can then, via the superposition method, be written as

$$H_z(z/a_1) = \frac{j\lambda a_1}{2}\{F(\alpha,\beta + z/a_1) + F(\alpha,\beta - z/a_1)\}, \tag{AIII.3}$$

and thus,

$$H_z(z/a_1) = H_z(0)\left\{\frac{F(\alpha,\beta + z/a_1) + F(\alpha,\beta - z/a_1)}{2F(\alpha,\beta)}\right\}. \tag{AIII.4}$$

When the axial field point lies outside the coil, one must use the relation

$$F(\alpha,\beta - z/a_1) = -F(\alpha,z/a_1 - \beta). \tag{AIII.5}$$

b) Off-axis field in the central zone.

The central zone of a magnet is defined as the sphere which does not enclose any of the magnet corners. Inside this sphere the axial and radial components of the field of a cylindrically symmetric magnet are given by

$$H_z(\rho,\theta) = H_o \{1 + E_2(\frac{\rho}{a_1})^2 P_2(u) + E_4(\frac{\rho}{a_1})^4 P_4(u) + \dots\} \qquad \text{(AIII.6a)}$$

and

$$H_r(\rho,\theta) = H_o \{E_2(\frac{\rho}{a_1})^2 P_2'(u) + E_4(\frac{\rho}{a_1})^4 P_4'(u) + \dots\}. \qquad \text{(AIII.6b)}$$

Here, the origin is assumed to be on the midplane of symmetry of the coil. ρ and θ are the conventional spherical coordinates of radius and polar angle and $P_n(u)$ are Legendre Polynomials ($u = \cos\theta$). The coefficients E_n are given by

$$E_{2n} = \frac{1}{H_o} \frac{1}{(2n)!} \left. \frac{d^{2n} H_z(z.0)}{dz^{2n}} \right|_{z=0}. \qquad \text{(AIII.7)}$$

Equation (AIII.6) can be written in the form

$$H_z(\rho,\theta) = j\lambda a_1 \{F(\alpha,\beta) + F(\alpha,\beta)E_2(\frac{\rho}{a_1})^2 P_2(u) + \dots\} \qquad \text{(AIII.8a)}$$

and

$$H_r(\rho,\theta) = j\lambda a_1 \{F(\alpha,\beta)E_2(\frac{\rho}{a_1})^2 P_2'(u) + \dots\}. \qquad \text{(AIII.8b)}$$

In the form $F(\alpha,\beta)E_n(\alpha,\beta)$ the error coefficients are tabulated in Ref. (1), pp 235-236, for uniform-current-density coils and for coils with a $j = j_o a_1/r$ current distribution (Bitter coils).

c) Fields outside the central zone.

The field at any point in space can be calculated from a summation of contributions to the field of ideal current loops (zero cross-section). The magnet coil can be approximated by a set of elemental loops, which can even be given different currents $I = j\lambda\Delta r\Delta z$. In practice, Δr and Δz have to be small compared to the diameter of the loop.

The axial and radial field components of an elemental loop of radius a are given by

$$H_z(z,r) = \frac{2I}{10a} \{(1 + r/a)^2 + (z/a)^2\}^{-\frac{1}{2}}$$

$$\times \{K(\phi) + \frac{1 - (r/a)^2 - (z/a)^2}{(1 - r/a)^2 + (z/a)^2} F(\phi)\} \tag{AIII.9a}$$

and

$$H_r(z,r) = \frac{2I}{10a} (z/r) \{(1 + r/a)^2 + (z/a)^2\}^{-\frac{1}{2}}$$

$$\times \{-K(\phi) + \frac{1 + (r/a)^2 + (z/a)^2}{(1 - r/a)^2 + (z/a)^2} E(\phi)\}, \tag{AIII.9b}$$

where

$$\phi = \sin^{-1} k \tag{AIII.10}$$

and

$$k = \{\frac{4(r/a)}{(1 + r/a)^2 + (z/a)^2}\}^{-\frac{1}{2}}. \tag{AIII.11}$$

The complete elliptic integrals of first and second kind, $K(\phi)$ and $E(\phi)$, are given in Ref. (2), while their numerical values are tabulated in Ref. (3).

References

1. D.B. Montgomery, *"Solenoid Magnet Design"*, Wiley-Interscience, New York, (1969).
2. K. Rektorys, Ed., *"Survey of Applicable Mathematics"*, M.I.T. Press, Cambridge, Massachusetts, (1969).
3. V.M. Belyakov, P.I. Kravtsova, M.G. Rappoport, *"Tables of Elliptic Integrals"*, Part I, Pergamon Press, Oxford, (1965).

Summary

The influence of applied magnetic fields on the stability of dispersions of paramagnetic and diamagnetic particles was studied.

When a particle is immersed in a fluid (electrolyte), a surface charge develops on the surface of the particle, which, together with a diffuse charge distribution in the liquid, is called the electrical double layer. In addition to the attractive London- van der Waals interaction, the repulsive double layer interaction determines the stability of the suspension or colloid. An applied magnetic field induces an additional dipole-dipole interaction, which, due to its attractive nature, is capable of destabilizing the colloid, i.e. causing the particles to flocculate.

In chapter 2, the various aspects of interparticle interaction are considered. Here, the process of magnetic flocculation is being studied on the basis of potential energies of interaction in a two-particle system. From this, expressions for the velocity of one of the particles with respect to the other can be derived. By numerical integration of these expressions, the particle trajectories in a magnetic flocculation process can be obtained. These trajectories form the basis of a further analysis of the various aspects of magnetic flocculation, such as the influence of parameters like magnetic field, double layer potential and -thickness, dissimilar particle sizes, flocculation in a secondary energy minimum and the formation of clusters of more than two particles. In addition, these trajectories form the basis of a kinetic theory on flocculation, from which expressions for the flocculation frequency and half-life could be derived. These quantities show the same dependence upon particle number density as similar expressions, derived by Von Smoluchowski in his theory on rapid coagulation; the latter in the absence of a magnetic field.

For relatively coarse particles (> 1 μm), the process of magnetic flocculation was studied by means of measurements of the settling rate as a function of the applied magnetic field. For single particles, the settling velocity increases proportional to the square of the field, due to non-uniformity of the field. Then, at a certain value of the field (threshold field for flocculation), a discontinuity appears, which indicates the formation of two-particle clusters. At higher fields, again a B^2-dependence of the settling velocity is observed, however, with a different slope. This as a result of a different ratio of volume and hydrodynamic diameter of the cluster with respect

to the single particle. The threshold field for flocculation has been determined for a variety of paramagnetic compounds.

Magnetically induced flocculation is also possible in dispersions of diamagnetic particles. However, here the magnetic interaction is small so that immense values of the threshold field are to be expected. On the other hand, the diamagnetic properties of the particles can be effectively enhanced by suspending them in a paramagnetic liquid. From measurements of the flocculation threshold field of quartz particles at various concentrations of the dissolved paramagnetic salt, it was possible to determine the isoelectric point of quartz in this particular electrolyte. At low fields we could observe the influence of the combination of an anisotropic magnetic susceptibility and the non-spherical shape of the quartz particles on the settling velocity. The experimental results fitted the theoretical description of the influence of magnetic anisotropy on the light transmission of colloidal dispersions of graphite.

The stability of ultra-fine colloids (particle sizes << 1 µm) in applied magnetic fields cannot be studied by means of detection of the settling velocity. In this case, we have chosen for light transmission techniques. A description is given in the second part of chapter 3. The experimental results appear to be, to a certain extent, consistent with the kinetic theory in chapter 2, although processes like particle diffusion, which are not taken into account in the theory, obviously are of great importance.

In High Gradient Magnetic Separation (HGMS), particles are separated by means of a ferromagnetic filter matrix, which is magnetized in an external magnetic field. Due to polarization of the filter, large field gradients appear, that are responsible for the capture of magnetic particles on the filter. A short review of the present techniques of magnetic separation is given in chapter 1.

Experimental results, concerning high gradient magnetic filtration of ultra-fine colloids are given in the first part of chapter 3. At these particle sizes, the filtration efficiency is, in addition to magnetic and hydrodynamic interactions, also influenced by Brownian motion and interactions between the particles themselves. The capture of these ultra-fine particles on a ferromagnetic fiber has to be considered in terms of a spatial increase in particle number density, opposed by diffusion and double layer forces. Filtration experiments were carried out on colloids of CuO, at different values of the applied magnetic field and fluid velocity, with different particle sizes and concentrations of dispersing agent and with different types of filter material.

In chapter 4, an application of magnetically enhanced settling and magnetic flocculation for separation purposes is introduced. The separation between magnetic and non-magnetic particles can be achieved by allowing them to settle in a fluid stream, directed upwards. A non-uniform magnetic field causes the magnetic particles to settle at an increased rate, through which they are able to settle against the fluid stream, while non-magnetic particles are carried away by the liquid. The performance of the separator is determined under various experimental conditions. Because of its continuous operation, this separation system greatly encourages the application of superconducting magnets, this in contrast to several other magnetic separators.

Samenvatting

Onderzoek werd verricht naar de invloed van magnetische velden op de stabiliteit van suspensies van paramagnetische en diamagnetische deeltjes.

In een waterige oplossing (elektroliet) vormt zich op elk deeltje een oppervlakte lading en in de omringende vloeistof een diffuse ladingsverdeling van tegengesteld teken. Het geheel vormt de zogenaamde elektrische dubbellaag. Tesamen met de attraktieve London-van der Waals interaktie bepaalt de repulsieve dubbellaag interaktie de stabiliteit van de suspensie. Een aangelegd magneetveld induceert een additionele dipool-dipool interaktie. Het attraktieve karakter van deze interaktie maakt het mogelijk een suspensie van deeltjes te destabiliseren (flocculeren).

In hoofdstuk 2 wordt uitgebreid ingegaan op de diverse aspekten van de onderlinge interaktie tussen de deeltjes. Het proces van magnetische flocculatie is theoretisch bestudeerd door uit te gaan van de interaktie-energieën in een twee-deeltjes systeem. Hieruit kunnen uitdrukkingen worden afgeleid voor de snelheid van één van de deeltjes ten opzichte van het andere. Numerieke integratie levert dan de banen die de deeltjes beschrijven in een magnetisch flocculatie proces. Dit vormt de basis voor een analyse van diverse aspekten met betrekking tot magnetische flocculatie, zoals onder andere flocculatie in een secundair energie-minimum, de invloed van parameters als magnetische veldsterkte, elektrische dubbellaag potentiaal en -dikte, ongelijke deeltjesgrootte en de vorming van clusters met meer dan twee deeltjes. Tevens vormt dit de basis voor een kinetisch model, waarmee grootheden als flocculatie frekwentie en flocculatie halfwaarde-tijd bepaald konden worden. Deze grootheden blijken op dezelfde manier van de deeltjes-concentratie af te hangen als in Von Smoluchowski's theorie met betrekking tot "rapid coagulation"; dit laatste in afwezigheid van een magneetveld.

Het verschijnsel magnetische flocculatie werd, voor relatief grote deeltjes (> 1 µm) bestudeerd aan de hand van metingen van de bezinksnelheid in hoge magneetvelden. De bezinksnelheid van niet-geflocculeerde deeltjes vertoont een kwadratische veld-afhankelijkheid als gevolg van de aanwezige inhomogeniteit van het veld. Bij een zeker magneetveld, het drempelveld voor flocculatie, worden twee-deeltjes clusters gevormd. Voor hogere velden wordt weer een kwadratische veld-afhankelijkheid gemeten, echter met een andere evenredigheidskonstante. Dit als gevolg van een gewijzigde verhouding tussen volume en hydrodynamische diameter van de cluster. Voor diverse paramagnetische stoffen

werd op deze wijze het drempelveld voor flocculatie bepaald.

Hetzelfde is mogelijk voor suspensies van diamagnetische stoffen. Echter, de magnetische interaktie is hierbij dermate klein dat gigantische magneetvelden benodigd zouden zijn. De deeltjes zijn daarentegen effektief sterker diamagnetisch te maken door ze in suspensie te brengen in een paramagnetische vloeistof. Uit metingen van het drempelveld voor flocculatie bij verschillende concentraties van het opgeloste paramagnetische zout bleek het mogelijk om het iso-elektrisch punt van diamagnetische deeltjes in een elektroliet te bepalen. Bij lage velden werden in de bezinksnelheid van kwarts-deeltjes effekten waargenomen, veroorzaakt door een kombinatie van een anisotrope magnetische susceptibiliteit en het niet-sferisch zijn van de deeltjes. De experimentele resultaten konden worden beschreven analoog aan een beschrijving van de invloed van magnetische anisotropie op lichttransmissie in colloïdale oplossingen van grafiet.

Voor de bestudering van de stabiliteit van suspensies met zeer kleine deeltjes (<< 1 μm) is meting van de bezinksnelheid ongeschikt. In dit geval werd de invloed van magnetische velden waargenomen door middel van lichttransmissie. Een beschrijving hiervan is te vinden in het tweede deel van hoofdstuk 3. De meetresultaten blijken tot op zekere hoogte te voldoen aan het kinetisch model in hoofdstuk 2. Daarbij bestaat de indruk dat het proces van deeltjes diffusie, wat niet verwerkt is in dit kinetisch model, een grote rol speelt.

Hoge Gradiënt Magnetische Scheiding (HGMS) is een deeltjes-scheidingstechniek waarbij gebruik wordt gemaakt van een ferromagnetisch filter. Dit filter wordt gemagnetiseerd in een extern magneetveld, waardoor sterke veldgradiënten ontstaan die verantwoordelijk zijn voor de invang van magnetische deeltjes. Een kort overzicht van bestaande technieken op het gebied van magnetische scheiding is gegeven in hoofdstuk 1. Naast onderzoek aan konkrete commerciële toepassingen van HGMS is ruim aandacht besteed aan magnetische filtratie van ultra-fijne kolloïden. Experimentele resultaten op dit gebied worden beschreven in het eerste deel van hoofdstuk 3. Voor deeltjes met dergelijk kleine afmetingen wordt de filtratie-efficiëntie, behalve door de magnetische en hydrodynamische wisselwerkingen, ook beïnvloed door Brownse beweging en de interakties tussen de deeltjes onderling. In deze deeltjesgrootte limiet moet de invangst van deeltjes op een ferromagnetisch filter gezien worden als een plaatselijke verhoging van de deeltjes concentratie, tegengewerkt door diffusie en dubbellaag krachten. Metingen werden verricht aan suspensies van ultrafijne CuO-deeltjes, bij verschillende waarden voor magneetveld, vloeistofsnelheid, deeltjesgrootte en kolloïdale stabiliteit en voor verschillende typen filters.

In hoofdstuk 4 wordt een techniek geïntroduceerd waarbij magnetisch geïnduceerde bezinking en flocculatie worden toegepast in een separatie-proces dat tot doel heeft "magnetische" deeltjes af te scheiden van "niet-magnetische" deeltjes. Hiertoe is een magnetische separator gebouwd waarin deze scheiding teweeg wordt gebracht door deeltjes in een opwaarts gerichte vloeistofstroom te laten bezinken. Een inhomogeen magneetveld vergroot de bezinksnelheid van de magnetische deeltjes met maximaal één orde van grootte, waardoor deze in staat zijn om tegen de stroom in te bezinken, terwijl niet-magnetische deeltjes met de stroom worden meegevoerd. De werking van de separator is bepaald voor diverse experimentele parameters en omstandigheden. Het grote voordeel van het systeem is dat het zeer geschikt is voor toepassing van supergeleidende magneten, dit in tegenstelling tot vele andere magnetische separatoren.

CURRICULUM VITAE

R.P.A.R. van Kleef

Geboren : 22 januari 1956 te Nijmegen

1968 - 1974 : Atheneum B, Scholengemeenschap Canisiuscollege -
Mater Dei, Nijmegen

1974 : Begin studie Natuurkunde, K.U. Nijmegen

14 september 1978 Kandidaatsexamen Natuurkunde (N1),
Kandidaatsexamen Sterrenkunde (A1),
K.U. Nijmegen

15 december 1980 : Doctoraalexamen Experimentele Natuurkunde,
K.U. Nijmegen
Hoofdvak Vaste Stoffysica

1981 - 1984 : In dienst van de Stichting voor Fundamenteel
Onderzoek der Materie (F.O.M.)
Promotieonderzoek op de afdeling
Experimentele Natuurkunde 4,
Faculteit der Wiskunde en Natuurwetenschappen,
Katholieke Universiteit Nijmegen,
onder leiding van Prof. Dr. P. Wyder

STELLINGEN

I

Door hun overeenkomsten met molekulaire vloeistoffen en hun geschiktheid voor lichtverstrooiingsexperimenten zijn kolloïdale systemen ideale kandidaten voor het testen van diverse theorieën met betrekking tot de gecondenseerde materie, zowel onder evenwichts- als onder niet-evenwichtskondities.

D. Ronis, Phys. Rev. Lett., 52, 473, (1984).

II

In de door Svoboda en Žofka toegepaste uitbreiding van de definitie voor de stabiliteitsverhouding W van een suspensie van deeltjes in een aangelegd magnetisch veld is ten onrechte geen rekening gehouden met de hoekafhankelijkheid van de magnetische dipool-dipool interaktie energie.

J. Svoboda, J. Žofka, J. Colloid Interface Sci., 94, 37, (1983).

III

De opmerkelijke afname in de spoed van de helixstruktuur in vloeibare kristallen, zoals deze optreedt bij het d.m.v. temperatuurverhoging naderen van de smectisch A fase vanuit de chiraal smectisch C fase, kan, in tegenstelling tot de bewering van Yamashita en Kimura, niet het gevolg zijn van fluktuaties in de tilthoek van de molekulen.

M. Yamashita, H. Kimura, J. Phys. Soc. Jpn., 52, 333, (1983);
J. Phys. Soc. Jpn., 51, 2419, (1982).
J. Muševič, B. Žekš, R. Blinc, L. Jansen, A. Seppen, P. Wyder,
to be published.

IV

The crossing or near avoided crossing of two or more RE (molecular rotational energy) surfaces would lead to resonance effects analogous to Jahn-Teller-Renner effects associated with the crossing of two PE (vibrational potential energy) surfaces. Such crossings of RE surfaces would provide a detailed semiclassical framework for visualizing complex rovibrational or rovibronic interactions.

W.G. Harter, C.W. Patterson, J. Chem. Phys., 80, 4241, (1984).

V

Door bij experimenten met elektronfocussering in metalen de energie van de geïnjekteerde elektronen te variëren, wordt informatie verkregen over de elektron-fonon interaktie bij lage energie. Als zodanig is deze methode een aanvulling op de puntkontaktspektroskopie, die vooral gevoelig is voor hogere energieën.

VI

Hoewel de effekten op de normaaltrillingen van een kristal ten gevolge van incommensurabele modulatie tamelijk drastisch zijn, blijven de experimentele studies hiervan te vaak beperkt tot pogingen om fasonen en amplitudonen te observeren.

VII

Bij de berekening van de kritische diffusie driftsnelheid van submicron deeltjes in de nabijheid van een ferromagnetische fiber hebben Takayasu, Gerber en Friedlaender ten onrechte de elektrische dubbellaag interaktie tussen de deeltjes onderling buiten beschouwing gelaten.

M. Takayasu, R. Gerber, F.J. Friedlaender, IEEE Trans. on Magn., MAG-19, 2112, (1983).

VIII

Het grote verschil in de halfwaardebreedte van de gemeten en de berekende signalen bij magnetische focussering van elektronen met behulp van dubbel puntkontakten kan verklaard worden door kleine afwijkingen van de ideale elektronen-banen in het kristal ten gevolge van dislocaties.

IX

De singuliere toestandsdichtheid van het twee-dimensionale elektrongas in hoge magneetvelden zou gebruikt kunnen worden om een afstembare ver-infrarood laser te maken.

X

Bij onderzoek naar de relatie tussen het kolloïdchemisch gedrag en de vaste stoffysische eigenschappen van halfgeleiders in halfgeleider-elektroliet systemen kan instraling van bandgap licht zeer bruikbaar zijn.

E.H.P. Logtenberg, proefschrift, Eindhoven 1983.

XI

Als gevolg van de kombinatie van de huidige mogelijkheden tot opslag van steenkool in Nederland en het daar heersende klimaat, moet reiniging van deze brandstof door middel van HGMS in droge vorm zonder meer onmogelijk geacht worden.

XII

De aanduiding 'eenvoudig', waarmee sommige auteurs door henzelf ontwikkelde theorieën en modellen classificeren, kan duiden op een zekere bescheidenheid maar biedt bovenal de mogelijkheid om de gevolgen van een experimentele tegenspraak te omzeilen.

R.P.A.R. van Kleef Nijmegen, 14 september 1984.